Manufacturing and characterisation of Ti-suboxides for sensing and energy applications

Adamaki, Vaia

Award date:
2015

Awarding institution:
University of Bath

Manufacturing and characterisation of Ti-suboxides for sensing and energy applications

Vaia Adamaki

A thesis submitted for the degree of Doctor of Philosophy

University of Bath
Department of Mechanical Engineering

December 2014

...για τον μπαμπά μου

Acknowledgements

I would really like to thank Prof. Chris Bowen and Prof. John Taylor for guiding me through the course of my PhD. I was very lucky to have such supporting, helpful and friendly supervision!

I need to give special thanks to my first supervisor Dr. Andrew Dent who was the one that gave me the opportunity in 2011 to move from Greece and start my PhD…and miss the four following sunny Greek summers! Together with Dr Domenico Regonini, their guidance and trust in the beginning gave me confidence to start my PhD.

Additionally, I'd like to thank my officemates Rhodri, Tony, Dan and Mike that made the office hours very fun☺

Since this work is the result of collaboration within different departments of University of Bath and other institutes and companies, I would like to express my gratitude to:

- The MesMesh consortium (7th Framework) for their fruitful contribution to my work. Many thanks to all the people from Pera Innovations, Bolpal, University of Vilnius, Matrican and Müggler for the unforgettable meetings.

- Dr Stephen Pennock (Department of Electronic and Electrical Engineering) that as part of the MesMesh group helped in the success of the project.
- Mr Nick Gathercole (Department of Mechanical Engineering) that first as member of the MesMesh group and after that as very helpful colleague was always very happy to assist me with things that were not working!
- Mr Harry Bone (Department of Physics) for his help using the XRD.
- Dr John Mitchel and Mrs Ursula Potter (Microscopy and Analysis Suite) for their training and help when using the SEM.
- All the technicians that are always a key factor in experimental work.
- Dr Frank Clemens (High Performance Ceramics, EMPA Institute) for his help and expertise and the opportunity to visit and work in his lab. Together with Frank I would also like to thank all the students and researchers in EMPA that made my stay there feel like a holiday break☺.
- Dr Tim Mays (Department of Chemical Engineering) for the access to the thermo-gravimetric analysis equipment.
- Dr Richard G. A. Wills (Engineering and the Environment, University of Southampton) and Dr Maria Kourasi for a very nice and fruitful collaboration.
- Dr Rajnish Kurchania (Department of Physics, Manit Bhopal) and Dr Richard Ball (Dept of Architecture and Civil Engineering) that gave me the opportunity to visit India. Also, special thanks to Dr Stella Papatzani that made this trip much better….and for the coffee breaks afterwards!
- All the students (Julia, Pascal, Mat and Graham) that as part of their projects contributed to my work.

Since the beginning of my studies my house is in Bristol, where I met amazing friends, who I want to thank for making a new city for me feel like home.

Even though they were quite far away back in Greece, they were part of my everyday life and kept me updated for everything that was going on back home. Filitsa, Eleni, Ntina and Fotini thank you……I know I know Fotini is not in Greece any more.

A huge part of my life is Margaritis, who I thank, appreciate and admire every day, so there is no need to add anything more here☺
My last thanks go to my mother and brother, that I've missed spending time with, but are always happy for me and help me in every way.
It was an amazing journey!

Abstract

Ti-suboxides (TiO_{2-x}) have been widely studied and tested for many potential applications, mostly for their tuneable electrical conductivity and chemical resistance. When the material has a low x ($0 < x < 0.10$), the dominant point defects in the structure consist of Ti^{3+} and Ti^{4+} interstitials and oxygen vacancies. However, for x=0.10-0.34 (Magnéli phases) the lattice is characterised by extended planar defects and crystallographic shear planes that offer metallic conductivity (10^4 S/m). Depending on the extent of the reduction their properties can be tuned to match the requirements of various applications such as cathodic protection, batteries, catalyst support for fuel cells and optical memory devices. This research has focused on the manufacture and characterisation of Magnéli phases fine scale fibres, with the aim to use them in a wear sensor and as electrodes in redox flow batteries. The manufacturing process was optimised to tune the properties and achieve reproducibility. A main part of the work was studying the electrical properties using Impedance Spectroscopy to analyse the electrical response of the samples across a wide range of frequencies. Additionally, the structure, density/porosity, hardness, wear rate, thermal expansion coefficient and the thermal stability were investigated to match the requirements of the applications. Thermal stability is the main disadvantage of Ti-suboxides, since a high temperature and oxygen rich environment can cause re-oxidation. Thermo-gravimetric analysis was used to determine the re-oxidation temperature and the kinetic mechanism. The

Magnéli phases fibres were successfully used as the sensing element in a wear sensor that was based on resistivity measurements. They also gave very promising results when tested as electrodes for redox flow batteries.

Contents

List of Figures

Glossary

A	Area
a	Mass change
AC	Alternating current
Ag	Silver
Al	Aluminium
AMPRI	Advance Materials and Process Research Institute
APS	Atmospheric Plasma Spray
B	Susceptance
C	Capacitance
CAES	Compressed air energy storage
CNT	Carbon Nanotubes
d	Depth
D1	One dimensional diffusion model
D2	Two dimensional diffusion model
D3a	Three dimensional diffusion model-Jander
D3b	Three dimensional diffusion model-Ginstling-Brounshtein
DC	Direct current
E_a	Activation energy
ECES	Electrochemical energy storage
EDX	Energy dispersive X-ray
EMPA	Swiss Federal Laboratories for Materials Science and Technology
ETH	Swiss Federal Institute of Technology in Zurich
f(a)	Diffusion kinetic model function
FEMs	Federation of European Materials Societies
G	Conductance
HV	Vickers hardness
HIP	Hot Isostatic Pressing
IIT	Indian Institute of Technology
IS	Impedance Spectroscopy
L	Length

LCR	Meter of inductance (L), capacitance (C), and resistance (R)
LDPE	Low density polyethylene
MRVS	Micromechanical Resonant Vibration Sensor
MANIT	Manuala Azad National Institute of Technology
MAX	M-early transition metal, A-element from group A, X-Carbon or Nitrogen
MEET	Materials for Energy Efficiency in Transport
MHV	Mean Vickers hardness
O	Oxygen
Ø	Diameter
p	Dc resistivity
p*	Ac resistivity
p_b	Bulk density
PEG	Polyethylene glycol
PHES	Pumped hydro-power energy storage
p_s	Solid density
Pt	Platinum
R	Resistance
R	Gas constant
RC	Resistor-capacitor
RFB	Redox flow battery
RT	Room temperature
SEM	Scanning electron microscopy
SHM	Structural health monitoring
St.Acid	Stearic acid
TEC	Thermal Expansion Coefficient
TEM	Transmission electron microscopy
T_g	Glass transition temperature
TGA	Thermo-gravimetric analysis
Ti	Titanium
v	volume
w	Width

w	Actual weight
w_f	Final weight
w_o	Initial weight
wt	weight
XRD	X-ray diffraction
Y	Admittance
Z	Impedance
Z’	Real part of impedance
Z’’	Imaginary part of impedance
ε	Relative permittivity
ε_o	Permittivity of free space
π_a	Apparent porosity
σ*	Ac conductivity
Ω	Ohms (Resistance)
ω	Frequency (Angular frequency: 2πω)

1. Introduction and background

The introductory chapter provides the reader with an overview of the research on Magnéli phases (Ti_nO_{2n-1}) that is the focus of this work. The Magnéli phases meet the requirements of two applications that are presented in this thesis. The final part of the current chapter describes the structure of this thesis.

The focus of this work is on the Magnéli phases conductive ceramics. Rutile TiO_2 is a well-known semiconductor behaving as a n-type semiconductor. Following a high temperature treatment in a reducing atmosphere titania sub-stoichiometric oxides of a general type of Ti_nO_{2n-1} are created, having a metallic conductivity. This work will focus on manufacturing and characterisation of Magnéli conductive fibres in order to tune their properties and meet the requirements for potential applications.

Initially, this work was part of an EU 7th framework project, MesMesh, whose focus was to develop a prototype mould with a built-in wear sensor. The aim of the project was to create a low cost innovative thin conductive ceramic mesh to monitor wear on a steel surface, in order for the end users to be able to reduce their scrap and prolong the life time of their equipment. A key aspect of the MesMesh concept is the ability to measure the level of wear occurring on the surface of the steel substrate without the need to dismantle the system for microscopic examination. The proposed system consisted of a sensor grid incorporated into the outer surface layer of the steel part. The sensor grid system was to be created by micromachining smooth walled, depth controlled grooves into the metal surface using a femtosecond laser at a project partner (Vilnius University). The grooves in the steel substrate are then filled with an insulating ceramic material into which a conducting ceramic fibre is inserted (which is thus electrically isolated from the steel substrate). The conductive material needs to be chosen to have a resistivity that is large enough to realise an easily measurable change in resistance (e.g. order of 100 Ω) when the surface is worn down by not more than 5 μm. It will be shown in the thesis that Magnéli phases meet the basic requirements for this application, since they are sufficiently conductive to provide a measurable change in resistance as material is being removed from the surface and the thermal expansion coefficient and the wear resistance are similar to those of steel for high density ceramic samples.

As the research progressed and knowledge on Magnéli phases was gained, a new collaboration with University of Southampton was initiated with Dr Richard Wills and Maria Kourasi (PhD Student) who conduct research on Redox

Flow Batteries (RFB). Briefly, the name 'redox' refers to chemical reduction and oxidation reactions employed in the RFB to store energy in liquid electrolyte solutions, which flow through a battery of electrochemical cells during charge and discharge. The Magnéli phases meet the requirement of electrical conductivity and additionally they have adequate mechanical properties to perform as electrodes and chemical resistance, but there is a need for increased surface area to perform better as electrodes.

In more detail, this thesis provides the reader with a background on the applications, the state of art and the material requirements in the literature review in chapter 2. Additionally, chapter 2 presents the initial material selection process and the aims and objectives of the current research.

In chapter 3 the methods and equipment used to manufacture and characterise the materials are presented in detail. The Magnéli phases samples were manufactured in both bulk (tablet) and fine scale fibre form (Ø ~250μm) and the characterisation involved analysis of the physical and structural properties and determination of the electrical properties.

The initial tests and characterisation were performed on bulk dense samples. The manufacturing and characterisation of dense Magnéli phases tablets are presented in chapter 4.

Following chapter 4 and the manufacturing and characterisation of dense bulk materials, chapter 5 presents the manufacturing and characterisation of dense ceramic fibres, which were used in the prototype sensors.

In order to increase the surface area of the samples to meet the requirement of RFB electrodes, porous samples were also manufactured. Again, the initial tests involved porous Magnéli phases tablets and then during a visit in EMPA research institute in Switzerland, porous Magnéli phases fibres were manufactured and characterized. The work on porous materials is presented in chapter 6.

Chapter 7 presents the final stages of the MesMesh project that includes the integration of the prototype sensor and the testing of the sensor. The testing of the prototypes was undertaken in Pera Innovations Ltd, MesMesh partner.

The testing of porous samples as electrodes in RFB took place in University of Southampton and preliminary results are presented in chapter 8.

Finally, the thesis concludes with chapter 9 that summarizes the main conclusions and targets achieved within this PhD project and provides general considerations on how to improve some aspects of the research on Magnéli phases fibers and their applications. Future work topics are also suggested, since additional potential applications are already under investigation, followed by dissemination activities as part of this work.

2. Literature review

MesMesh was a 7th framework EU project that aimed to create a 'real time' sensor to monitor the surface wear of steel moulds for the moulding industry. This was needed in order to avoid faulty products and to be able to detect automatically the need for replacement of the mould. In addition, the materials under study were tested as electrodes for redox batteries. These two applications will be presented in detail, followed by the material selection to determine the appropriate material for the applications. Initially, the focus of the work was on two potential conductive ceramic systems, the MAX phase (Ti_2AlC) and the Magnéli phases ceramics. The structure and properties of both ceramics and a background review will be presented. Bearing in mind the requirements for the materials, the aims and objectives of this PhD will be presented at the end of this chapter.

2.1 Project background - Applications

A background review on wear sensors is presented, as well as the mode of operation for the MesMesh wear sensor. A background review on Redox Flow Batteries is also included in the current section. Both applications will set the requirements for the candidate materials.

2.1.1 Wear sensor

The focus of the MesMesh project was in the moulding industry and the aim was to develop a prototype mould with built in continuous structural health monitoring (SHM). Today there are no adequate means for measuring the surface damage of steel surfaces in industrial machinery during operation. This means that it is not possible to determine easily when to change a part or perform routine maintenance. By creating a low cost, innovative thin conductive ceramic mesh to monitor wear on a steel surface, it will be possible for end users to reduce their scrap and prolong the life of their equipment [1].

The proposed sensor system will allow gradual monitoring of the wear on the surface, compared to existing systems that allow only stepwise monitoring of wear. Existing patents and reported work on wear sensors mainly use optical fibres [2-4] or resistive paths [5-10] that are cut as material is removed and so the degree of wear is determined stepwise. These sensors find application in mechanical bearing systems, traction brake linings, cyclone dust separator linings, wear of the barrel wall in Diesel engines, cutting industry and quarrying industry [11]. *Figure 2.1* shows an example of a patented wear sensor that can measure wear in a stepwise manner since the wear damages the individual optical fibres and breaks the optical path [3]. Additionally, Figure 2.2 shows a schematic diagram of the principle of the wear sensors that use resistive paths to measure the wear. As material is removed due to wear the overall resistance of the system is expected to increase (following the equation for resistors in parallel: $R_{TOTAL} = (\frac{1}{R_1} + \frac{1}{R_2} + \cdots)$.

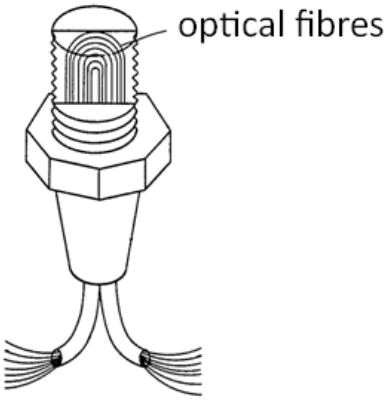

***Figure 2.1**: Wear sensor – the optical fibres are connected to the light source at one end and to the light receiving element at the other end [3]*

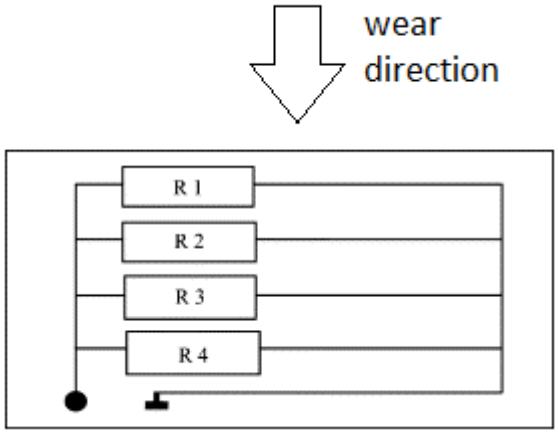

***Figure 2.2:** Schematic diagram of the resistive paths used to measure wear [6]*

Figure 2.3 and *2.4* present examples of two reported sensors for brake linings and the wear of the walls in Diesel engines respectively. They both use resistive paths in parallel so that as material is removed from the surface they get damaged and the overall resistance of the sensor changes.

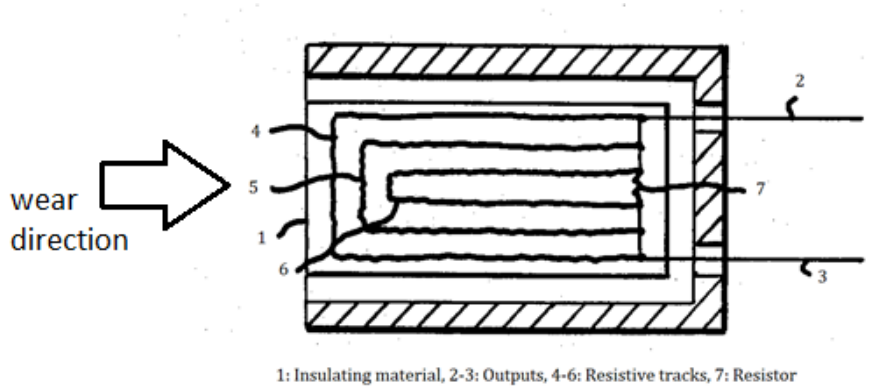

Figure 2.3: *A schematic diagram of a resistive multiple wear point sensor used in traction brake linings or cyclone dust separator linings [9]*

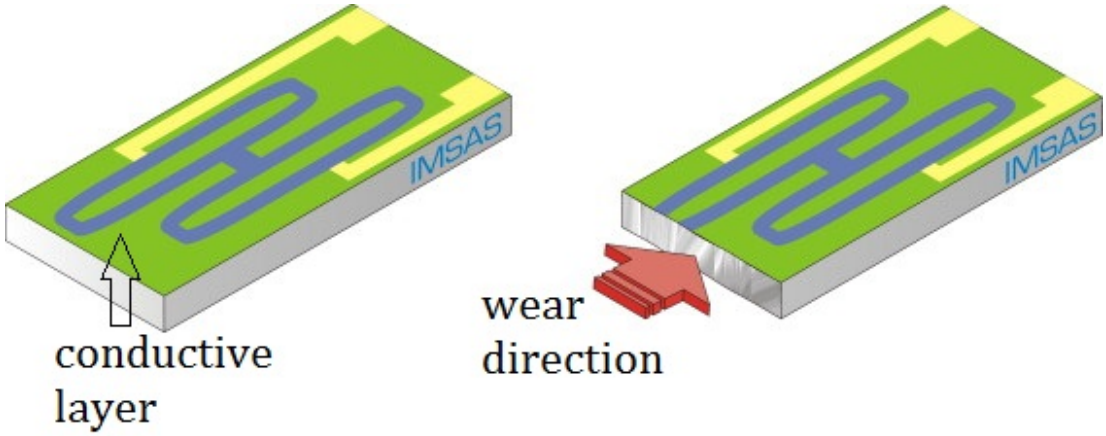

Figure 2.4: *A steel chip for wear measuring of the barrel wall in large Diesel engines [5]*

More 'gradual' sensing can be achieved by measuring an electrical resistance, which can be at the resolution determined by the sensitivity of the measuring equipment combined with the resistivity of the sensor element; this is in contrast to the approach used in *Figure 2.1* and *Figure 2.2* whereby wear leads to damage of individual optical fibres or resistors.

The general structure of the sensor elements proposed in this work is illustrated in *Figure 2.5*.

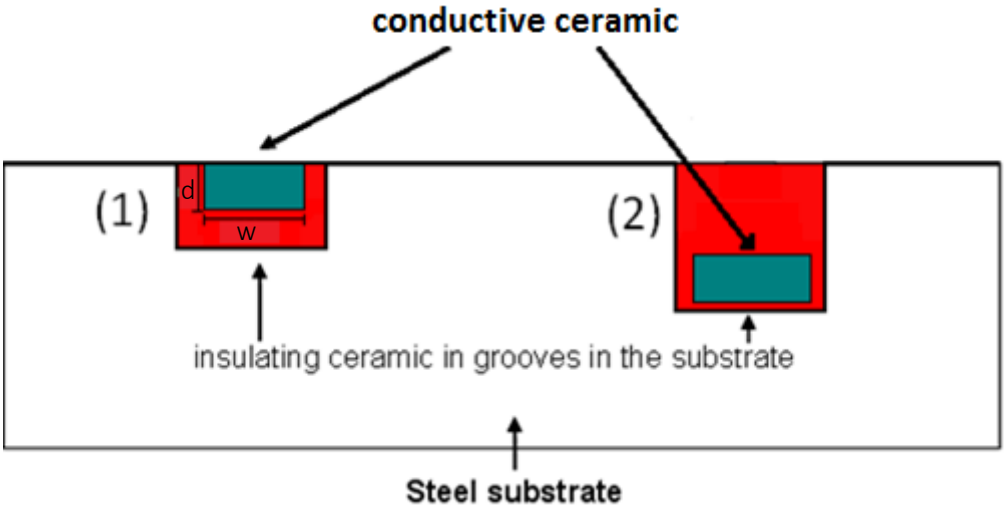

Figure 2.5: *Side view of the sensor showing the placement of the insulating (red) and conducting ceramic (green) in the grooves: (1) sensor element (2) reference element*

Groove (1) is used as the sensor element since wear will gradually change the dimensions and therefore the resistance of the sensor element (green section). Groove (2) is a reference element that is used to calibrate the sensor to changes in temperature, since the operating temperature of a metal part in industrial machinery can be up to 300^{o}C and this may lead to a change in the resistivity of the sensor ceramic. The dimensions of the conducting fibre to be made in this PhD will be on the order of 300 µm, since this is the depth the moulding industry is interested in monitoring [1].

As the steel mould material and the ceramic sensor fibre, are worn down the cross sectional area of the fibre decreases and its resistance increases. Assuming a rectangular (w x d) cross section with the parameters defined above and with length L:

$$R = \rho \frac{L}{wd}, \qquad \textbf{Equation 1}$$

where ρ is the resistivity of the ceramic element (fibre). Therefore if ρ, L , w (width) and d(depth) are assumed to be known constants, an observed change in the value of R (ΔR) results in a corresponding change in d (Δd). Measuring the DC (or low frequency AC) resistance of the ceramic fibres from one end to

the other and assuming a constant wear rate across the fibres leads to an average value of depth, Δd.

Taking a value of 20-100Ω as an easily measurable change in resistance (ΔR), if the depth (d) of the mould is reduced by 5μm using Eqn. 1 the desirable value of conductivity for the ceramic sensing element can be calculated. Therefore, with a ceramic fibre with dimensions L = 5 mm, w = d = 500 μm, the conductivity of the fibre should be in the order of 10^4 S/m (*Figure 2.6*).

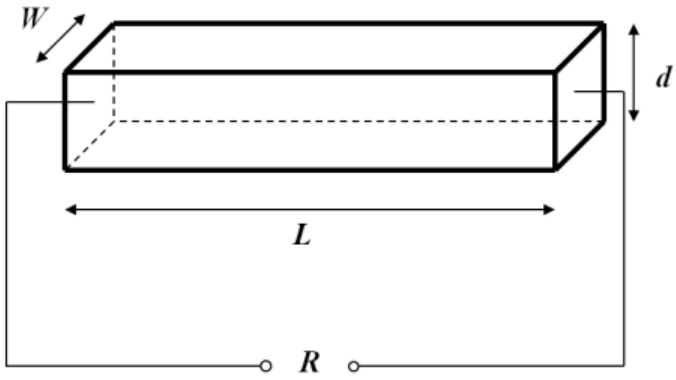

(a)

$$R_1 = \rho\frac{L}{wd_2}, R_2 = \rho\frac{L}{wd_1}$$

$$\Delta R = R_2 - R_1 = \rho\frac{L}{w}\left(\frac{1}{d_2} - \frac{1}{d_1}\right)$$

(b)

Figure 2.6: *(a) Dimensions of a single fibre, assuming rectangular geometry [12], (b) Calculations using eqn. 1 to determine optimal resistivity*

2.1.2 Electrodes for Redox batteries

In addition to generating energy from renewable sources, one of the most challenging problems is finding a way to store energy safely and efficiently, since these sources can be unreliable and intermittent. With the world population expected to grow from 7 to 9 billion by 2040 [13], the world's energy demand is expected to increase significantly. Taking into consideration the importance of reducing CO_2 emissions, an energy storage solution is even more urgent in order to achieve large scale energy storage systems that can release the energy on demand.

Energy storage systems exhibit a wide range of technological approaches to managing power supply, such as electrochemical energy storage (ECES),

flywheels, compressed air energy storage (CAES) and pumped hydro-power storage (PHES) (*Figure 2.7*). These energy storage systems are suitable for different storage and localisation needs. Pumped hydro-power is one of the most established energy storage technologies. A hydroelectric dam relies on water cascading down through a turbine to produce electricity. In order to store energy, water is elevated into a pool behind the dam, creating an on demand energy source. The disadvantage of the PHES is that the plants need to be sited in mountain regions with appropriate differences in water levels, so they have an environmental impact and are often threatened by long-term reservoir filling with sedimentary depositions [14]. Compressed air energy storage (CAES) is suitable for large plants and is also liable to site issues since compressed air needs to be stored i.e. in large underground caves. CAES also covers similar energy management service as PHES and in order to improve efficiency and the storage options, high investments costs are required [15]. A flywheel is a rotating mechanical device that is used to store kinetic energy that can be released instantaneously. A flywheel contains a spinning mass in its centre that is driven by a motor. To release energy, the spinning force drives a device similar to a turbine to produce electricity, slowing the rate of rotation. Its rotational speed is once again increased using the motor to recharge. High energy density and rapid energy release are their main advantages. A disadvantage is the design scaling [16].

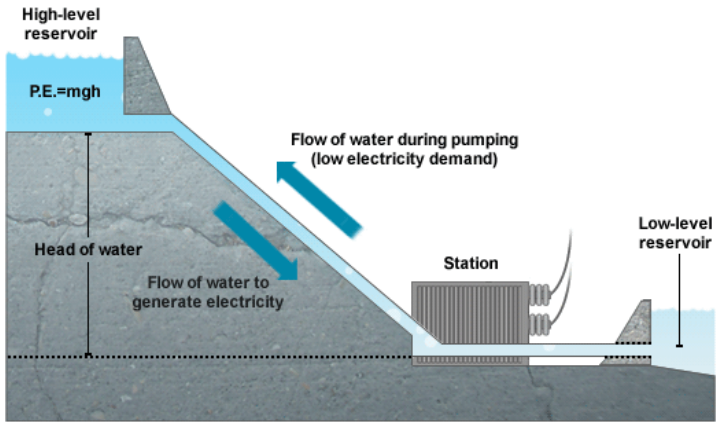

(a) - PHES

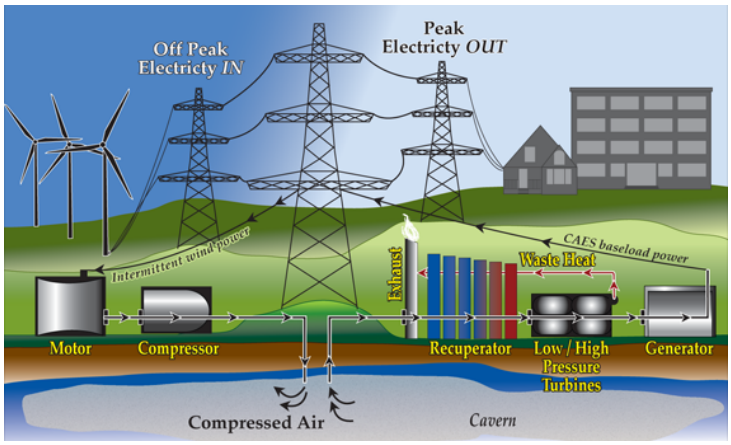

(b)-CAES

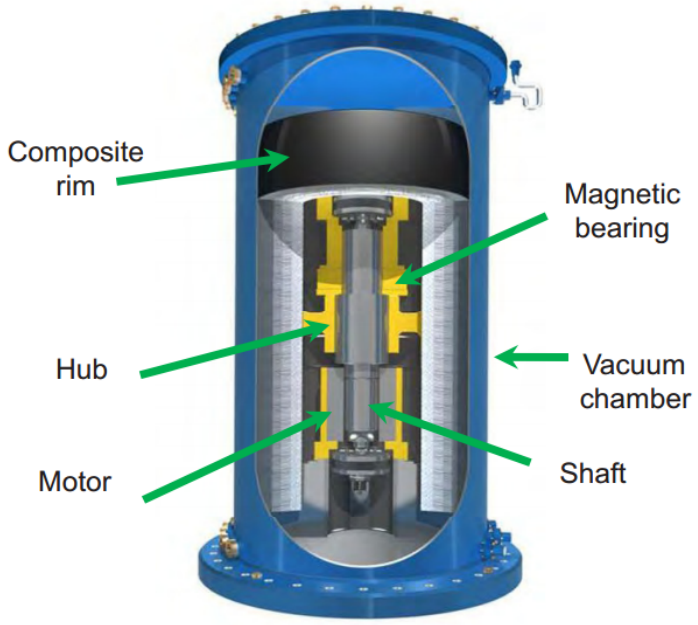

(c)- flywheels

Figure 2.7: *Schematic representations of energy storage systems [17]*

Several surveys show that electrochemical energy storage systems are the solution for intermittent renewable energy generators because of their site versatility, modularity that allows wide scalability, ease of operation and static structure. They are expected to have wide implementation in the coming years as distributed storage systems and substantial funds [18] have been already allocated for their scientific and technological development. A specific feature of ECESs is that deep discharges strongly affect the battery life and consequently producers specify a depth of discharge less than 100% [19]. Another feature of

most ECESs is that the same device provides both power conversion and energy storage that allows for very compact systems, but at the same time, bonds power to energy sizing [19]. Among the electrochemical systems, flow batteries represent one of the most recent and promising technologies. A flow battery is a type of rechargeable battery where rechargability is provided by two chemical components dissolved in liquids contained within the system separated by a membrane. One of their biggest advantages is the almost instant recharge by replacing the electrolyte liquid, while the spent material for re-energization [17]. Various classes of flow batteries exist including the redox (reduction–oxidation) flow battery. The name 'redox' refers to chemical reduction and oxidation reactions employed in the RFB to store energy in liquid electrolyte solutions which flow through a battery of electrochemical cells during charge and discharge. During discharge an electron is released through an oxidation on the negative (anode) of the battery. The electron is accepted on the cathode of the battery. The direction of the current and the chemical reactions are reversed during charging. A key distinction of RFBs is that the electrolyte is stored externally so that the power and energy requirements are independent of each other. The separation of power and energy also provides design flexibility in the application of RFBs, in this way the storage capability can be designed for the needs of a specific application. Also the electrodes are protected since they do not contain active material and so they are not consumed over time as in solid state batteries. However, potential dissolving of the electrodes though corrosion is an issue. *Figure 2.8* shows a schematic representation of a redox flow battery in which both half-cells are shown to be connected to external storage tanks providing the needed volume of electrolyte solutions circulated by pumps [20].

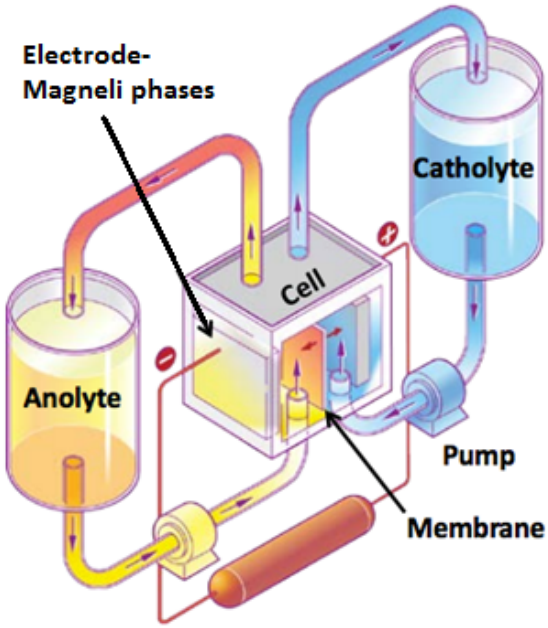

Figure 2.8: *Schematic representation of redox flow battery [21]*

2.2 Candidate materials for wear sensor and RFB electrodes

This section describes the process of material selection for the two applications considered and the characteristics that make the MAX phase (Ti_2AlC) and the Magnéli phases (Ti_nO_{2n-1}) attractive for these applications.

2.2.1 Candidate materials for the wear sensor

Initially, University of Bath, as a partner of the MesMesh EU project, carried out an extensive literature review of conductive ceramics and produced a guideline for the material selection, requiring further experimental research. According to the mode of operation of the wear sensor and the calculations of the resistance difference as described in section 2.1.1 the optimal resistivity of the conductive fibres that will be the sensing element in the sensor is in the range of 10^2-10^4 S/m. The hardness provides an estimate of the wear rate that needs to be similar between the steel and the sensing element so that the sensor measurement can be related to the wear of the steel surface. The hardness of the sensing element needs to be in the range of 700-800 Vickers, however further wear measurements were conducted as part of this work. Additionally, for the material selection the Thermal Expansion Coefficient (TEC) needs to be

taken into consideration since the operation temperature of the sensor maybe rise to 300^{o}C and therefore any difference in the TEC may result in fracture and damage of the soldering between the sensing elements and the steel surface. It is also important that the insulating component is chosen to perform as a bridge to match the TEC of the different soldering components and offer stress-free soldering, therefore the TEC of the solder glass needs to be matched to the components. *Figure 2.9* shows an Ashby diagram of the hardness (Vickers) against the thermal expansion coefficient providing ceramics that meet the application requirements, that are shown by a small box in the diagram (hardness: 700-800 Vickers, TEC:8-12x10^{-6} K^{-1}). None of these ceramics, however, meet the conductivity requirement for the active/conductive element of the sensor. Glass ceramic MACOR, TiO_2 and Al_2O_3 are materials that, as presented in *Figure 2.9*, could be used as insulating ceramic since their hardness and TEC are within the required range. The graph in *Figure 2.10* shows an Ashby diagram of the TEC against the electrical resistivity and the area of interest as a box. The only ceramic within the requirements is MAX phase (Ti_2AlC), however its hardness is much lower than needed. Therefore, in order to combine all the properties the focus moved to novel ceramics, like MAX phases (Ti_2AlC), titanium suboxides (Ti_nO_{2n-1}), SiAlON and Carbon nanotubes (CNT) composites as their conductivity and hardness can potentially be tuned. Table 2.1 summarises the required thermal and electrical properties of potential conductive ceramic candidates to be used in the MesMesh project, including the properties of the insulating ceramic and the steel substrate into which the sensor is embedded.

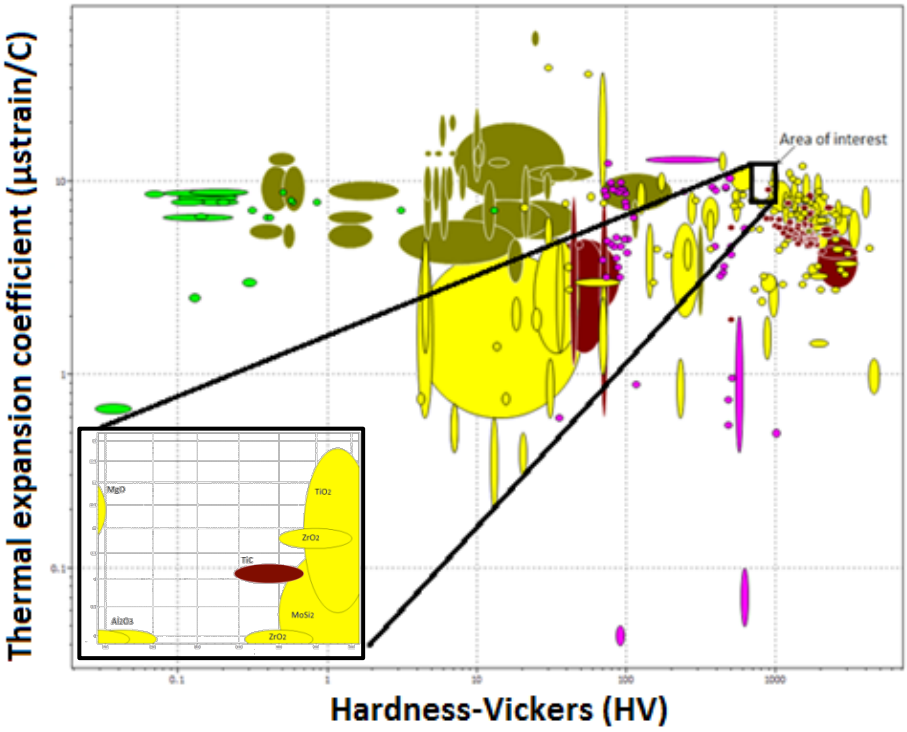

Figure 2.9: *A plot of hardness (Vickers) of various ceramics against the thermal expansion coefficient*

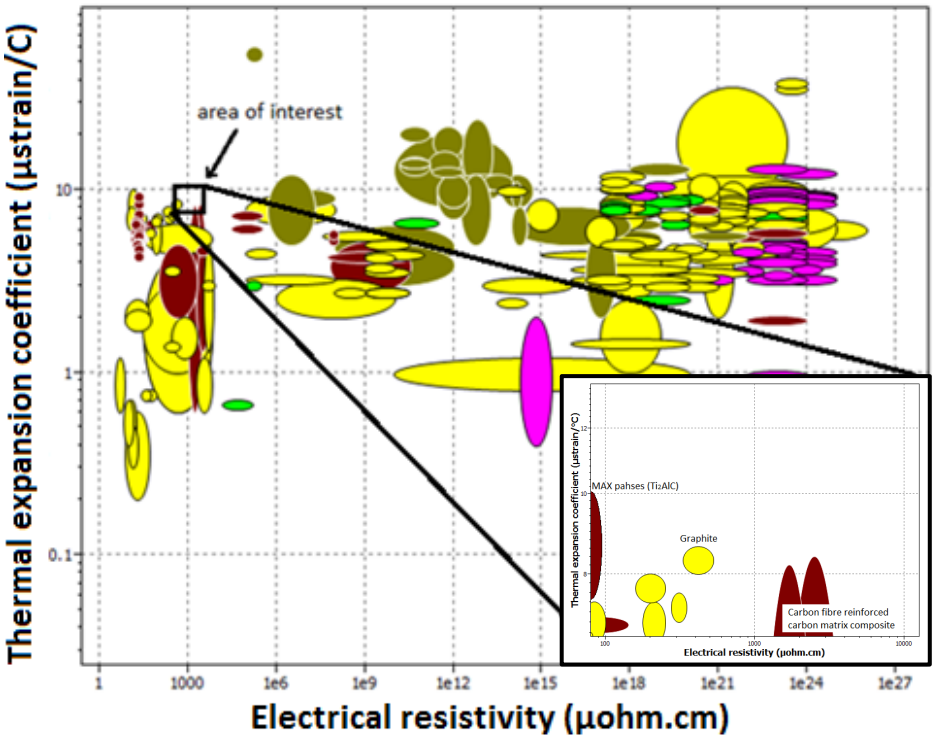

Figure 2.10: *A plot of the thermal expansion coefficient of various ceramics against the electric resistivity (µΩ/cm)*

Table 2.1: List of desired properties and candidate materials for the wear sensor

	Conductive Fibre	**Insulating (buffer) Component**	**Substrate: Hardened Steel**
Optimal Electrical Conductivity (S/m)	$10^3 – 10^4$	$>10^8$	$<10^{-9}$
{Optimal Electrical Resistivity(μΩ/cm)}	10^4-10^5	$>10^{15}$	$<10^{-1}$
Hardness (Vickers)	700 – 800	700 – 800	780
Linear Thermal Expansion Coefficient (K^{-1})	8 – 12 x 10^{-6}	10 – 12 x 10^{-6}	Expected: 12 x 10^{-6} Measured: 13 x 10^{-6}
Candidate Materials	CNT composites SiAlON (SiC/TiB_2) Titanium suboxides (Ti_nO_{2n-1}) MAX phases (Ti_2AlC)	Glass/Vitreous enamel MACOR (glass-ceramic) Titanium dioxide (TiO_2) Aluminium oxide (Al_2O_3)	-

Therefore, based on Table 2.1, the initial experimental work on the candidate ceramic materials to be used for the mesh sensor was performed and focussed on the following properties:

(i) electrical properties (conductivity)

(ii) thermal properties (thermal expansion coefficient to minimize thermal stresses)

(iii) hardness (to correlate the wear of the sensing element with that of steel).

Carbon nanotube (CNT) composites can have high density and the electrical properties can be tuned within the range of interest of the MesMesh sensor. However since these systems use a polymer matrix the hardness will not reach that of steel [22]. On the other hand, the SiAlON ceramic alloy systems (silicon, aluminium, oxygen and nitrogen) have an electrical conductivity within the desirable range by the addition of conductive particles such as SiC and TiB_2. However, they have a much higher hardness of up to 1700 Vickers leading to potentially very different wear rates to that of steel (780 Vickers) [23].

Therefore, regarding the potential conductive ceramics, the focus has been on Magnéli Phases (Ti_nO_{2n-1}) and MAX Phases (Ti_2AlC) that will now be described [24].

Conductive ceramic: MAX phase (Ti_2AlC)

MAX phase is a novel class of ceramic materials with interesting properties and is represented by the family discovered by Nowotny [25]. These materials have been named MAX phases [26] and are ternary compounds with the general formula $M_{n+1}AX_n$ where n= 1 to 3, M is an early transition metal (Ti, V, Zr, Ta), A is an element from A group (mostly IIIA such as Al and IVA such as Si) of the periodic table and X is either carbon (C) or nitrogen (N), as highlighted in *Figure 2.11*. They are hexagonal layered compounds, where pure layers of the A-group elements are interleaved with M layers having the rock-salt structure (*Figure 2.12*).

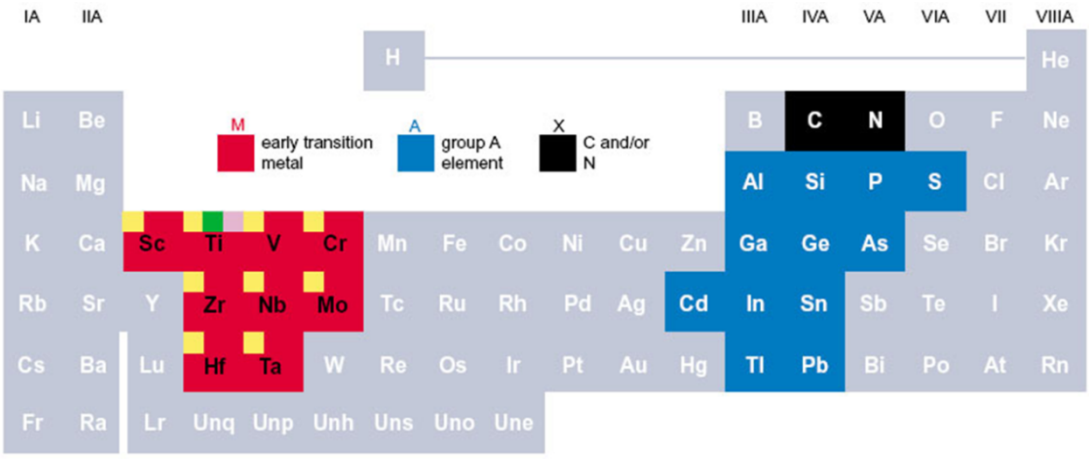

Figure 2.11: *Elements forming MAX phases are highlighted in this period table. M is an early transition metal, A an element from group A and X is either Carbon or Nitrogen [26].*

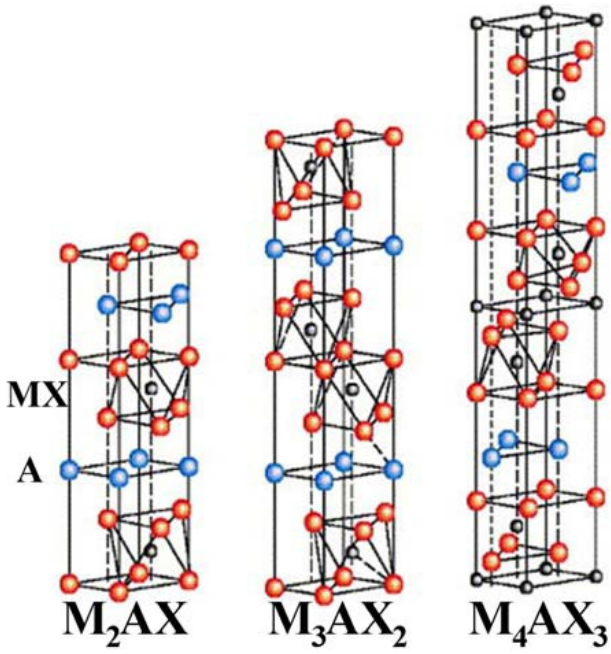

(a) (b) (c)

Figure 2.12: *Unit cells of the $M_{n+1}AX_n$ phases for (a) n = 1 or M_2AX, (b) n = 2 or M_3AX_2, and (c) n = 3 or M_4AX_3 phases, and (d) M, A, and X elements that form the MAX phases[27]*

MAX phases are interesting from an electrical perspective because they are electrically (metallic type) conductive ceramics [26-28]. The thermal expansion coefficient of MAX phases is reported to be in the range 7.5 to 10 x 10^{-6} $°C^{-1}$ [26]; this property is of interest to avoid thermal mismatch problems when the ceramic is embedded in the steel substrate. Electrical resistivity is in the range of 36 μΩ·cm at room temperature and increases linearly with increasing temperature (in a similar fashion to metals) [29]. This makes MAX phase a candidate material for the present sensor application since the ideal material should exhibit a resistivity in the range 10^4 to 10^5 μΩ·cm. MAX phase also has some additional characteristics unusual to ceramics. They are readily machinable but quite stiff (E=275-305 GPa) [30], resistant to thermal shock and damage tolerant. The good mechanical properties are a result of the localised lattice distortions that allow the delamination of multiple layers of the structure (*Figure 2.13*) [30].

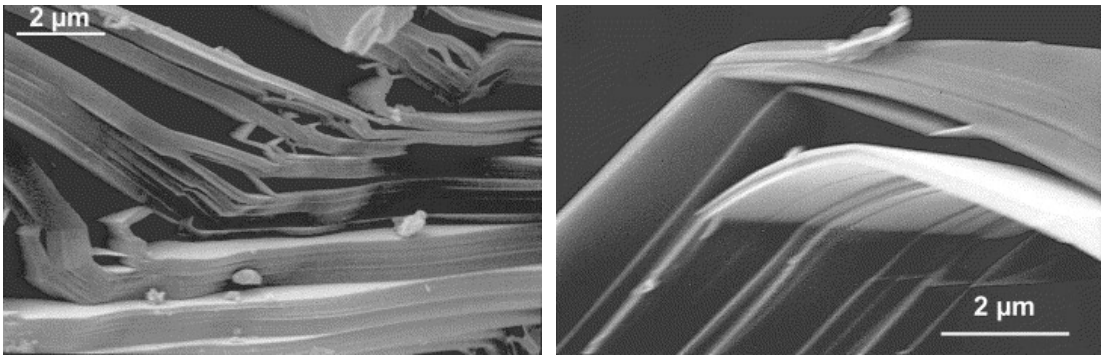

Figure 2.13: *Typical examples of the nano laminated nature of the MAX phase [30, 31]*

Another advantage of Ti_2AlC is that it has excellent oxidation resistance due to it being an alumina former [32], which means it can be used in high temperature applications and still maintain its mechanical properties. More specifically, focusing on the wear sensor application, the thermal expansion coefficient (TEC) is within the range of requirements ($8.55\pm0.24x10^{-6}$ K^{-1}) [33]; similar to steel (13×10^{-6} K^{-1}), however the hardness is lower than needed for the sensor (250-450 HV) [34]. A basic disadvantage of the MAX phase ceramics is the high cost and energy associated with the manufacturing process, in particular the need for high temperature processing and shaping of the sintered material [35].

Conductive ceramic 2: TiO_2 and Magnéli phases (Ti_nO_{2n-1})

Titanium dioxide (TiO_2) is the most important compound of titanium and oxygen and it exists in several crystalline forms. The most common forms are *rutile, anatase* and *brookite*. These structures are formed of TiO_6 octahedra in different arrangements [36]. The most common form is rutile which is the equilibrium phase at all temperatures (*Figure 2.14*). TiO_2 is a poor electrical conductor that due to defects – oxygen vacancies – performs as an n-type semiconductor.

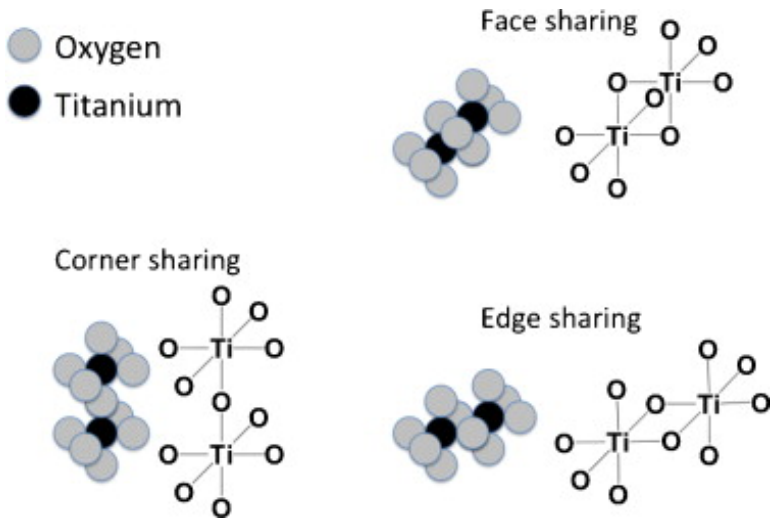

Figure 2.14: *Orientations of TiO_2 octahedra [37]*

It is known that the electrical conductivity of titanium dioxide can be significantly increased by treating the oxide at a high temperature in a reducing atmosphere, usually in the presence of hydrogen [38] or carbon [39]. The process leads to the formation of sub-stoichiometric oxides of general formula Ti_nO_{2n-1} (with 3 <n< 10), known as Magnéli phases [40]. In non-stoichiometric titanium dioxide, TiO_{2-x}, with low x (0 <x< 0.10), the dominant point defects in the structure consist of Ti^{3+} and Ti^{4+} interstitials and oxygen vacancies[41]. However, the Magnéli phases (x=0.10-0.34) are characterised by extended planar defects and crystallographic shear planes which vary according to the oxygen deficiency [42, 43] (*Figure 2.15*).

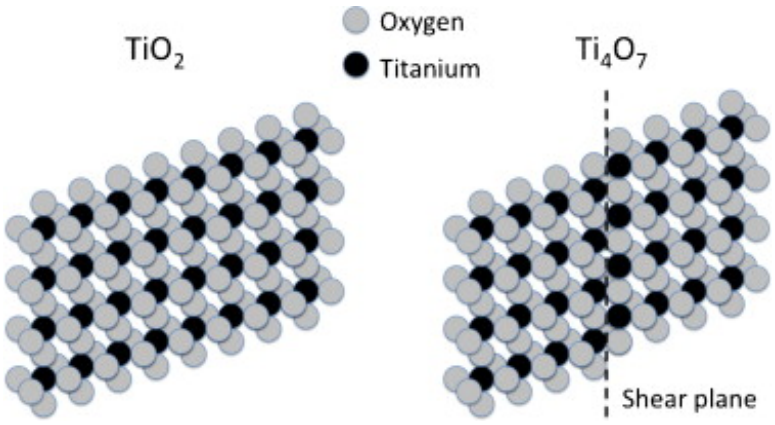

Figure 2.15: *Edge-sharing TiO_2 and Ti_4O_7 octahedra structures [37]*

In more detail the crystal structure of the Magnéli phases (Ti_nO_{2n-1}) is related to that of rutile TiO_2 and consists of rutilelike blocks which are infinite in two dimensions and *n* oxygen-octahedra wide in the third [44]. Along the plane separating these blocks, the octahedral share faces, edges and corners, while inside the blocks they share only edges and corners [45]. This causes the titanium-atom positions in one block to correspond to unoccupied or interstitial positions in the next block [46]. The crystallographic shear plane and vector for the Magnéli phases are $(121)_{rutile}$ and $\frac{1}{2}[0\bar{1}1]_{rutile}$, respectively. The shear vector corresponds to a vector connecting a position of oxygen ion with another in the bc-plane, thus resulting in no disturbance in the oxygen arrangement. However, the titanium arrangement is disturbed since the shear vector moves titanium ions in the octahedron formed by six ions to the interstitial octahedral positions (*Figure 2.16*) [47]. As a result, the oxygen deficiency occurs on the shear plane and homologous series of Magnéli phases with various Ti/O ratios are formed by changing the spacing of the crystallographic shear plane.

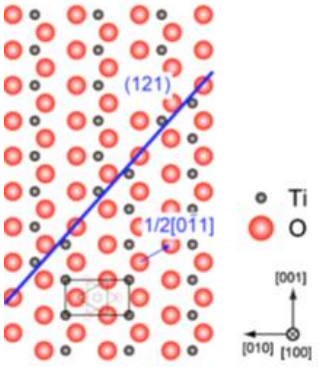

Figure ***Error! No text of specified style in document****..1: Schematic illustration of crystallographic shear structure of Magnéli phases [47]*

As an example the atomic arrangement in Ti_6O_{11} Magnéli phase is schematically illustrated in *Figure 2.17*, where the oxygen deficiency and the disturbance of the titanium ion arrangement is evident to occur at the crystallographic shear plane.

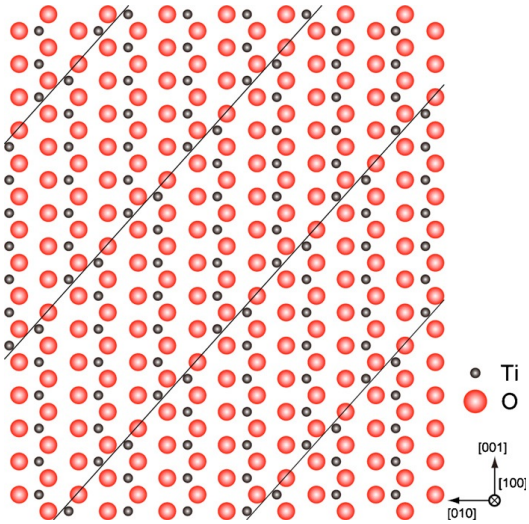

***Figure 2.17**: Schematic illustration of ideal structure of Ti_6O_{11} (n=6) crystallographic shear structure [47]*

Figure 2.18 shows a high-resolution TEM image of the Ti_6O_{11} Magnéli phase and as discussed the crystallographic shear structure is formed by introducing the shear planes parallel to $(121)_{rutile}$ every six pure titanium planes. Another example of high-resolution TEM on Magnéli phases is shown in *Figure 2.19* where the shear planes are marked with arrows.

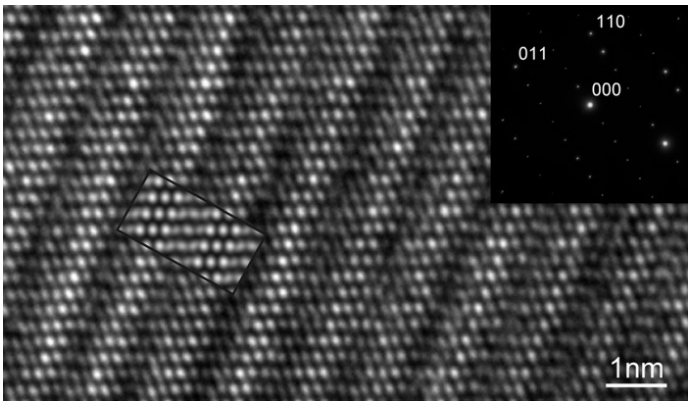

***Figure 2.18**: A high-resolution TEM image of the Ti_6O_{11} Magnéli phase [47]*

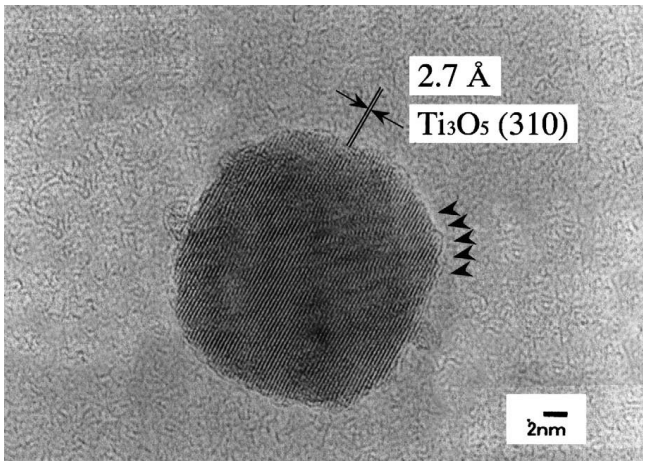

***Figure 2.19**: A high-resolution TEM image of the Ti_3O_5 Magnéli phase [48]*

The structure of TiO_2, TiO_{2-x} and Magnéli phases has been studied in extent between 1970 and 1985, when Y. Le Page at al. published a series of papers in journal of Solid State Chemistry calculating the cell parameters of Magnéli phases [49-51]. In 1970 J. S. Anderson and R. J. D. Tilley studied in detail the crystallographic shear in oxygen-deficient rutile, observing that starting from stoichiometric rutile TiO_2 and moving towards structures with increased oxygen-deficiency there are disordered shear planes created that become more ordered as Magnéli phases (Ti_nO_{2n-1}) form [52]. A lot of work was also published regarding the electrical properties of oxygen deficient rutile in an attempt to find a model to describe the conductivity mechanism [53, 45, 46, 54].

More recently, a mixture of predominately Ti_4O_7, Ti_5O_9 and Ti_6O_{11} Magnéli phases is trademarked under the name of Ebonex and it is of interest in a variety of applications due to its electrical conductivity (10^4 S/m) and chemical resistance. Among the potential application areas are cathodic protection, batteries, catalyst support for fuel cells as well as their potential use in the treatment of aqueous waste and contaminated water [37, 55, 56]. In recent work Magnéli phases and more specifically Ti_3O_5, have been tested for an optical memory device using the reversible, photoinduced phase transition between λ-Ti_3O_5 and β-Ti_3O_5 at room temperature [57]. The reported work on Magnéli phases for these applications focuses on manufacturing bulk samples used as substrates or coatings. A comprehensive understanding of the electrical properties of Magnéli phases is crucial to the progress of the above mentioned

fields. The dc electrical conductivity of Ti_nO_{2n-1} has been studied by Bartholomew and Frankl [58] and Inglis *et al.* [59] and in both studies, a transition in the conductive mechanism from semiconducting to metallic was observed at around 150K and up to room temperature. Most recent work has also focused on providing an insight into the conductivity mechanism of Magnéli phases [39]. The difficulty in characterizing and understanding the electrical properties of Magnéli phases lies in the fact that the various sub-oxides cannot be produced separately. Optimisation of the manufacturing process can lead to the production of a single phase in a high percentage, however isolating a single phase is difficult. A variety of models have been proposed to describe their structure and predict their properties [60-62].

The Magnéli phases can be manufactured either by heating TiO_2 with metallic titanium under an inert atmosphere:

$$(\mathbf{1/2})\boldsymbol{Ti} + (\boldsymbol{n} - (\mathbf{1/2}))\boldsymbol{TiO_2} \xrightarrow{\boldsymbol{Heat}} \boldsymbol{Ti_nO_{2n-1}}, \qquad \textbf{Equation 2}$$

or by reducing TiO_2 at high temperatures using a reducing agent such as hydrogen gas:

$$\boldsymbol{nTiO_2} + \boldsymbol{H_2} \xrightarrow{\boldsymbol{Heat}} \boldsymbol{Ti_nO_{2n-1}} + \boldsymbol{H_2O}, \qquad \textbf{Equation 3.}$$

In the case of using TiO_2 and metallic titanium the temperature needed is around 1200°C for over a week, whereas in the case of using a reducing agent on TiO_2 a temperature over 1200°C is needed for 1 to 8 hours [37]. Optimisation is necessary depending on the shape and size of the samples; since this would influence the diffusion during the reduction reaction. Other reducing agents such as carbon can also be used or catalysts to optimize the process [37, 38, 63, 64]. The temperature and the duration of the manufacturing process needs to be chosen carefully, depending on which manufacturing route is chosen, since at higher temperatures (>1400°C) TiC is likely to be formed [65, 66]. Usually rutile TiO_2 is used to manufacture the Magnéli phases, since as explained above the Magnéli phases have crystal structures derived from the rutile structure by

crystallographic shear. However, anatase TiO_2 has also been used as a raw material [67, 68]. However, a common factor in these studies is that the relation between conductivity and temperature is not linear. Thus, the defect structure cannot be interpreted in terms of a simple model in which either oxygen vacancies or interstitial titanium ions predominate. Both oxygen and interstitial titanium defects are important depending on temperature. In K. H. Kim et al study [53] conductivity is measured under a range of O_2 pressure and temperature and it is proposed that at lower temperatures (below 520K) oxygen vacancies as shallow donors are the predominant conduction mechanism, whereas at higher temperatures (>520K) the observed conduction is due to electrons that are thermally excited to the conduction band.

2.2.2 Candidate materials for flow batteries electrodes

An electrode in a redox flow battery needs to have high electrical conductivity, good mechanical properties, high chemical resistance and high surface area to increase the reaction rate. In addition, as cost is a significant factor in the feasibility of such batteries, the price and cycle life of the electrode are important parameters [69].

The existing electrode materials used for redox flow batteries are either metallic or carbon-based electrodes. However, the high carbon content required for good conductivity may result in reduced mechanical properties in the case of a polymer matrix [70]. CNT composites exhibit better mechanical properties and one-dimension conductivity, however impurities can affect these properties [71]. In addition, these materials are not stable enough due to corrosion in corrosive environments and in high electrode potential [69].

Magnéli phases can offer high electrical conductivity, in addition to good corrosion resistance and better mechanical properties, such as hardness. In addition, Magnéli phases have the advantage of a simple and inexpensive production method [37]. It is also important for the electrode to be porous in order to maximize the active surface area [72]. A larger surface area leads to an increase of the catalytic reaction rate, improving the response and power of the battery. In this context, the porous structure of a material can be divided into

microporous (<2nm), mesoporous (2-50nm) and macroporous (>50nm) [73]. Microporous ceramics offer very high surface areas, but as the pore sizes are small they can easily be blocked, not allowing the electrolyte to pass through. Mesoporous ceramics also provide significant surface area and additionally they are less likely to be blocked compared to a microporous system. A network of macropores would allow the electrolyte to flow through the material and reach the mesopores and micropores, as shown in *Figure 2.20*.

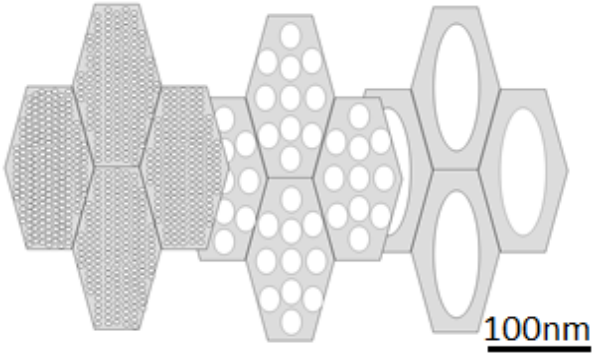

Figure 2.20: *Ideal electrode material structure with increasing pores size close to the surface*

The majority of the work on Magnéli phases as electrodes involves the use of Magnéli phases as substrates for catalytic coatings or as thin films [37, 74]. Typical electrodeposites include Pb (cathodic) and PbO_2 (anodic) [75]. The work of Magnéli phases thin films involves coatings obtained by Atmospheric Plasma Spray onto steel or nickel substrates [76, 77]. In the current work that the focus is on fine scale fibres and the final idea for their use as electrodes is to place them vertically on a substrate in order to increase further the surface area of the electrode system (*Figure 2.21*).

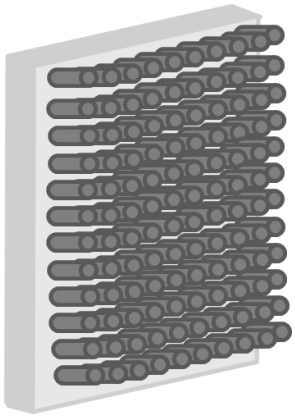

Figure 2.21: *Ideal electrode with Magnéli phases fine scale fibres maximizing the active surface area*

2.3 Aims and objectives

For the wear sensor application the initial focus of the work was to use MAX phase or Magnéli phases as the active material of a wear sensor based on resistance measurements in fibre form. Optimisation of their properties (such as electrical conductivity and thermal expansion) is necessary to meet the requirements for the wear sensor. In order to achieve that, the main goal of this work is to correlate the manufacturing process of the ceramics with their mechanical and electrical properties.

More specifically, regarding the wear sensor and the final material used as the sensing element the aims can be highlighted by the following points:

i. The wear sensor requires the sensing element to have a resistivity of 10^2-10^4 μΩ.cm in order to provide the best resolution in the measurement of resistance using simple electronics as the cross-section of the conductive fibres is decreased during wear. Therefore in order to use the MAX phase (Ti_2AlC) as the sensing element the resistivity needs to be increased by 2-3 orders of magnitude from 36 μΩ.cm to 10^2-10^4 μΩ.cm. On the other hand, the conductivity of the Magnéli phases is within the range of the electrical resistivity requirements, however the chemical reduction process is not an easily controlled process, so it

needs appropriate optimization in order to guarantee reproducible electrical results.

ii. Since the wear sensor is going to measure the material removed from the surface of the ceramic fibres, the fibres need to have the same wear resistance and hardness as steel in order to correlate the wear of the fibres with the wear of the steel surface. Regarding the MAX phase materials, the hardness is lower than steel, and ceramic alloying could be attempted to increase the hardness. Regarding the Magnéli phases the hardness is within the desirable range and the aim is simply to achieve high density samples. Since the reduction process occurs through diffusion, cracks and porosity may be present in the samples that results in poorer mechanical properties and unstable electrical properties. Therefore it is important to avoid cracks and porosity during the manufacturing and achieve highly dense fibres.

iii. Following the final material selection a method of integrating the wear sensor into a steel mould needs to be developed. It is essential to achieve good fibre-wire electrical bonds that have an ohmic electrical behaviour and be mechanically strong. In addition, the glass needs to offer strong soldering and good insulation from the steel to avoid the creation of electrical short circuits.

iv. Finally, in order to increase the performance of Magnéli phases as Redox battery electrodes there is a need to increase the surface area. Therefore the work focusses on increasing the porosity of the bulk samples initially and then fibres, but retaining the mechanical properties to a sufficient level. The increased porosity will affect the manufacturing of the green samples, especially the extrusion of the fibres. The porosity is also going to affect the reduction process, so further optimisation is needed.

In conclusion, there have been several studies on MAX phase and on Magnéli phases most of which focus on using both types of conductive ceramics for electrodes either as a substrate or in the form of a coating. Their electrical

conductivity and chemical resistance are the main characteristics that make them suitable for these applications.

3. Manufacturing and characterisation methods and equipment

The ‘green’ bodies (i.e. unsintered materials) were manufactured in both bulk form (tablets) and in fibre form and the equipment used for the manufacturing are presented in this chapter. For the sintering and the reduction of the samples to produce Magnéli phases materials, both chamber and tubular furnaces were used. In addition, this chapter presents the methods and equipment used to characterize the structure, the physical and electrical properties of the bulk materials and the manufactured fibres.

3.1 Manufacturing methods and equipment

The green bodies in tablet form were manufactured at the University of Bath and extruded in fibre form in EMPA Research Institute (ETH Domain). The equipment used to achieve a homogeneous feedstock and shape the green bodies are presented, together with the furnaces used for the sintering and reduction stages.

3.1.1 Ball milling

A ball mill is a type of grinder used to homogeneously mix powders and grind the mixture into fine powder by crushing any agglomerations present. The principle is that the size reduction occurs by the impact of the ceramic balls that drop from the top as the cylindrical container rotates about its axis (*Figure 3.1*). The balls used were zirconia and the ball milling device is a Capco, shown in *Figure 3.2*.

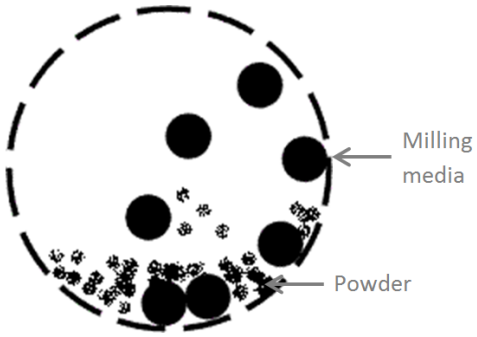

Figure 3.1: *Ball milling principle*

Figure 3.2: *Ball milling apparatus*

3.1.2 Uniaxial cold pressing

Uniaxial cold pressing is an inexpensive shaping method to produce simple shapes such as the tablets formed in this work. Uniaxial pressing involves the compaction of powder into a rigid die by applying pressure in a uni-axial direction through a piston. The parameters that affect the green bodies are the amount of powder fed into the die, the pressure applied, the rate and the duration of the pressure application. For example, a high ratio of height to diameter can lead to cracks or delamination [78]; low pressures can result in low density samples, whereas higher pressure can result in cracks during de-binding and sintering due to internal stress. The pressing devices used were a low and a high pressure device in the University of Bath and in EMPA respectively, both shown in *Figure 3.3*.

(a) *(b)*

Figure 3.3: *Uniaxial pressing devices in (a) University of Bath and (b) in EMPA*

3.1.3 De-binding, sintering and carbo-thermal reduction - Furnaces

For the shaping of the ceramic the use of a binder is essential in order to provide the necessary plasticity and the 'green' body to maintain the shape before firing. The most common method to remove them fully from the ceramic body is thermal decomposition. During decomposition, the binder is broken down into gaseous species and carbon that diffuse out of the body. The defects associated with the binder burn out include cracks, delamination, bubbling, blistering or voids and the parameters to control them are the heating rate and the duration

at the temperature that the binder burns out. Generally to avoid defects and shrinkage the heating rate should be low and for all the samples manufactured in this work the duration at the binder burn out temperature was 2 hours. The de-binding temperature was chosen depending on the specific binder used [79, 80], which was polyethylene glycol for the bulk samples and polyethylene for the fibres.

After de-binding a sintering step was necessary to densify the samples. Additionally, in the case of MAX phase ceramics a high temperature is necessary for the reaction to take place and form the MAX phase [35]. During sintering, densification occurs through grain growth and shrinkage and the sintering temperature depends on the specific material. For the formation of Magnéli phases the TiO_2 samples undergo a carbo-thermal reduction (*Figure 3.4*) under constant Argon flow to avoid re-oxidation [37]. After various trials, the optimal set up was to create a micro-environment for the reduction of the TiO_2, where the tablets or fibres were embedded in carbon black powder (Ø3.55μm, mean length=104μm), as shown in *Figure 3.5*.

$$nTiO_2 + \tfrac{1}{2}C \xrightarrow{\text{Heat}} Ti_nO_{2n-1} + \tfrac{1}{2}CO_2$$

Figure 3.4: *Reduction of TiO_2 using carbon as a reducing agent*

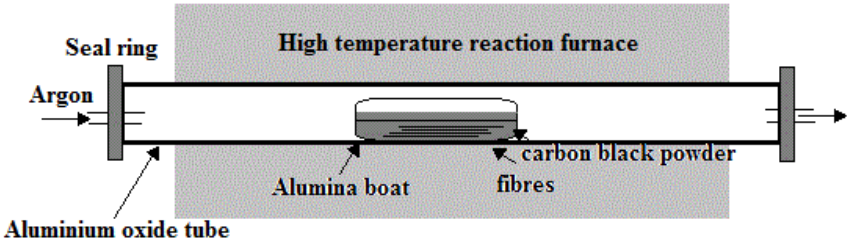

Figure 3.5: *Microenvironment for the reduction of TiO_2 in a tubular furnace*

As described in section 2.2.1 other processes could be used for the manufacturing of Magnéli phases, such as using hydrogen as the reducing agent. However, since an important aspect of the MesMesh project is to keep the

production costs of the wear sensor low, an inexpensive and easy to control carbothermal reduction was chosen.

During this work various furnaces have been used depending on the temperature and the atmosphere required. For de-binding and sintering in air, chamber furnaces were used up to 1300°C, *Figure 3.6* (a) and (b) show the chamber furnaces in University of Bath and in EMPA. For the heating treatments that needed to occur in a controlled atmosphere tubular furnaces were used in order to ensure a constant gas flow. The furnaces in University of Bath and in EMPA and their details are shown in *Figure 3.7*.

(a) *(b)*

Figure 3.6: *Chamber furnaces in (a) University of Bath (Elite Thermal Systems Limited, BRF14/10-2416CG) and (b) EMPA(Borel Special Furnaces, TH 1280)*

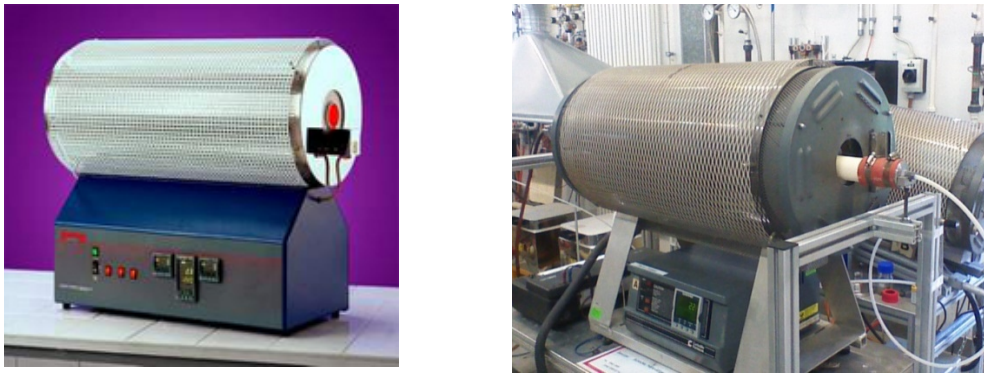

(a) *(b)*

Figure 3.7: *Tubular furnaces in (a) University of Bath (LTF 16/75/450, LENTON, UK) [81] and (b) EMPA(Borel Special Furnaces, TU 1400)*

3.1.4 Ceramic fibre extrusion - Capillary rheometer

Extrusion involves forcing a deformable material through the orifice in order to shape a green body of continuous cross-sectional area. The feedstock is fed from the rear of the extruder and transported along the barrel by axial movement of a piston. The process is widely used to produce components having a constant cross-section and a large length-to-diameter ratio such as rods, fibres and hollow tubes. This shaping method is applied to a wide range of materials, in the case of ceramics, a thermoplastic binder is mixed with the ceramic powder to offer the desired flow properties. During extrusion the driving force produced by the movement of the piston needs to be higher than the resistance of the feedstock and the die-wall friction. The main requirement for the ceramic extrusion process is to obtain a feedstock with the desired plasticity. Apart from providing the required plasticity the thermoplastic binders also offer handling strength [82].

To produce the green fibres in the current work a capillary rheometer was used. The rheometer offers controlled extrusion of a material and allows the material flow and deformation properties to be characterised during extrusion. The feedstock is loaded into a capillary die and the die is mounted into a bore in the temperature controlled barrel. The barrel has three heater bands in order to ensure temperature uniformity during processing. Before starting the extrusion process, the feedstock was heated in the barrel for approximately one hour to ensure homogeneous temperature distribution. The temperature was chosen after testing and it was different for the various feedstocks. The capillary rheometer used in EMPA is a RH7-2, Malvern, Herrenberg, Germany, shown in *Figure 3.8*a. *Figure 3.8*b presents a schematic representation of the barrel area.

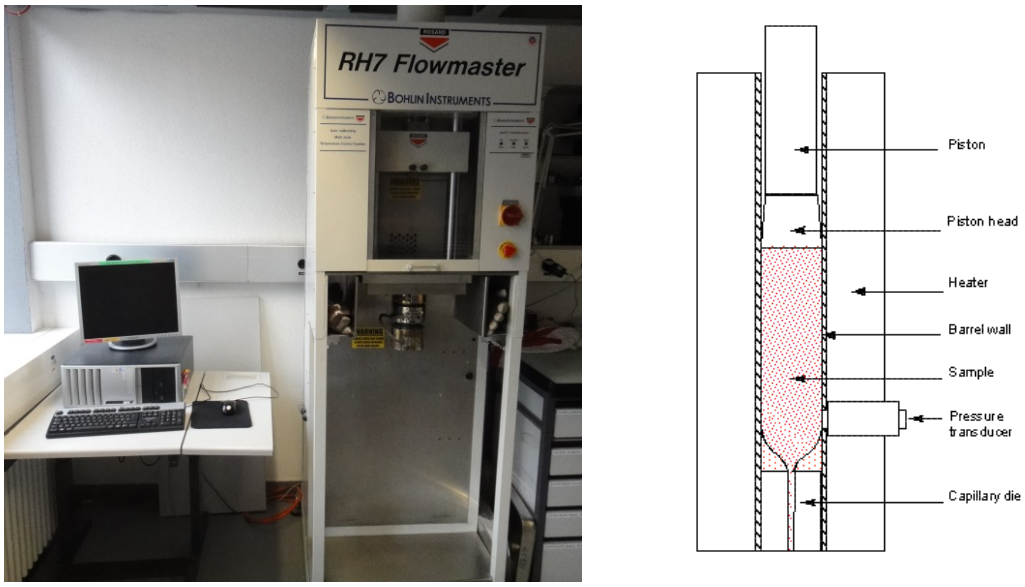

(a) *(b)*

Figure 3.8: *(a) Capillary rheometer in EMPA, (b) schematic representation of the barrel area [83]*

3.1.5 Feedstock preparation - Torque rheometer

When working with ceramic powders a thermoplastic binder, that ensures the required feedstock plasticity, is not the only requirement. A surface active agent (surfactant) can be added to the system in order to ensure that the binder wets the powder particles, in order to avoid phase separation between the powder and binder under pressure. The feedstock is prepared by directly mixing the raw materials and additives in a shear mixer. The parameters that affect the quality of the mixture are the rotor geometry, chamber loading, mixing temperature and the sequence of materials addition. After the mixing, a homogeneous feedstock is obtained that is free of agglomerates that would affect its flow [84].

Torque rheometry allows the study of multicomponent thermoplastic systems and their processing behaviour. Torque rheometry measures the torque caused by the resistance of the material to the shearing action and the thermal sensitivity of the feedstock. A typical measurement of the torque during mixing as a function of time is shown in *Figure 3.9*.

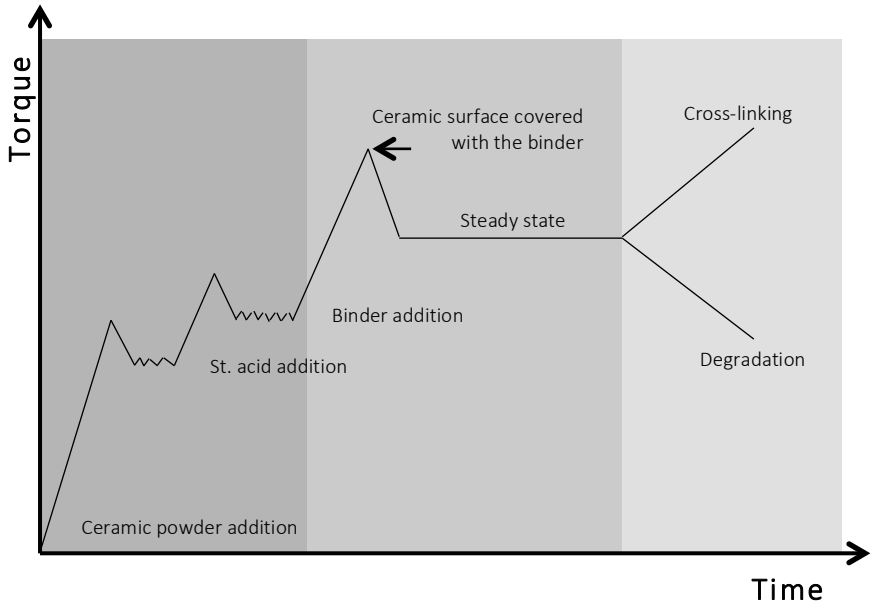

Figure 3.9: *Schematic representation of the measured torque as a function of time during compounding*

When the raw materials are introduced in the heated mixing chamber (*Figure 3.10*a), they cause additional resistance to the rotation force of the blades and therefore an increase of the torque is observed. This resistance is overcome when the thermoplastic binder melts and the ceramic surface is covered with the binder, therefore the torque decreases and reaches a steady state. A stable torque is an indication that the ceramic powder is uniformly distributed in the binder. During mixing an increase or decrease of the torque might occur, depending whether cross-linking or degradation of the binder take place [84].

The torque rheometer in EMPA is a HAAKE PolyLab Mixer, Rheomix 600, Thermo Scientific, Karlsruhe, Germany, shown in *Figure 3.10b*.

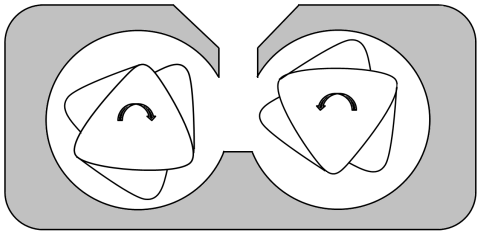

(a)

(b)

Figure 3.10: *(a) Schematic front view of the chamber, (b) HAAKE PolyLab Mixer Torque rheometer in EMPA*

3.2 Characterisation methods

Based on the aims and objectives set in the previous chapter a variety of characterisation methods are needed in order to determine the physical and electrical properties of the candidate ceramics for both wear sensor and flow battery. These methods are described in this section.

3.2.1 Physical properties and structural characterisation

Density and porosity measurements

It is important to determine the density of the ceramics, since a density above 95% of the theoretical value is needed in order to ensure that the electrical measurements are truly representative of the material and the influence of the porosity is a small. BS En623:2 [85] details the steps and the appropriate

precision in order to make acceptable measurements. The experimental set up is shown in Figure 3.11, which allows wet and dry weight measurements to be conducted.

Figure 3.11: *Density measurements set up*

The samples were cleaned in an ultrasonic cleaner with ethanol and then dried at 50°C overnight. Following the dry weight measurement (m_1) the samples were submerged in distilled water and left in a vacuum oven for 1.5h according to the BS En623:2 standard. Samples were then weighed when submerged in distilled water (m_2), the temperature of the water was recorded for every sample. Finally, the mass of the water impregnated ceramics was measured on a dry substrate after wiping away any excess water on the surface of the ceramic (m_3).

From this data the bulk density (p_b, g/cm^3, eq.4), the apparent solid density (p_s, g/cm^3, eq.5) and the apparent solid porosity (π_a, %, eq.6) were calculated.

$$\mathbf{p_b = \frac{m_1}{m_3 - m_2} \times p_l,} \qquad \textbf{Equation 4}$$

$$\mathbf{p_s = \frac{m_1}{m_1 - m_2} \times p_l,} \qquad \textbf{Equation 5}$$

$$\mathbf{\pi_a = \frac{m_3 - m_1}{m_3 - m_2} \times 100,} \qquad \textbf{Equation 6,}$$

where p_l is the density of the distilled water depending on the temperature of the water.

The bulk density (p_b) describes the overall density of the material including both open (interconnected) and closed porosity, whereas the apparent solid density (p_s) excludes the open porosity. Similarly the apparent porosity (π_a) provides a measure of the open pores. The percentage theoretical density is calculated from the ratio of the bulk to theoretical density to make the comparison easier. Density measurements are necessary since porosity can influence the electrical measurements and the pores act as defects in the material which can influence the mechanical strength and the wear/hardness of the material

Helium pycnometer

The helium pycnometer (*Figure 3.12*) is used to determine the actual density of a sample without including the volume occupied by internal or open porosity. This method is based on placing a sample of known mass into a cell of known volume. The sample is initially placed into a cell under vacuum. Helium is then introduced into the cell and occupies the entire volume of the cell that is not occupied by the sample. The volume of the sample can then be calculated since the volume of the cell is known, thus the actual density [86]. If the sample occupies less than 2/3 of the cell volume the measurements will be less accurate. The Helium pycnometer was used for the porous fibres, since their fine scale excluded the use of the Archimedes method.

Figure 3.12: *Helium pycnometer in EMPA(AccuPyc II, micromeritics)*

Dilatometry

The Thermal Expansion Coefficient (TEC), α, was measured using a high temperature (HT) dilatometer, model DIL 402C Netzsch, *Figure 3.13*, which allows measurement of the expansion of a specimen from room temperature (RT) up to 1400°C. All dilatometry measurements have been performed under a nitrogen flow, to avoid re-oxidation of the samples.

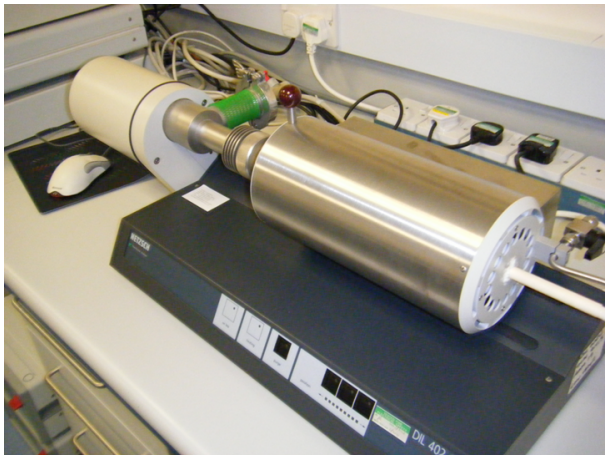

Figure 3.13: *High Temperature dilatometer, DIL 402C Netzsch*

Such horizontal dilatometers, as shown in *Figure 3.14*, comprise of a horizontal tube, the end of which is inserted into a furnace. A pushrod is fixed in a high sensitivity linear displacement transducer. The sample is placed against the end of the tube and is held in place by the pushrod. The samples used had a rectangular cross-section and 25mm length and were cut off a 30mm diameter tablet, pressed with uniaxial pressing. The thermocouple is placed as close to the sample as possible and calibration measurement was always taken before the actual measurement to ensure accurate results [87].

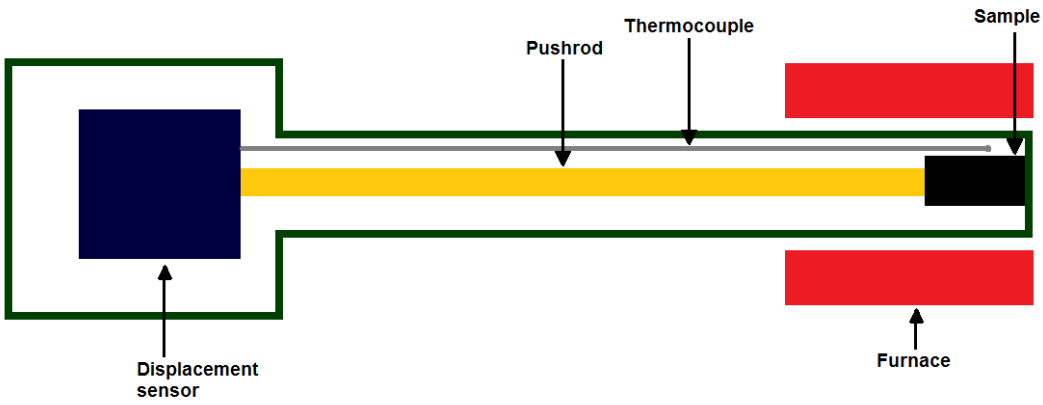

Figure 3.14: *Schematic representation of a horizontal dilatometer*

Wear measurements [88]

The wear resistance of the materials was determined using pin-on-disk testing, following the ASTM G99 [89] and BS EN 1071[90] standards. A pin-on-disk as shown in *Figure 3.15* is a common method of measuring wear. The pin, that was fabricated specifically for the dimensions of MAX phase and Magnéli phases tablets, was pressed against a rotating disc of the other material concerned at a fixed distance from the centre of rotation.

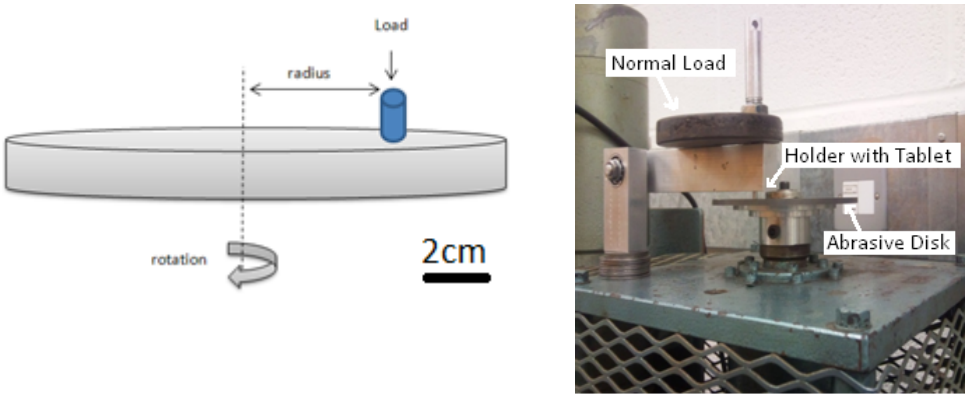

Figure 3.15: *Pin-on-disk representation –wear measuring method [88]*

The aluminium pin design and the dimensions are shown in *Figure 3.16*, the tablets were levelled using compliant adhesive wax in the inner circle.

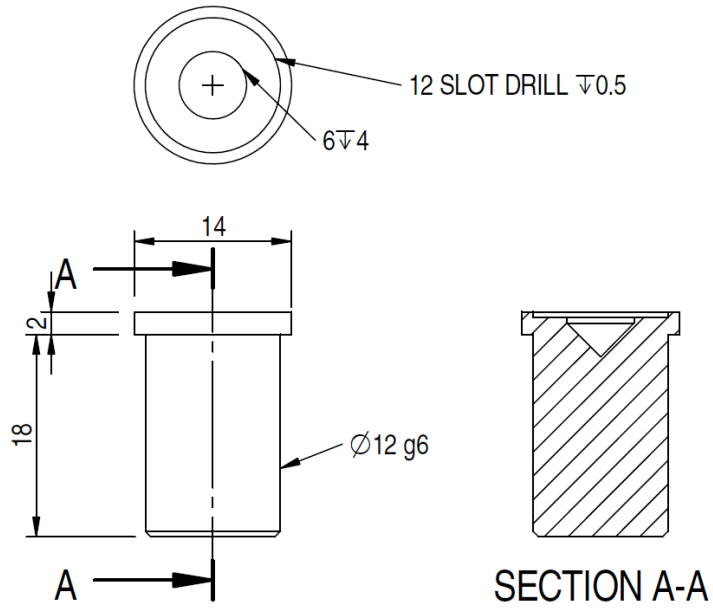

Figure 3.16: *Pin design for wear measurements [91]*

Hardness measurements

The hardness measurements were conducted using the LECO M-400 Micro hardness tester with a diamond indenter that can be seen in *Figure 3.17*.

Figure 3.17: *LECO M-400 Micro hardness tester*

The samples were mounted in resin and polished to provide a clean, flat surface to penetrate with the indenter. Individual resin blocks were loaded into the machine and the surface was penetrated by a diamond tip with a test load of 500gf. The diagonals of the diamond tip profile embedded on the surface ware measured and it was used to evaluate the Vickers hardness (HV). The diagonals

were determined using the optical microscope of the equipment. To ensure accuracy of the measurements, experience and calibration are very important. The Vickers hardness (HV) is defined as follows:

$$\mathbf{HV} = \frac{\mathbf{F}}{\mathbf{A}} = \frac{\mathbf{2Fsin}\left(\mathbf{\Theta}/\mathbf{2}\right)}{\mathbf{d^2}} = \mathbf{1854} \times \frac{\mathbf{F}}{\mathbf{d^2}}, \qquad \textbf{Equation 7,}$$

where F is the test load (gf), A is the surface area of indentation (μm^3), Θ is the angle between opposite faces of tip (136°) and d is the average diagonal length of indentation (μm).

XRD - X-ray diffraction

Powder X-Ray Diffraction (XRD) is a tool to understand the crystal structure of samples. For the Magnéli phases XRD was useful to determine which crystal phases constitute the Magnéli phases samples, since they are polycrystalline materials and the various processes followed reduce the samples in various proportions. In the case of MAX phase XRD was useful in order to determine the temperature in which the MAX phase (Ti_2AlC) can be obtained without the creation of second phase of TiC. The equipment used was a Philips PW1730 (Cu-Kα, λ=1.541838Å, 40kV, 25mA), *Figure 3.18*.

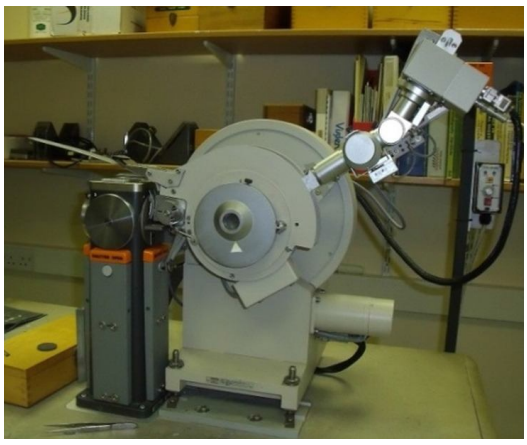

Figure 3.18: *Phillips PW1730 XRD analyser*

The samples were ground to a very fine powder using a mortar and pestle, washed with ethanol and left to dry at 50°C overnight.

SEM- Scanning Electron Microscope

The SEM helps the physical understanding of the materials and assessment of the microstructure of the material. With respect to the MAX phase and the Magnéli phases, the SEM was used to determine the grain size, the porosity and analyse the homogeneity of the samples. The SEM used in University of Bath was a JEOL JSM6480LV (*Figure 3.19*a) and in EMPA was a Tescan Vega TS 5236 MM.

(a) (b)

Figure 3.19: *(a) JEOL JSM6480LV in University of Bath and (b) Tescan Vega TS 5136 MM in EMPA*

The samples were mounted in resin blocks using Epothin that can withstand the high voltage and vacuum conditions without warping or charging and it is more suitable for porous materials. The grinding and the polishing steps followed are shown in Table 3.1. In an attempt to reveal more clearly the grain boundaries some of the samples were also thermally etched before the polishing for one hour at 800^{o}C. However such a temperature may cause re-oxidation in the case of Magnéli phases. In the case of Magnéli phases fibres SEM images were taken both with and without the polishing steps in Table 3.1.

Table 3.1: Grinding/polishing steps for SEM sample preparation

Stage	Surface	Lubricant	Particle size	Head rotation	Speed
Planar grinding	SiC paper	Water	P120	Complementary	150
Planar grinding	SiC paper	Water	P320	Complementary	150
Planar grinding	SiC paper	Water	P600	Complementary	150
Planar grinding	SiC paper	Water	P1200	Complementary	150
Planar grinding	SiC paper	Water	P4000	Complementary	150
Polishing	Chemomet cloth	Silica	0.05µm	Complementary	150

The SEM images were also used to determine the grain size of the materials. Depending on the resolution of the images the grain sizes were calculated either by adjusting the threshold using ImageJ free software or using the linear intercept method.

Energy Dispersive X-ray (EDX)

Energy dispersive X-ray spectroscopy (EDX) was used to determine the chemical structure of materials. It was carried out in the SEM (JEOL 6480) and provides an elemental analysis of the specimen.

Thermo gravimetric Analysis (TGA)

A Setaram TGA 92 16.18 (*Figure 3.20*) was used for the TGA measurements. The microbalance (*Figure 3.21*) used for the TGA measurements was sensitive (±0.1% accuracy [92]) and the operating weight range for samples was 12-50mg. The samples used were approximately 20mg.

***Figure 3.20**: Setaram TGA 92 16.18*

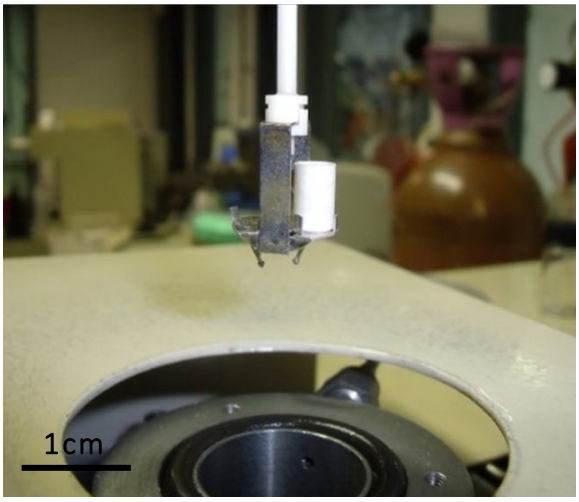

***Figure 3.21:** TGA crucible balance*

Both the samples and the crucible were cleaned with ethanol using the ultrasonic cleaner and then left to dry overnight with the crucible at 50°C. During the experiment the cooling water flow rate was set at 1.4l/min, the argon shield gas inlet pressure was set at approximately 0.5bar and the carrier gas (air) inlet pressure was set at approximately 1.5bar. There was an initial ramp up to 100°C to remove any humidity in the samples and data was only recorded after that initial ramp from room temperature up to 900°C. To increase the accuracy a blank run with the crucible and no sample was conducted.

3.2.2 Electrical characterisation

Impedance Spectroscopy

Impedance Spectroscopy (IS) is a powerful technique for the measurement of impedance and more generally the electrical properties of a material over a frequency range [93]. A typical IS experiment, of the type undertaken at University of Bath to characterise ceramics under study, is done by applying a small voltage perturbation ($0.1V_{rms}$) to the specimen, then measuring its response (current) over a broad range of frequencies (1MHz to 0.1Hz) using the set up shown in *Figure 3.22*. A furnace allows the control of the temperature of the specimen up to 1000°C. Different types of electrodes can be applied to the ceramic in order to provide a good contact for IS measurements [94, 95].

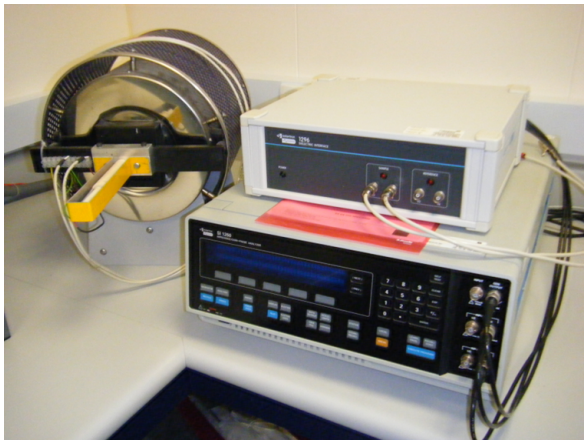

Figure 3.22: *Solartron 1260 Impedance Analyser with a Solartron 1296 dielectric interface, coupled with a furnace*

Impedance Spectroscopy (IS) allows measurements of the conductivity and resistivity of ceramic materials. It is assumed that at low frequencies (0.1-1Hz) the values obtained correspond to the dc conductivity and resistivity of the material [96].

Impedance Z (ohms) is a complex variable:

$$Z = Z' + iZ'', \quad \textbf{Equation 8,}$$

where Z' is the real component of the impedance (purely resistive) and Z'' is the imaginary part (reactance). It is then possible to define the admittance (Y), which is the reciprocal of impedance:

$$Y = \frac{1}{Z' + iZ''}, \quad \textbf{Equation 9.}$$

Admittance Y is also a complex variable composed of a real part, the conductance (*G)*, and an imaginary part, the susceptance (*B*):

$$Y = \frac{1}{Z' + iZ''} \cdot \frac{Z' - iZ''}{Z' - iZ''} = \left(\frac{Z'}{Z'^2 + Z''^2} \right) + i\left(\frac{-Z''}{Z'^2 + Z''^2} \right) = G + iB \textbf{, Equation 10.}$$

Therefore the real conductance (*G*) is given by:

$$G = \frac{Z'}{Z'^2 + Z''^2} \textbf{, Equation 11,}$$

and from the conductance, it is possible to calculate the ac conductivity, σ^* (S/m):

$$\sigma^* = G \cdot \frac{t}{A} \textbf{, Equation 12,}$$

where t is material thickness/length (m), and A is the area of material (m^2). As discussed above, at a lower frequency (and providing polarisation effects are not present), the ac conductivity provides a good approximation of the dc conductivity (σ). A similar discussion can be made for the ac resistivity (ρ^*) and dc resistivity (ρ) that are simply given by the reciprocal of the conductivity.

The ability of the dielectric materials to store electrostatic charge is expressed by the permittivity (ε) of the material. Assuming a parallel plate capacitor filled

with a material of permittivity ε. The permittivity is related to the capacitance (C), by the following equation:

$$C = \frac{\varepsilon \cdot a}{d}, \qquad \textbf{Equation 1,}$$

where α is the area of each of the plates (m^2) and d is the distance separating the plates. The permittivity of a dielectric is also related to the permittivity of vacuum (ε_0), 8.85x 10^{-12} F/m:

$$\varepsilon = \varepsilon_r \cdot \varepsilon_0, \qquad \textbf{Equation 2,}$$

where ε is the relative permittivity or dielectric constant of the material, which is also effectively a measurement of the ability of a material to store charge. Combining eq.13 and 14 the relative permittivity is given by:

$$\varepsilon_r = \frac{C \cdot d}{a \cdot \varepsilon_0}, \qquad \textbf{Equation 3}$$

It is then possible to calculate its ac permittivity (ε_r) from Impedance Spectroscopy since capacitance (C) is given by:

$$C = -\frac{Z''}{(Z'^2 + Z''^2) \cdot \omega}, \qquad \textbf{Equation 4}$$

where Z' is the real part of the impedance (purely resistive), Z'' is the imaginary part of the impedance (capacitive) and ω is the angular frequency $(2\pi \cdot f)$.

In order to prepare the bulk samples for IS measurement the surface was polished with a SiC paper (P600) to remove any surface defects and the samples were cleaned in an ultrasonic bath with ethanol and then dried overnight.

Table 3.2 shows the drying and firing conditions needed for the various electrode used.

Table 3.2: Drying and firing conditions for the electrodes tested

Electrode	Details	Drying	Firing
Silver paint	Electrolube - SCP03B	120°C for 10min	-
Silver paste	Gwent, C2060217D3	120°C for 10min	660°C for 10min
Platinum paste	Gwent, SB010401	120°C for 10min	600 or 800°C for 10min
Aluminium paste	Gwent, C2100303D2	120°C for 10min	710°C for 10min

In order to conduct the IS measurements for the fine scale fibres (typically with a diameter of 260μm) it was necessary to attach wires. Various electrodes and wires were initially examined first to check the linearity of the measurements to ensure ohmic contacts. The wires were attached at the sides of the fibres and the length of the fibres was 5mm (size of the sensing element of the sensor). It was not possible to control the point of contact, which causes some instability to the measurements; poor fibre-wire contact (*Figure 3.23*). The ideal bond would be to have a fully covered fibre side with electrode and the contact point of the fibre to be close to the bottom of the side, so that when material is being removed from the upper surface the bond is not damaged.

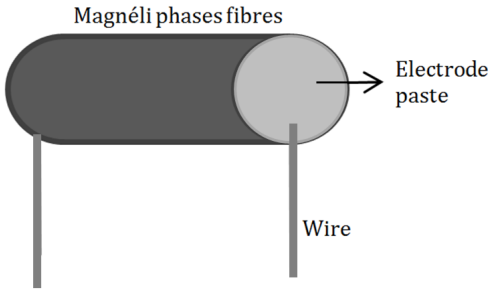

(a)- ideal contact

(b)- incomplete coverage *(c)- incomplete coverage and poor contact*

Figure 3.23: *(a) Ideal and (b, c) faulty fibre-wire bonds*

The IS measurements were analysed using Zview software (Version No 1631 Scribner Associates). Various methods to analyse the electrical data have been employed ranging from simple equivalent circuits to resistor-capacitor networks [93, 97].

An example of an equivalent circuit that is often used for ceramics is shown in *Figure 3.24*. This basic equivalent circuit consists of two parallel resistor – capacitor (RC) elements connected in series. One RC element relates to the grain boundaries and the other to the grain (bulk).

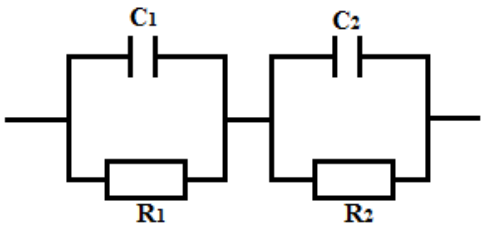

Figure 3.24: *RC equivalent circuit*

Data collected with IS in a wide range of frequencies and temperatures can also be used to calculate the activation energy (E_a) for conduction using the Arrenhius' equation:

$$\ln(\sigma_{DC}T) = A - \frac{E_a}{k_B T}, \quad \textbf{Equation 17}$$

where A is a constant, σ_{DC} is the DC conductivity (S/m) measured at 0.1 Hz, T the absolute temperature (K), and κ_B is the Boltzmann constant (eV/K). By plotting

$\ln(\sigma_{DC}T)$ versus 1/T, the activation energy can be determined from the slope of the graph.

Linearity measurements

Since the wear sensor relies on the accurate measurement of the resistance of the ceramic fibre, it is critical for the performance and reliability of the device to acquire a low resistance, stable metal-ceramic ohmic contact. An ohmic contact between two conductors has a linear current-voltage (I-V) curve consistent with the Ohm's law. Generally, ceramics that are insulators or semiconductors, create Schottky barriers in contact with metals, due to the energy difference between the Fermi Level of the metal and the energy bands of the ceramic (*Figure 3.25*) [98-105].

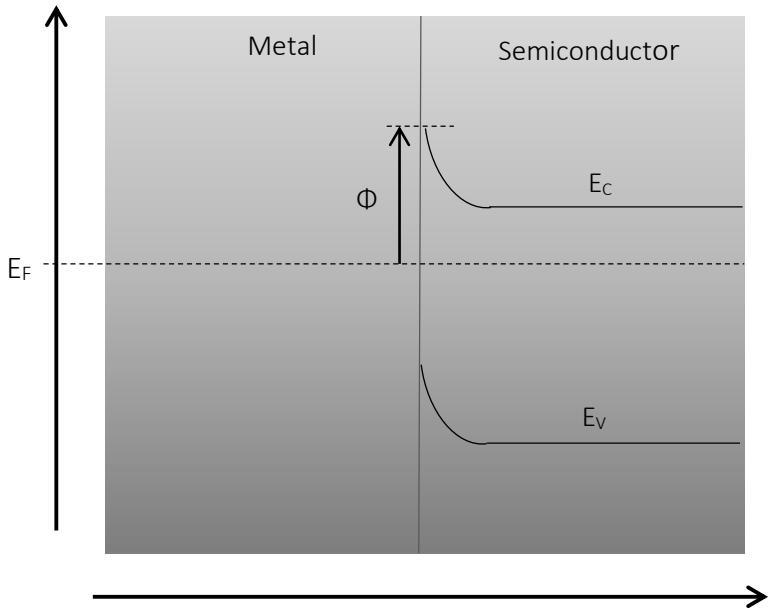

Figure 3.25: *Band diagram for Shottky barrier metal-semiconductor bond*

An ohmic contact is possible between metals and semiconductors by choosing the appropriate metal, carefully applying a thin layer and annealing it to alter the metal- semiconductor bond. Regarding the Magnéli phases that have close to metallic conductivity, various electrodes were tested and the I-V curves were acquired using Agilent E5270B.

3.2.3 Cyclic voltammetry

To test Magnéli phases as RFB electrodes, electrochemical characterisation was undertaken at the University of Southampton. For the electrochemical characterisation, the cell shown in *Figure 3.26* was designed and constructed. The Magnéli phases fibre was used as a working electrode and a Pt wire was used as both the counter and the reference electrode. All the electrodes were placed together in the small cavity of the electrochemical cell and two electrolytes were tested; H_2SO_4 and KOH.

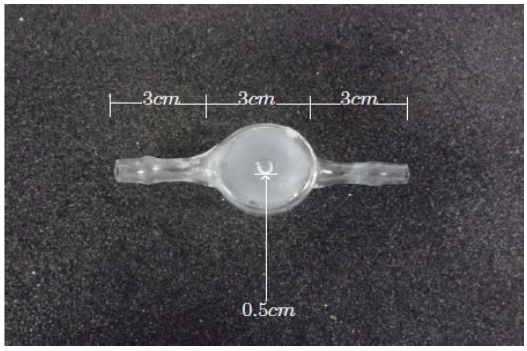

***Figure 3.26**: The electrochemical cell used for the characterisation of the Magnéli phases [106]*

The above cell provided the opportunity for initial tests and the observation of redox activity. However, the arrangement of the cell and the fragility of the fibres made the conditions of the measurements rather complicated. One series of some initial cyclic voltammetries on the Magnéli fibres in H_2SO_4 and in KOH is shown in *Figure 3.27*. Redox peaks are observed which justifies the use of Magnéli phases as electrodes. Four scans took place to examine the stability of the electrodes in the two electrolytes. The data show no significant change after four scans, although the set up does not allow their full evaluation.

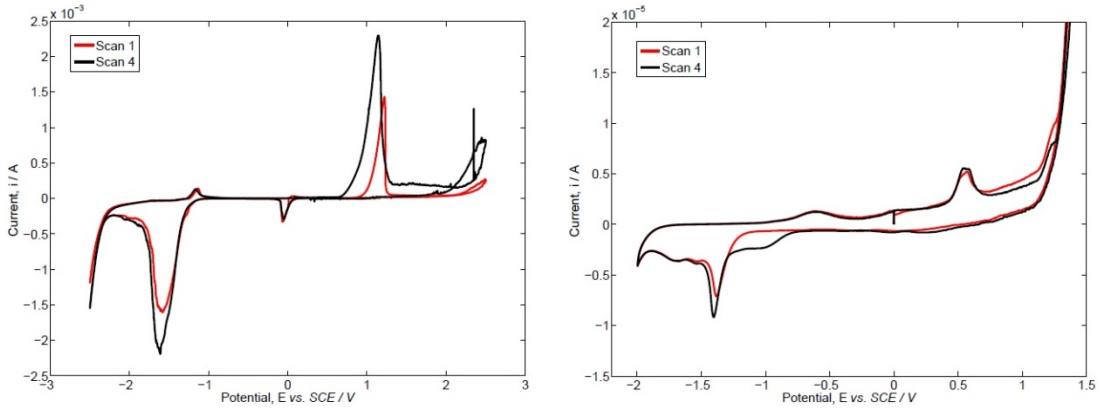

(a) (b)

Figure 3.27: *Cyclic voltammograms in (a) 1.0 M H_2SO_4 and (b) 4.0 M KOH of Magneli fibres. The first scan (red line and the fourth scan (black line) are shown. The scan rate of the voltammograms was 50 mV sec^{-1} and the temperature was 293K [106]*

The electrochemical cell that was used during the cyclic voltammetry for more detailed and accurate measurement of the Magnéli electrodes was a three-compartment cell as shown in *Figure 3.28*. A Pt mesh (1.5 cm^2) was used as the counter electrode and a saturated calomel electrode (SCE) was used as the reference electrode. The working electrode was the Magnéli microelectrode. Additionally, a standard glassy carbon electrode (GCE) was used as a working electrode to have a reference point. The working electrode was placed in the main compartment of the cell close to the end of the Luggin capillary which was connecting the part of the cell where the reference electrode was placed. The electrolyte used was an aqueous solution of potassium ferricyanide (5.0 mM $K_3Fe(CN)_6$) in potassium nitrate (0.1 M KNO_3).

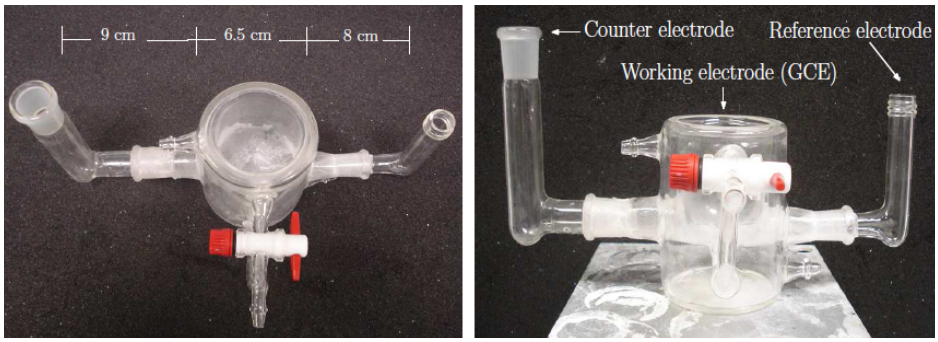

Figure 3.28: *Three- electrode electrochemical cell used for the electrochemical characterisation of the Magnéli microelectrodes [106]*

4. Dense bulk ceramics - Development and characterisation

The current chapter describes the process followed to develop the bulk ceramic materials under study. In order to make the initial characterisation and determine the basic properties to finalize the materials selection, bulk samples were prepared. Section 4.1.1 and 4.1.2 describe the development processes for MAX phase (Ti_2AlC) and Magnéli phases (Ti_nO_{2n-1}) respectively. Following the manufacturing processes, section 4.2 presents the structural and physical characterisation of the bulk samples and section 4.3 reports the electrical properties.

4.1 Development of bulk ceramics

Before focusing on the manufacturing of the conductive dense fibres that will be used for the wear sensor, the final material selection was based on characterising the properties of bulk samples made from both MAX phase ceramics and Magnéli phases. The manufacturing parameters of the dense tablets were optimised in order to tune the properties.

4.1.1 Development of MAX phases bulk samples

Figure 4.1 shows typical MAX phase samples prepared for electrical and thermal expansion characterisation.

Figure 4.1: *MAX phase (Ti_2AlC) ceramics prepared for electrical and thermal testing [12]*

The initial characterisation of the MAX phases (Ti_2AlC), described in section 2.2.1, was performed using MAX phase powder and bulk samples supplied by Kanthal (MAxthal 211, grain size 100μm) [107]. A commonly used method to manufacture dense MAX phase materials is hot isostatic pressing (HIP) [108]. Though pressureless sintering is less expensive, it is not easy to achieve highly dense samples from starting materials. Therefore, MAX phase powder was used in pressureless sintering. The powder was cold pressed uni-axially into tablets using a 13 mm diameter die with a force of 443 MPa for 0.9 g of powder. The 'green' state tablets were sintered in an alumina tubular furnace at 1400°C under an argon flow for 3h [91].

The aim regarding the MAX phase, as it was set out in section 2.3, was to decrease the electrical conductivity and increase the hardness and wear

resistance. In order to achieve that, MAX phase samples were prepared containing 5%, 10% and 20% of alumina [109] (99.5% alumina, D_{50}=max 6 microns). The powders were mixed and ball milled for 24h with zirconia pearls (ø1cm) before they were pressed using a 10mm die by dry cold uniaxial pressing, applying a pressure of ~400MPa (~40kN over an area of 1cm^2). The firing temperature was again 1400^{o}C, with a 150^{o}C/h heating and cooling rate, for 3h under constant Argon flow.

4.1.2 Development of Magnéli phases bulk samples

In order to manufacture Magnéli phases ceramics, TiO_2 powder (Pi_kem, 99.5%, 0.3μm) was initially processed by adding 2.5% wt of an organic binder, (polyethylene glycol-PEG 8000). A slurry was then created with the addition of distilled water (1ml per 1g of powder) and ball milled for 24h with zirconia pearls (ø1cm) using the apparatus (Figure 3.2) [110, 111]. Ball milling, further reduces the particle size and thoroughly mixes the organic binder with the ceramic powder preventing the formation of agglomerates. The slurry was then dried and the resulting powder sieved through a 45μm mesh [79]. TiO_2 tablets were formed by dry cold pressing, applying a pressure of ~250MPa (~20kN over an area of 1cm^2). The resulting green body was then fired in a furnace in air up to 1300^{o}C with an initial step at 400^{o}C for two hours to burn out the binder. *Figure 4.2* shows the firing regimes that were followed [112]. Typical TiO_2 tablets are shown in *Figure 4.3* and at this stage the material is stoichiometric and non-electrically conductive.

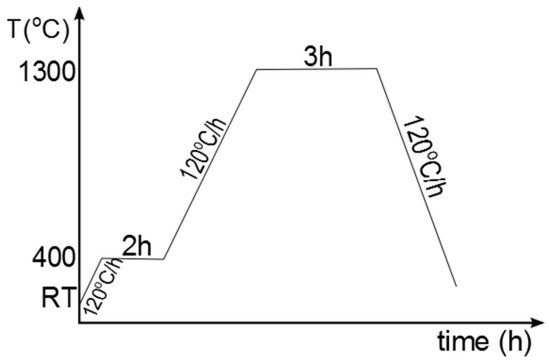

(a)

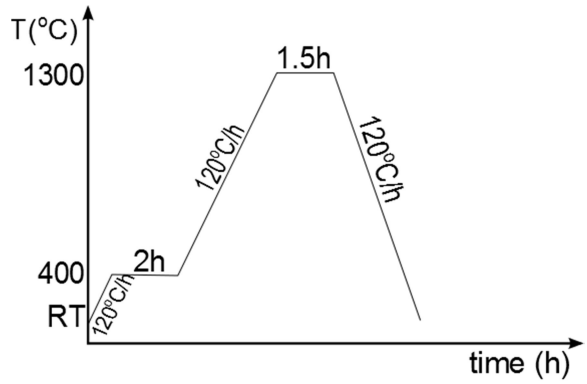

(b)

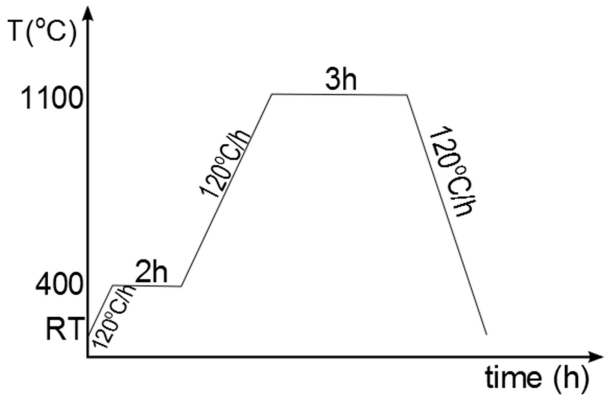

(c)

Figure 4.2: *Sintering conditions for TiO_2 in air*

Figure 4.3: *TiO_2 samples used to determine the electrical and the thermal properties [12]*

In order to obtain the Magnéli phases tablets, sintered tablets were reduced through a carbo-thermal process performed in a tubular furnace at 1300°C under an argon flow using a heating/cooling rate of 150°C/h. The typical dwelling time was 6 h [56], however samples reduced for 1, 2, 4, 6, 8 hours were prepared in order to examine if this resulted in changes to the grain size and electrical conductivity, since each Magnéli phase has a different conductivity [37]. After the reduction, the characteristic colour of the tablets is black (*Figure*

4.4). Due to the reduction, a variety of Ti - sub-oxides are created that have different energy gaps. That means that the energy gap between the top of the valence band and the bottom of the conduction band varies from 0.006 to 3.04 eV [56].

Figure 4.4: *Magnéli phases samples, compared with TiO_2 samples before reduction (Figure 4.3) [12]*

4.2 Physical properties and structural characterisation

In order to determine the physical properties and structure of the materials under study, the characterisation methods (XRD, SEM, density measurements, wear measurements, Impedance Spectroscopy) described in section 3.2 were used. These results are presented in the current chapter for the MAX phase (Ti_2AlC) and the Magnéli phases (Ti_nO_{2n-1}) bulk samples.

4.2.1 Physical properties and structural characterisation of MAX phase (Ti_2AlC)

After producing the green tablets as described in section 4.1.1 and firing them, XRD was conducted to confirm the phases created during firing. *Figure 4.5a* shows the XRD spectra of the MAX phase powder as received from Kanthal and the spectra of the first firing attempt at 1300^{o}C under constant argon flow. As it is observed after the firing at 1300^{o}C, alumina and TiC are still present in the samples. The second firing attempt was at 1400^{o}C under constant argon flow and as it is observed from the XRD spectra in *Figure 4.5b* there is only MAX phase present.

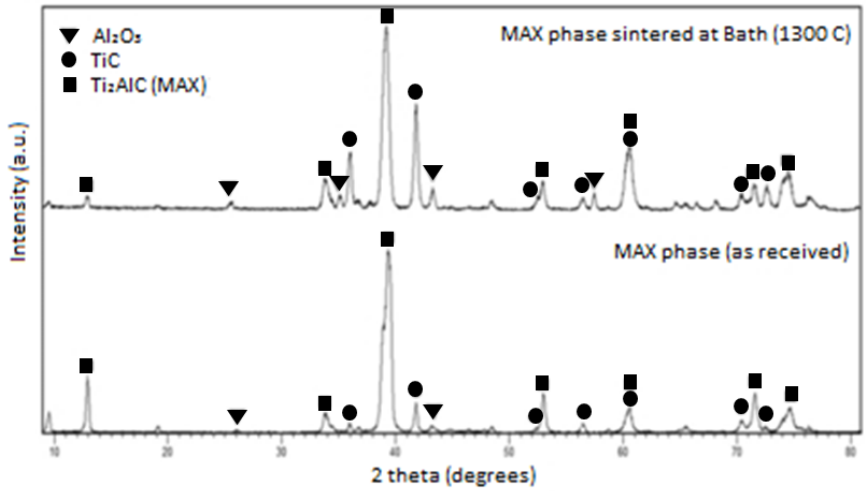

(a)

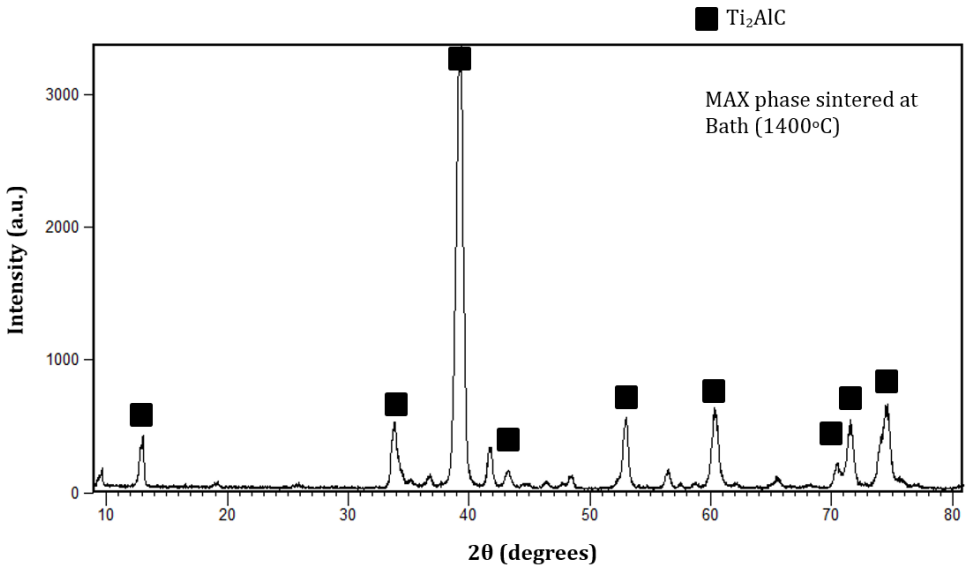

(b)

Figure 4.5: *XRD spectra of (a) MAX phase powder as received from Kanthal and MAX phase tablets fired at 1300°C and (b) MAX phase tablets fired at 1400°C [91]*

The theoretical density of MAX phase Ti_2AlC is 4.11 g.cm^3 [27] and the measured density of the samples was 3.35 g.cm^3 (82% of the theoretical). The low density of the samples agrees with that reported in other work as well [113]. Alumina was used to manufacture a ceramic alloy in order to increase the density [113]. The wear resistance of the samples fired at 1400°C was

determined using the pin-on-disk wear test (3.2.1) and was compared with the wear resistance of steel. For the steel sample it was possible to take four readings until the sliding distance reached the 350 km. However the wear rate of MAX phase was much higher than steel (*Figure 4.6*), so it was possible to make a single measurement at 106 km sliding distance. Table 4.1Error! Reference source not found. presents and compares the results, which show that the wear rate of the MAX phase is much higher than steel.

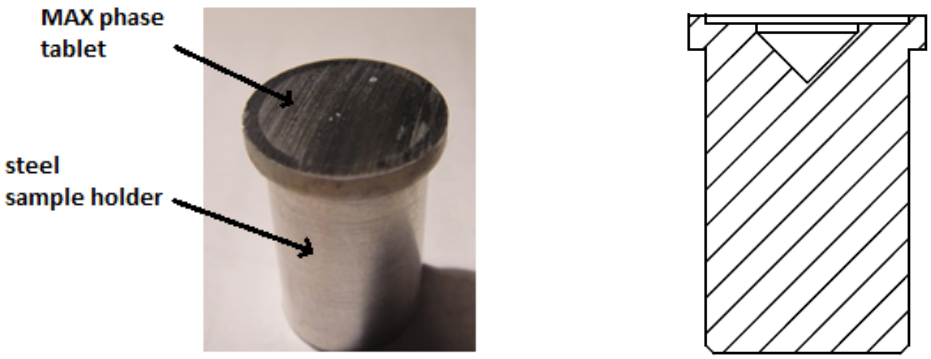

(a) *(b)*

Figure 4.6: *(a) MAX phase sample completely worn down after pin-on-disk wear measurement, (b) sample holder design*

Table 4.1: Steel and MAX phase wear measurements results

Material	Average wear rate ($mm^3/N.m$)
Hardened steel	$1.39x10^{-5}$
MAX phase (Ti_2AlC)	$9.46x10^{-7}$

In order to increase the density [109] and the wear resistance, MAX phase samples containing 5, 10 & 20 wt % alumina were manufactured. The strengthening is contributed to grain boundary strengthening and crack deflection [114]. *Figure 4.7* shows an EDX analysis of samples containing 10% alumina which shows that the alumina is homogeneously dispersed across the tablets and Table 4.2 presents the density measurements.

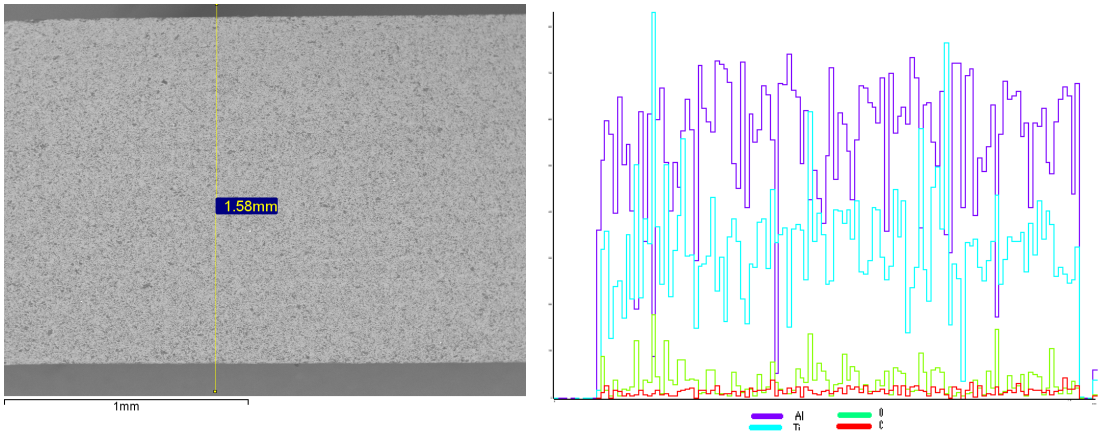

Figure 4.7: *EDX analysis across the samples cross section to detect the dispersion of αlumina*

Table 4.2: Density and porosity measurements of MAX phase with various proportions of alumina

Percentage of αlumina (%)	Theoretical density (g/cm³)	Bulk density (g/cm³)	% Apparent solid porosity	% theoretical density
0	4.10	3.35 ± 0.01	13.1 ± 0.53	82 ± 0.26
5	4.09	3.37 ± 0.04	23.5 ± 1.38	82.39 ± 0.99
10	4.08	3.51 ± 0.06	27.6 ± 2.24	85.92 ± 1.45
20	4.07	3.21 ± 0.29	20.4 ± 1.08	78.87 ± 0.72

As shown in Table 4.2 the density achieved with this method is not satisfactory (<90%), so other methods of development should be investigated, such as hot isostatic pressing (HIP).

4.2.2 Physical properties and structural characterisation of TiO_2 and Magnéli phases (Ti_nO_{2n-1})

After developing the green tablets as described in section 4.1.2 and sintering them as shown in *Figure 4.2*, the XRD in *Figure 4.8* confirms the presence of only rutile TiO_2 phase. Their density was then measured and the results are shown in Table 4.3.

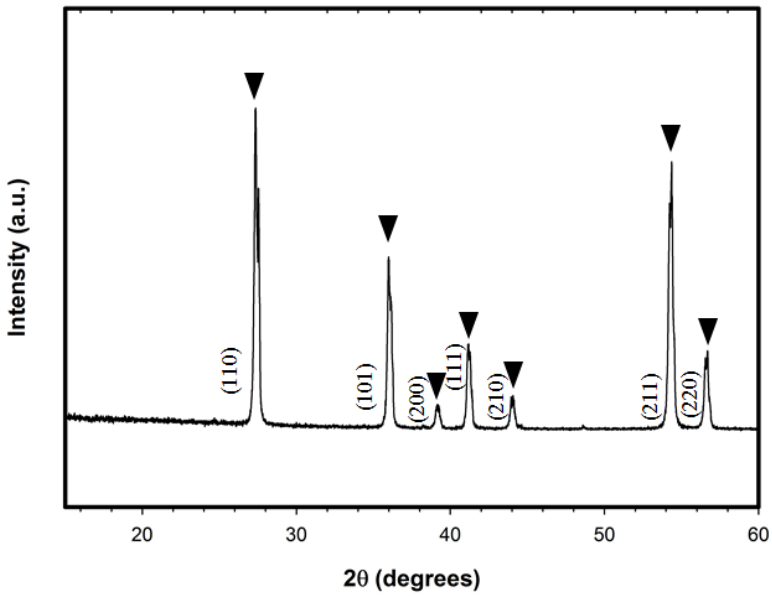

Figure 4.8: *XRD spectra of sintered TiO_2*

Table 4.3: Density and grain size measurements of the sintered TiO_2 tablets

Sintering process	Theoretical density ($g.cm^3$)	Bulk density ($g.cm^3$)	% Apparent Solid Porosity	% theoretical density	Grain size (μm)
1100°C/3h	4.3	3.95 ± 0.13	2.29 ± 1.05	93.51 ± 3.07	2-4μm
1300°C/1.5h	4.3	4.17 ± 0.20	0.24 ± 0.05	98.65 ± 0.48	5-10μm
1300°C/3h	4.3	4.15 ± 0.02	0.38 ± 0.05	98.21 ± 0.68	12-15μm

The results indicate that a sintering temperature of 1100°C is insufficient in order to achieve a dense ceramic (>95% of the theoretical density). On the other hand at 1300°C a sintering time for 1.5 h is sufficient to achieve a high density. *Figure 4.9* shows images with an optical microscope and the SEM from which the grain growth during the sintering process is obvious. The grain size is 5-10 μm.

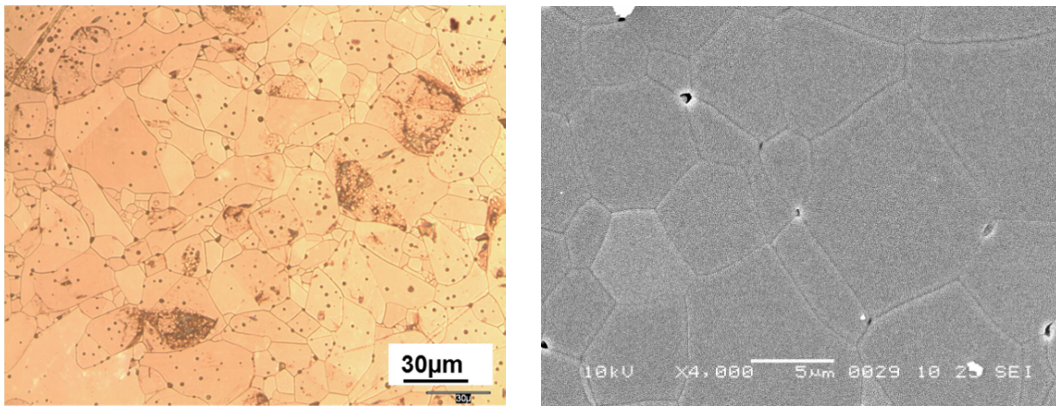

(a) *(b)*

Figure 4.9: *(a) Optical microscope image [12] (b) SEM image of TiO_2 sintered at 1300°C for 1.5h*

The hardness was also measured and the results are presented in Table 4.4, based on three measurements on each tablet.

Table 4.4: Micro-hardness measurements for TiO_2 tablets

Sintering process of TiO_2 tablets	**Hardness Mean MHV**
1100°C for 3h	764.0
1300°C for 1.5h	744.5
1300°C for 3h	835.2

The hardness fulfils the initial requirements (Table 2.1) of 700-800 MHV, since the hardness of hardened steel is 780 MHV. The sintering process selected for manufacturing the Magnéli phases was at 1300°C for 1.5h to avoid any unnecessary grain growth due to longer heating treatment.

The tablets were later reduced at 1300°C for 6h to convert the TiO_2 to Magnéli phase and increase the electrical conductivity. The density was measured once again to ensure that it was over 95% of the theoretical value in order to proceed to the electrical measurements. The density measurements are presented in Table 4.5 and show a density of 97% of the theoretical.

Table 4.5: Density and grain size measurements of the Magnéli phases tablets

Reduction process	Theoretical density (g.cm^3)	Bulk density (g.cm^3)	% Apparent Solid Porosity	% theoretical density	Grain size (µm)
1300^{o}C/6h	4.3	4.17 ± 0.02	0.59 ± 0.10	97.1 ± 0.54	70-100µm

Figure 4.10 shows the SEM images of the reduced samples that indicate the significant grain growth during the reduction. In order to achieve clear SEM images some of the samples were thermally etched at 800^{o}C for 45 min (*Figure 4.10a)*, whereas in *Figure 4.10b* the samples were not subjected to the heat treatment.

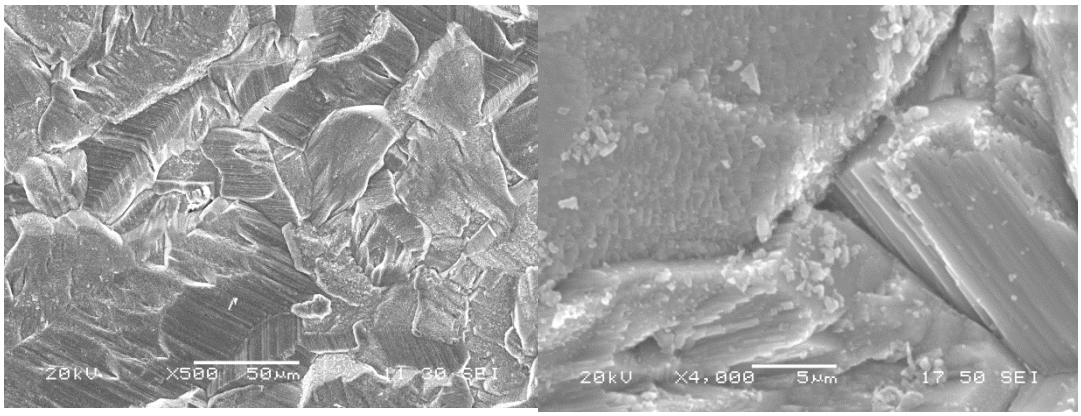

(a)

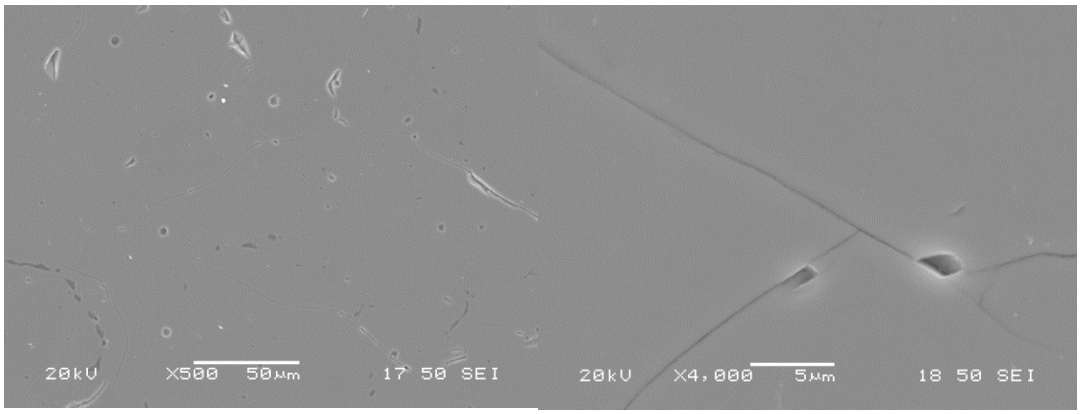

(b)

Figure 4.10: *SEM images of Magnéli phases tablets reduced at 1300^{o}C for 6h*

The grain size is approximately 70-100 µm. From the SEM images it is also indicated that the thermal etching has an effect on the surface that possibly changes the structure. The final size of the sensor, as proposed in section 2.1.1,

is approximately 300 μm, therefore a grain size of 100 μm may affect the stability and reliability of the sensor element since it would be only 2-3 grains wide.

The hardness of the Magnéli phases tablets was measured to be 917 MHV, which is higher than steel and higher than the initial stoichiometric TiO_2 material, since the defects make dislocation movement more difficult [115]. During the reduction defects and shear planes are created that act as boundaries and make dislocation slip more difficult [116]. This is in agreement with the wear measurements, shown in *Figure 4.11,* indicating that the wear rate of steel is higher in relation to the Magnéli phases.

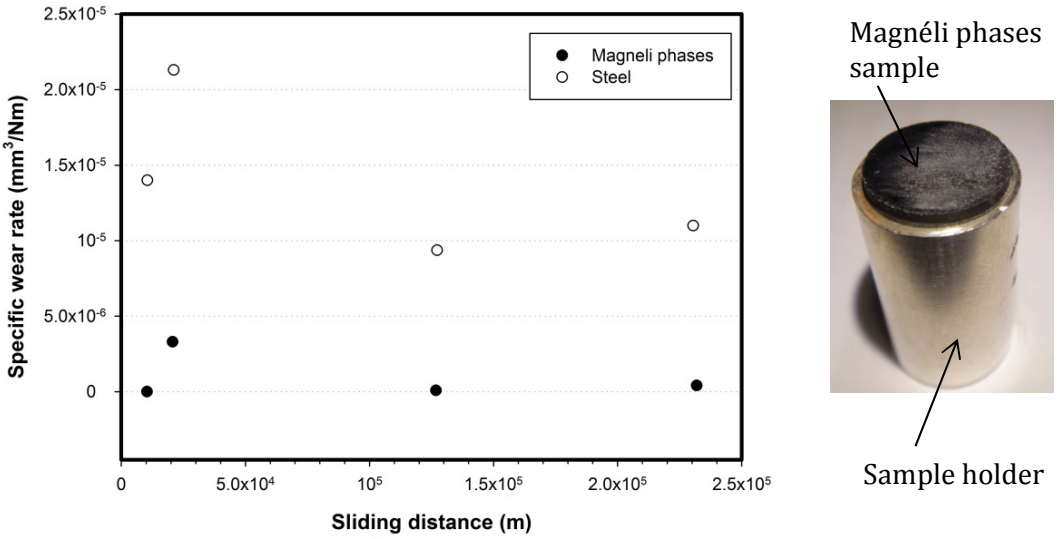

Figure 4.11: *Wear measurements of Magnéli phases and steel*

The wear measurement results for Magnéli phases and MAX phase are summarised in Table 4.6 so it is possible to compare them more easily with steel.

Table 4.6: Wear measurements of the Magnéli phases, the MAX phase and steel

Material	Average wear rate ($mm^3/N.m$)
Hardened steel	$1.39x10^{-5}$
Magnéli phases	$9.46x10^{-7}$
MAX phase	$7.19x10^{-4}$
Magnéli phases> Steel > Ti_2AlC (MAX phase)	

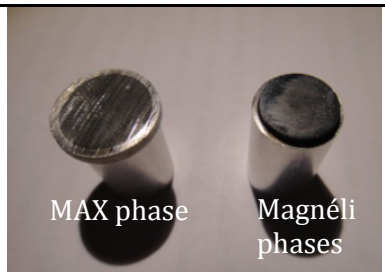

In order to control the grain growth some TiO_2 tablets were reduced at 1300°C for 1h and 4h. Table 4.7 summarises the density measurements and *Figure 4.12* shows an SEM image of a Magnéli phases sample reduced at 1300°C for 4h that indicates that the grains are slightly smaller (~70 μm) in comparison to the samples reduced for 6h.

Table 4.7: Density measurements of Magnéli phases tablets reduced at 1300°C for 1, 4 and 6h

Reduction process	Theoretical density ($g.cm^3$)	Bulk density ($g.cm^3$)	% Apparent Solid Porosity	% theoretical density	Grain size (μm)
1300°C/1h	4.3	4.16 ± 0.07	3.04 ± 0.62	96.65 ± 1.65	50-60
1300°C/4h	4.3	4.13 ± 0.04	1.39 ± 0.82	96.13 ± 0.98	60-70
1300°C/6h	4.3	4.17±0.02	0.59±0.10	97.10±0.59	70-100

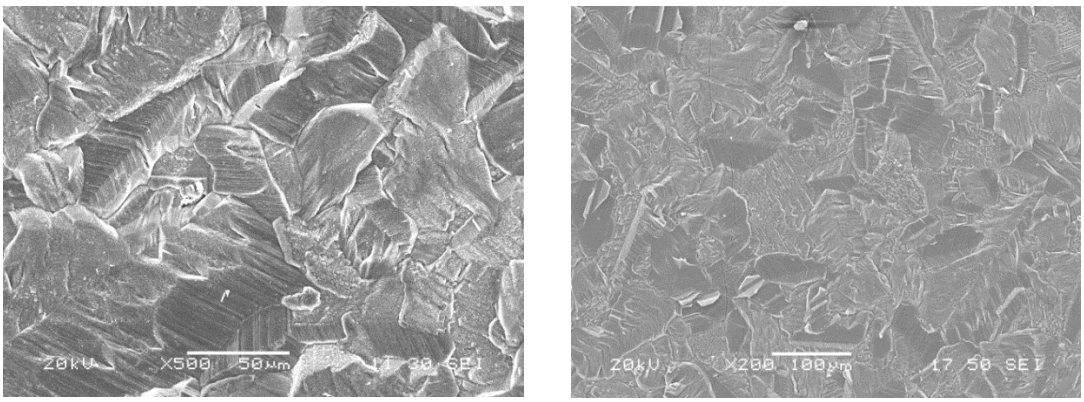

(a) *(b)*

Figure 4.12: *SEM images of thermally etched Magnéli phases tablets reduced at 1300°C for (a) 1h and (b) 4h*

Finally, X-ray diffraction was performed on samples that were reduced at 1300°C for 1, 2, 4, 6 and 8h, in order to determine if there are any structural differences due to the carbo-thermal reduction duration (*Figure 4.13*).

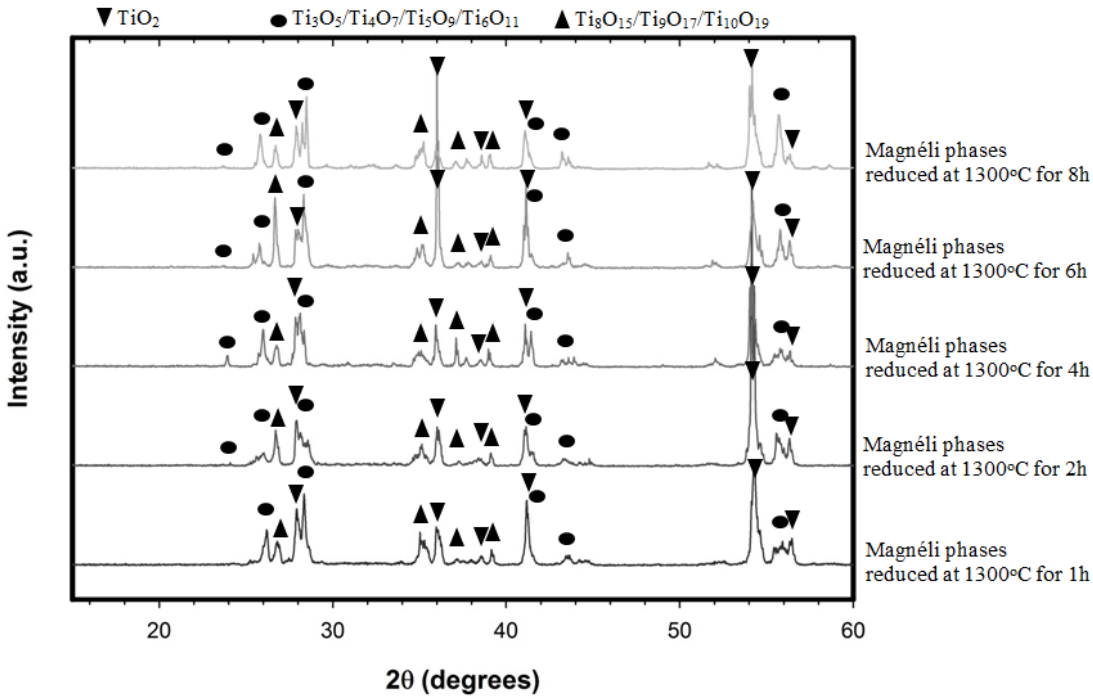

Figure 4.13: *XRD spectra of Magnéli phases reduced for 1, 2, 4, 6 and 8h (see also Figure 4.8 for TiO_2 XRD)*

The same phases are observed in all the spectra, which means that it is possible to achieve the reduction of the TiO_2 samples at 1300°C for even 1h. Since the samples are exposed to high temperature for less time, the grain growth is not as extensive, therefore the shorter reduction duration of 1h will be used.

4.3 Electrical characterisation

The electrical properties were the key properties for choosing the materials and attempting to tune them in order to meet the requirements of the applications. Regarding the MAX phase (Ti_2AlC), since the conductivity is close to copper (10^2-10^4 μΩ.cm), the work focused on trying to decrease it by creating the composite of MAX phase and alumina as described in section 4.1.1. In order to

predict and understand the frequency dependent response, the conductivity was modelled using electrical network models. Impedance Spectroscopy was the main tool used to experimentally characterize and understand the response of Magnéli phases. The results of the characterization study will be presented in the two following sections.

4.3.1 Electrical characterisation of composite MAX phase (Ti_2AlC) with alumina

Impedance Spectroscopy measurements on MAX phase are limited by the high conductivity of the material. However, in order to predict and understand the frequency dependent electrical properties of the compound developed (MAX phase with alumina) microstructural electrical network models were used [93]. The frequency dependent response of the compound materials can be modelled as a large network of conductive (R) and capacitive (C) regions and the measurable bulk conductivity and relative permittivity can be predicted by the logarithmic mixing rule as follows [117]:

$$\sigma_{system} = \sigma_{DC} + (\varepsilon_{ins}\varepsilon_0)^n(\sigma_{cond})^{1-n}\cos(n\pi/2)\,\omega^n, \textbf{ Equation 18}$$

$$\varepsilon_{system} = \varepsilon_{ins}n + (\varepsilon_{ins}\varepsilon_0)^n(\sigma_{cond})^{1-n}\sin(n\pi/2)\,\omega^{n-1}, \textbf{ Equation 19,}$$

where σ and ε are the conductivity and relative permittivity of the conducting (MAX phase) and dielectric/insulating phase (alumina), ε_0 is the permittivity of free space and n is the fractional volume of the material occupied by the dielectric phase. Table 4.8 shows the values used in the model.

Table 4.8: Conductivity and permittivity values used in the model

$\boldsymbol{\varepsilon_{ins}}$	9.1 [118]
$\boldsymbol{\sigma_{DC}}$	10^6 S/m [35]
n	0, 0.05, 0.1, 0.2, 0.3, 0.4

Using this model the conductivity and the permittivity of MAX phase mixed with alumina in different percentages was calculated. *Figure 4.14* and *Figure 4.15*

show the system ac conductivity and the system permittivity respectively as a function of frequency.

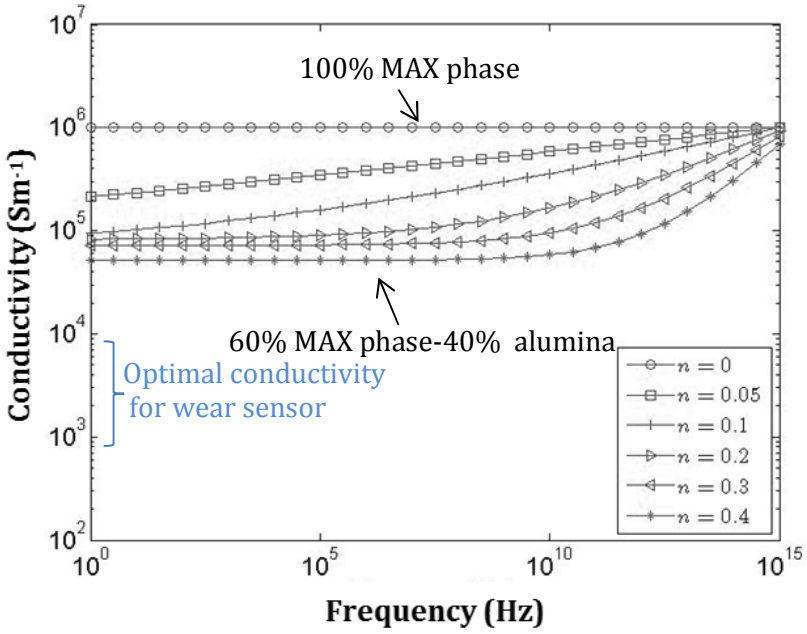

Figure 4.14: *System conductivity of MAX phases with 5, 10, 20,30, 40% alumina as a function of frequency.*

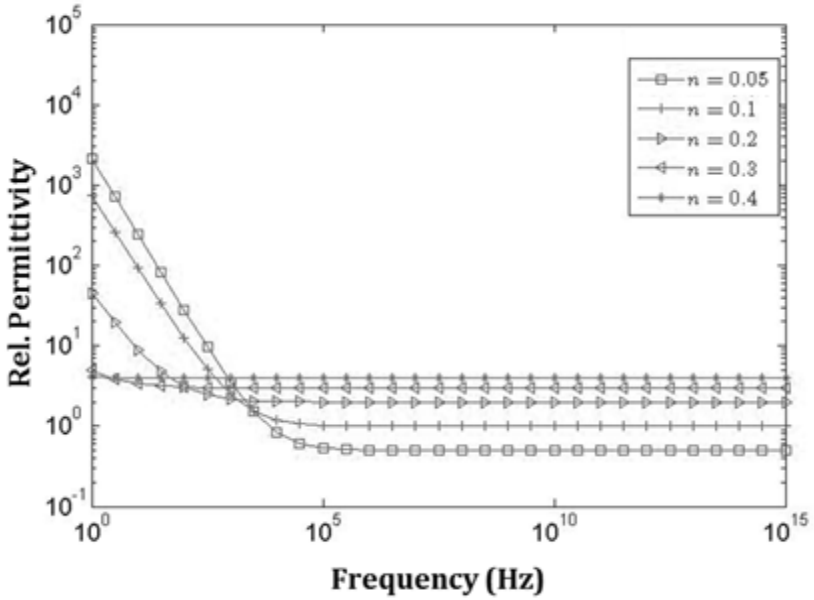

Figure 4.15: *System permittivity of MAX phase with 5, 10, 20, 30, 40% alumina as a function of frequency*

In a network of resistors (MAX phase) and capacitors (alumina) the conductivity and the permittivity at low frequencies are due to the resistors and the capacitors respectively. As the frequency increases the influence of the capacitors becomes obvious, since its ac conductivity is proportional to ωC ($2\pi fC$). As the concentration of alumina increases, the effect of the capacitors is observed at lower frequencies (*Figure 4.14*).

Modelling has proved to be a useful tool in confirming the complex, frequency dependent properties of the material's electrical response. This method may be applied further in future to tune the response to the electrical circuit, as part of the sensor system.

4.3.2 Electrical characterisation of TiO_2 and Magnéli phases (Ti_nO_{2n-1})

In order to understand the electrical measurements of the Magnéli phases they can be compared with the IS measurements of TiO_2 samples. In *Figure 4.16* the ac conductivity and relative permittivity of TiO_2 are presented over a range of frequencies and temperatures. Platinum electrodes were used for the measurements on the TiO_2. The conductivity increases as the temperature increases. In addition, at low temperatures the conductivity increases as frequency increases, whereas at higher temperatures the plateau of the conductivity is larger. This response of the conductivity can be explained in terms of a series of RC circuits, where the grain boundary regions are the capacitors and the bulk material in the grains the resistors [119].

In the initial characterisation, the samples used were Magnéli phases tablets reduced at 1300°C for 6h, using silver electrodes. *Figure 4.17* shows the ac conductivity (S/m) of the Magnéli phases over a range of frequency from 0.1Hz to 0.1MHz and temperature from room temperature to 375°C. Again, as it is observed the conductivity increases with temperature from 25°C to 375°C and it also increases above a certain frequency (> 1kHz) (eq. 20). It has been shown that a power law dispersion of conductivity can be interpreted using a resistor-capacitor (RC) network model.

$$\sigma(\omega) = \sigma_{DC} + A\omega^n, \qquad \textbf{Equation 20}$$

According to this model the increase in frequency-dependent conductivity observed at high frequencies occurs when the capacitive components of the network begin to contribute to the overall conductivity, whereas the frequency independent conductivity at low frequency is taken as a purely resistive dc conductivity (σ_{dc}) [120, 121]. The same graph previously plotted for the titanium dioxide in *Figure 4.16* shows a much lower conductivity (10^{-9} S/m at RT) than the Magnéli phases (10^{-2} S/m at RT), however the Magnéli phases tablets are less conductive than the Magnéli phases reported in the literature (10^{3}-10^{5} S/m at RT)[44, 111, 112]. An explanation of this can be provided by the x-ray diffraction analysis (XRD), section 4.2.2 (*Figure 4.13*), that show that some unreduced TiO_2 is still left in the Magnéli samples.

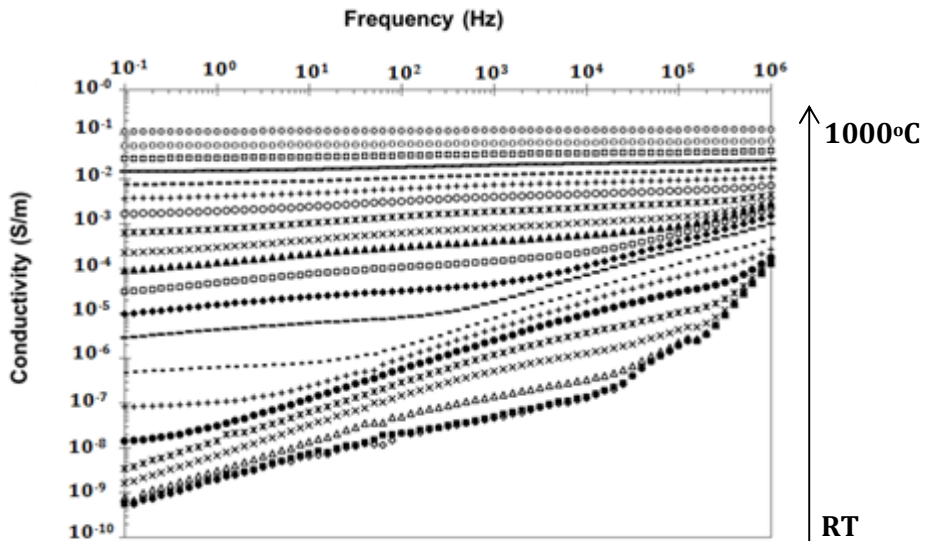

(a)

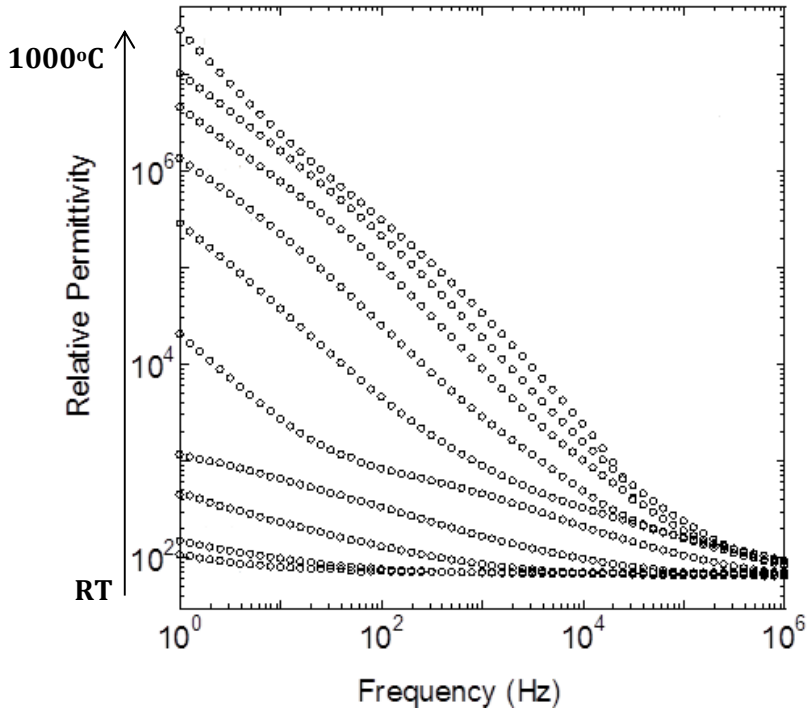

(b)

Figure 4.16: *(a) Conductivity and (b) relative permittivity of titanium dioxide over a range of frequencies and temperatures [39]*

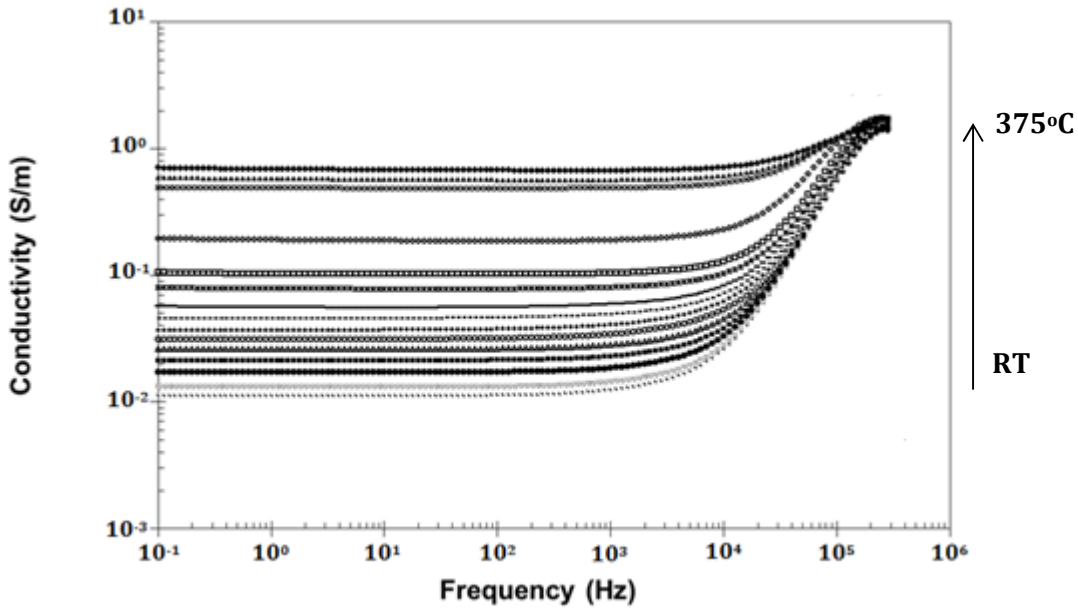

(a)

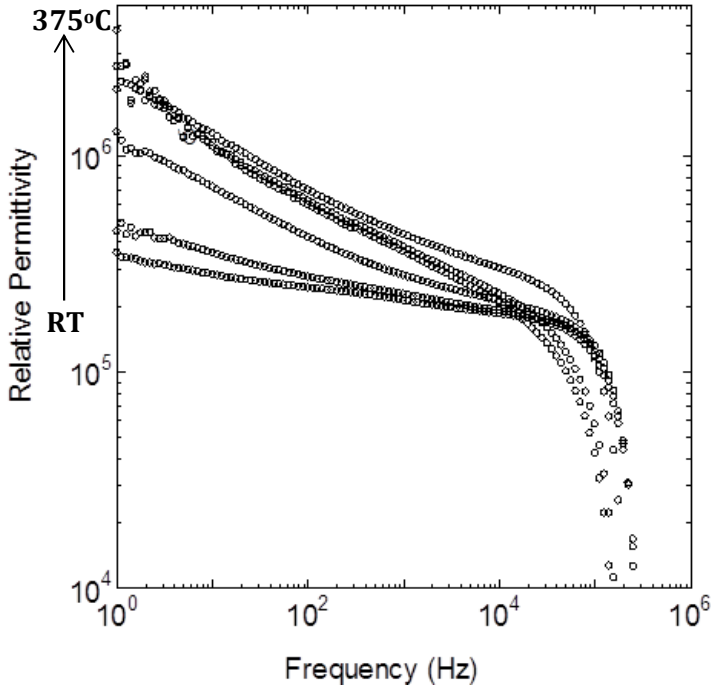

(b)

Fiure 4.17: *(a) Conductivity and (b) relative permittivity of Magnéli Phases over a range of frequencies and temperature [39]*

The impedance plot (Z' against Z'') of Magnéli phases, *Figure 4.18* can be interpreted as the result of two RC elements in series (*Figure 3.24*), where the non-zero intercept (inset of *Figure 4.18*) provides an estimation of the resistance of the bulk of the grains (R_B) which is approximately 12 Ω and accounting for the dimension of the specimens corresponds to a resistivity of 10^{-1} Ω·m. The only observable arc in *Figure 4.18* is assigned to the grain boundary response (R_{GB}), approximately 1400 Ω which leads to a resistivity of 10^2 Ω·m at room temperature. At room temperature R_{GB} is therefore approximately three orders of magnitude higher than R_B, however since R_{GB} decreases systematically with increasing temperature it eventually approaches R_B (~10^{-1} Ω·m) at 375°C.

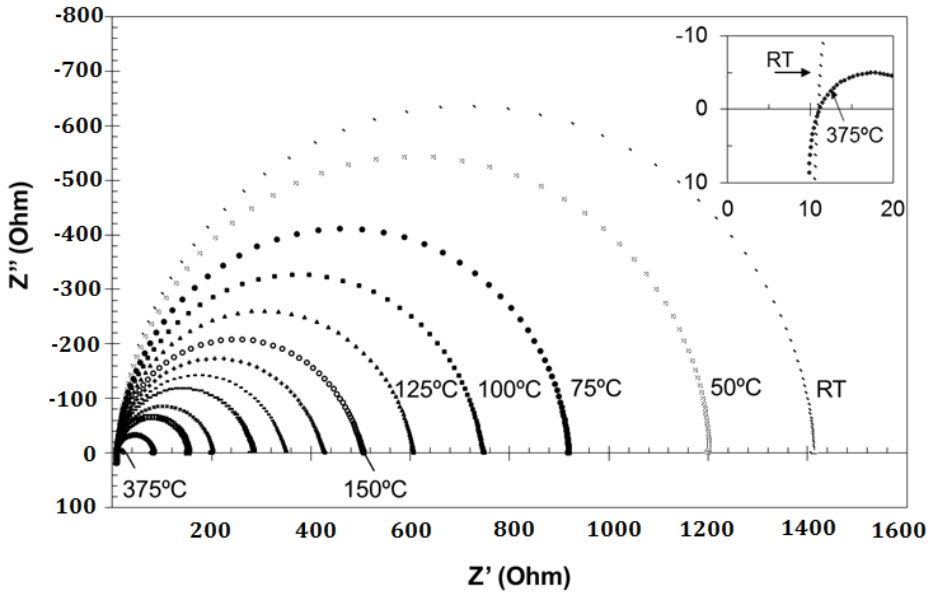

Figure 4.18: *Real Impedance (Z') vs Imaginary Impedance (Z'') for Magnéli Phases over a range of frequency, from 10^6Hz (left) to 0.1Hz (right) [39]*

The activation energy (E_{act}) for the conduction mechanism can be calculated using the Arrenhius' equation:

$$\ln(\sigma_{DC}T) = A - \frac{E_a}{k_B T}, \qquad \textbf{Equation 21,}$$

as described in section 3.2.2, where A is a constant, σ_{dc} is the dc conductivity (S/m), T the absolute temperature (K) and k_B is the Boltzmann constant (eV/K). The dc conductivity was determined at low frequencies (0.1 Hz). The plot obtained for the Magnéli phases is shown in *Figure 4.19* and Table 4.9 shows the calculation of the activation energy.

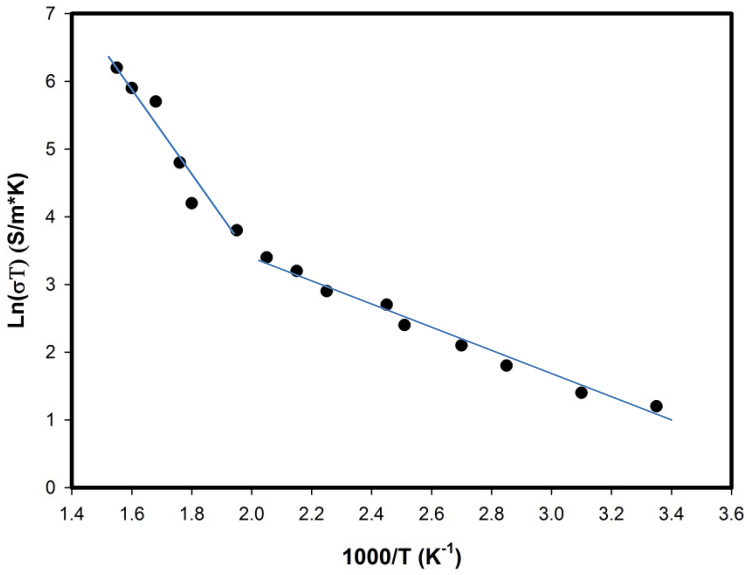

Figure 4.19: *Logarithmic plot of the conductivity of Ti_nO_{2n-1} versus 1000/temperature*

Table 4.9: Activation energy of conduction for Ti_nO_{2n-1} and corresponding conduction mechanism

Temperature range	Activation energy (eV)	Conduction mechanism
RT to 200°C (298 to 473K)	0.14±0.01	Electronic (shallow donor)
250 to 1000°C (523 to 1273K)	0.77±0.08	Electronic (over entire band gab)

The plot shows that the conduction mechanism is different above 500K, since the slope of the plot changes. From RT to 498K the activation energy is 0.14±0.01eV that is attributed to shallow donors in the energy gap mainly due to oxygen vacancies of the remaining TiO_2 (n-type semiconductor), whereas above 500K it is attributed to donors over the entire band gap [124].

A parameter that causes faults in the electrical measurements is that due to the development process and the internal stress, cracks may appear in the tablets that can influence the IS measurements [125] and speed up the re-oxidation at lower temperatures. *Figure 4.20* shows a characteristic response of a sample that probably had a crack and oxidized as the temperature increased. The response is reversed compared with *Figure 4.18*, since the conductivity is decreasing as the temperature is increasing.

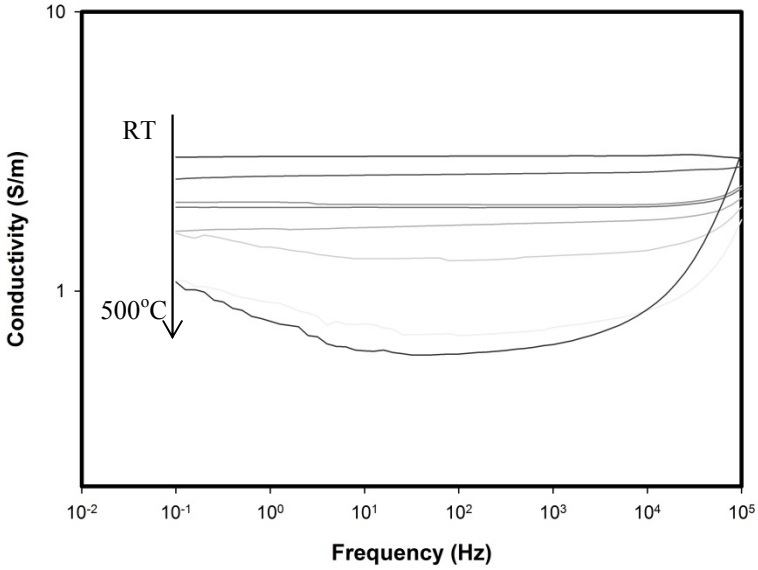

Figure 4.20: *Conductivity of a possible cracked sample over a range of frequency and temperature*

4.4 Discussion

The scope of the work in the current chapter was to conduct further characterisation on bulk samples of the two candidate materials, in order to conclude the material selection process.

Regarding the MAX phase ceramic (Ti_2AlC) the aim was to decrease the conductivity and increase the wear resistance. In order to achieve that, MAX phase samples were prepared containing 5, 10 and 20wt% Alumina aiming to create an alumina layer around the MAX phases grains as shown in *Figure 4.21.*

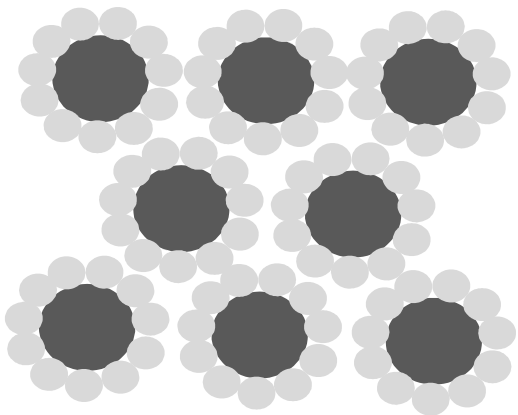

Figure 4.21: *MAX phase (Ti_2AlC) grains with an Alumina layer separating them*

SEM and EDX were conducted to examine the homogeneity of the samples. The images and the analysis showed that there was no second phase in the samples and the Alumina was homogeneously dispersed across the samples. However, the density achieved was not sufficiently high to ensure accurate electrical measurements. More specifically, the highest density achieved was achieved using 10wt% alumina and it was 85.7±1.45% of the theoretical density. The samples containing 20wt% alumina had a lower density, probably because of inhomogeneous mixing of the powders due to the high content of alumina. Higher sintering temperature could be tested to increase the density of the composite or smaller grain size of alumina powder to keep the sintering temperature at 1400^{o}C [126].

Regarding the Magnéli phases the properties matched the requirements for the wear sensor, in terms of electrical conductivity and hardness, therefore it was decided to focus the work on this material. Dense Magnéli phases tablets were manufactured achieving a density up to 97% of the theoretical. The hardness and wear resistance were also within acceptable limits higher than steel. The electrical properties were determined and the conduction mechanism was studied, raising the issue of repeatability, since the manufacturing process for the tablets can cause defects that influence the electrical properties.

According to the characterisation described in the current chapter, the Magnéli phases better matched the requirements of the wear sensor and this material was selected to be the focus of the rest of the work.

The results of the current chapter can be summed up in the following bullet points:

i. MAX phase cannot be sintered to high density (max. density 82% of the theoretical).
ii. MAX phase conductivity too high (10^6 S/m) and wear rate too low (7.19x10-4 mm^3/N.m) for wear sensor application.
iii. MAX phase-alumina composites did not seem to reduce conductivity for model and did not sufficiently increased density and hardness.
iv. Magnéli phases could be sintered to high density (>95% of the theoretical).

v. The electrical conductivity of Magnéli phases can potentially be within the requirements of the application, however optimization of the reduction process is needed.

vi. The hardness (835.2 MHV) and the wear rate (9.46×10^{-7} $mm^3/N.m$) of Magnéli phases was measured close to steel and therefore within the requirements of the wear sensor.

Part of the work on the electrical properties of bulk Magnéli phases in this chapter was published in Solid State Ionics (D. Regonini, V. Adamaki, C. R. Bowen, S. R. Pennock, J. Taylor, A. C. E. Dent, 'Ac electrical properties of TiO_2 and Magnéli phases Ti_nO_{2n-1}', Sol. St. Ionics, 229, 2012, 38-44.

The next step that is described in the following chapter, is the manufacturing of Magnéli phases fibres that will be used in the sensor and Redox batteries application. The manufacturing process of the fibres must be able to produce materials of the same high density and hardness. Additionally, the reduction process needs to be optimized further in order to tune the electrical conductivity, since the fine scale of the fibres, compared to the larger tablets, may influence the diffusion kinetics during the reduction process.

5. Dense ceramic fibres – Development and characterisation

Having completed the material selection based on the results of the dense tablets and having concluded that Magnéli phases were the best candidate ceramic for the wear sensor application, the work now focuses on manufacturing dense Magnéli phases fibres. The green fibres were prepared in the High Performance Ceramics lab of EMPA Institute (ETH Domain) and then sent to University of Bath to sinter and reduce, optimising further the heating treatments to achieve consistent electrical conductivity outcome. The manufacturing process and the structural, physical and electrical characterisation are presented and discussed in the current chapter, including density and hardness measurements, X-ray diffraction, Scanning Electron Microscopy, Thermo-gravimetric Analysis, Impedance Spectroscopy and linearity measurements.

5.1 Development of Magnéli phases fibres

The TiO_2 fibres were produced using a thermoplastic extrusion process. Titanium dioxide powder (Pi_kem, 99.5%, 0.3 µm particle size, specific surface area 7.49 m^2/g) was pre-coated with stearic acid (93661, Fluka Chemie AG, Switzerland). The stearic acid was dissolved in toluene and mixed with the ceramic powder in a ball mill with zirconia milling media for 24h. The toluene was dried out using a rotary evaporator (Rotavapor R-134, Büchi Labortechnik AG, Switzerland). The pre-mixed powder was blended with polyethylene binder (1700MN18C Lacqtene PEBD, Arkema Group, Cedex, France) using a torque rheometer (HAAKE PolyLab Mixer, Rheomix 600, Thermo Scientific, Karlsruhe, Germany). For the two step mixing a temperature of 150°C (1st step) and 120°C (2nd step) was used, according to the requirements of the binder. After mixing a thermoplastic homogeneous feedstock with 54 vol.% of TiO_2 powder was achieved. This feedstock was used for thermoplastic extrusion of fibres with a diameter of 300 µm using a capillary rheometer (RH7-2, Malvern, Herrenberg, Germany) at a temperature of 120°C. A special ceramic die design (Empa, Switzerland) with an orifice of 300 µm was used to produce the fibres. The fibres were extruded with a ram speed of 0.5 mm/s and a pressure of 13 MPa [127]. The 'green' TiO_2 fibres were cut on a conveyor belt into 170 mm long pieces (*Figure 5.1*).

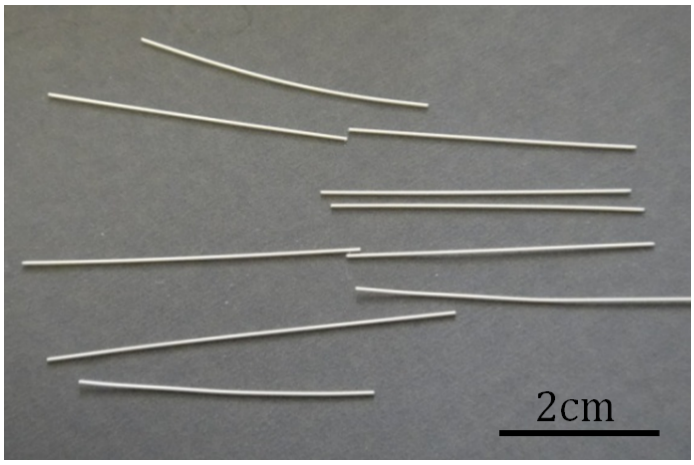

Figure 5.1: *Green TiO_2 fibres (Ø=300 µm, l= 3-8 cm)*

The green fibres were sintered in a chamber furnace (UAF, LENTON, UK) in air following the two sintering profiles presented in *Figure 5.2a* at 1300°C with a step at 500°C in order to burn out the binder. The sintering profile in *Figure 5.2b* was then selected to control the grain growth.

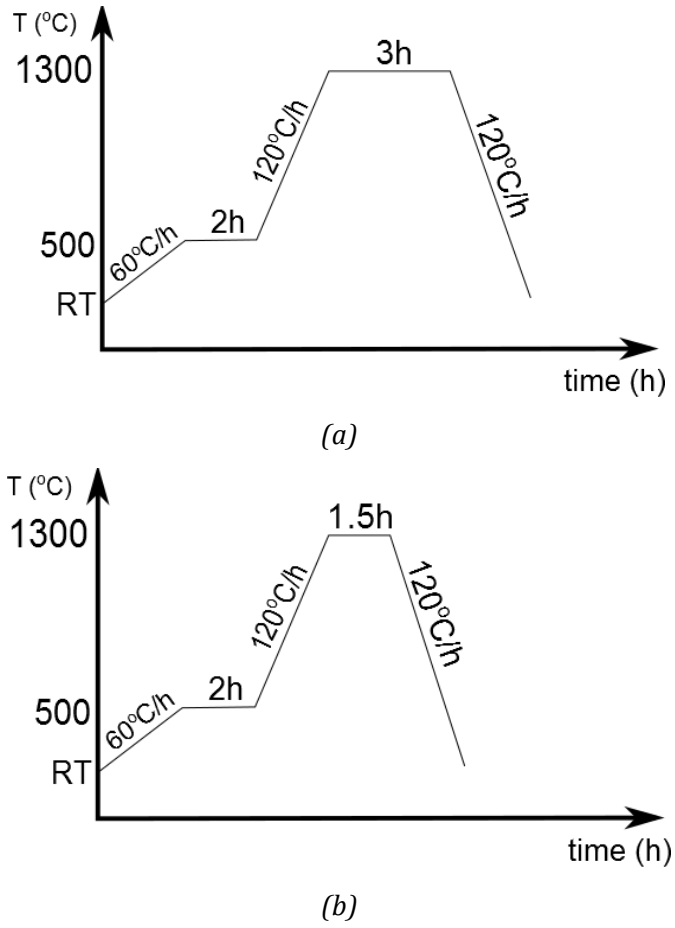

Figure 5.2: *Sintering patterns for the green TiO_2 fibres*

In order to obtain the Magnéli phases fibres the TiO_2 sintered fibres were reduced through a carbo-thermal process performed in a tubular furnace (LTF, LENTON, UK) as described in section 3.1.3. Table 5.1 shows the seven different reduction patterns that were followed. These reduction profiles were chosen based on the work on tablets, in chapter 4, that showed that the phases created are the same at 1300°C for 1, 2, 4, 6 or 8 hours of reduction. Whereas, at lower temperatures initial tests took place at longer durations in order to ensure a homogeneous degree of reduction, since in lower temperatures the diffusion

rate is lower. *Figure 5.3* is a schematic diagram of the process developed to create the Magnéli phases fibres.

Table 5.1: Reduction patterns in order to obtain the Magnéli phases

Reduction temperature(ºC)	Heating/cooling Rate (ºC/h)	Reduction duration (h)
800	150	24
900	150	24
1000	150	12
1100	150	12
1200	150	6
1300	150	1

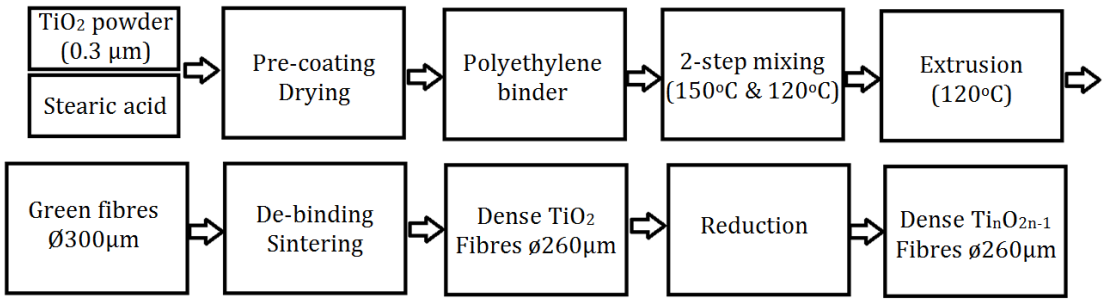

Figure 5.3*: *Diagram of the Magnéli phases fibres manufacturing process

5.2 Physical properties and structural characterisation

In order to determine the density of fibres, it was not possible to use the Archimedes method [85], therefore a simple volumetric method was used. However, the error, especially in the weight measurements, was significant (10%).

Table 5.2 presents the results of the density measurements for all the manufacturing steps of the fibres. The shrinkage of the TiO_2 fibres through the sintering step was 13.3%.

Table 5.2: Density measurements of green and TiO_2 fibres

Material	Process	Volume (cm^3)	Density (g/cm^3)	% theoretical density	Diameter (µm)
green TiO_2 fibres	-	0.00239	3.01 ± 0.06	100	300
sintered TiO_2 fibres	1300°C/1.5h	0.00169	4.20 ± 0.13	99.2	260
sintered TiO_2 fibres	1300°C/3h	0.00169	4.20 ± 0.13	99.2	260

The hardness measurements show a value of hardness similar to that of the tablets (Table 4.4) and are presented in table 5.3**.**

Table 5.3: Hardness measurements of TiO_2 fibres

Sintering process of TiO_2 fibres	Hardness Mean MHV
1300°C for 1.5h	844.7
1300°C for 3h	883.2

Using an optical microscope it was confirmed that the diameter of the green fibres is 300 µm and constant across the length of the fibres (*Figure 5.4*). From the SEM images the grain size and the diameter of the sintered fibres was determined. The grain size of the fibres was determined using ImageJ software across the whole cross-section of the fibres. *Figure 5.5 (a)* and *(b)* show SEM images of sintered fibres for 1.5h and 3h respectively.

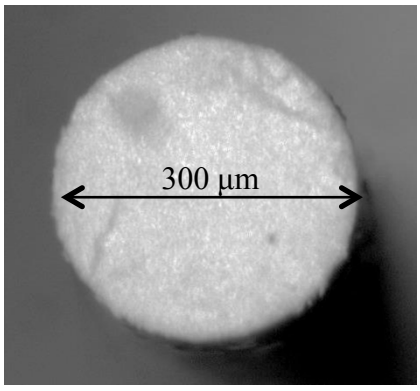

Figure 5.4: *Optical microscope image of TiO_2 green fibre*

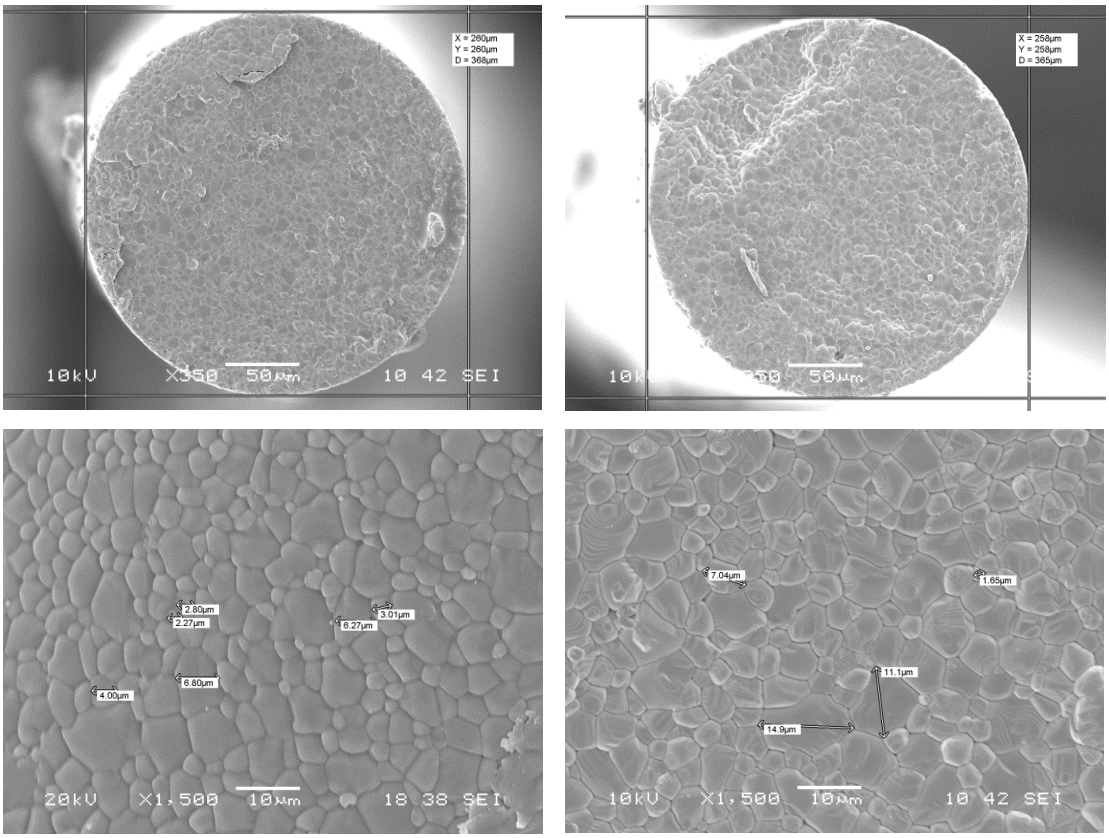

(a) - average grain size 3.6 µm *(b) - average grain size 4.7 µm*

Figure 5.5: *SEM images of TiO_2 sintered fibres for 1.5h (a) and 3h (b)*

The diameter is constant among the fibres at 260 µm. Also, it was observed that the grains are slightly smaller in the fibres that were sintered for 1.5h, so this is the sintering process to be followed for the manufacturing of TiO_2 and Magnéli phases fibres.

Table 5.4 presents the hardness measurements for the reduced fibres for all the reduction patterns followed. Comparing the hardness of the Magnéli phases with that of the TiO_2 fibres (Table 5.3), an increase in hardness after reduction is observed. The same was observed for the tablets (Table 4.4), since after reduction defects and shear planes are created that act as boundaries and make dislocation slip more difficult. To ensure accurate measurements of the hardness three measurements were taken on each tablet, however that was not possible on the fibres due the limited cross-sectional area. One measurement was taken on each fibre and three fibres were used from each batch. Because of the small cross-sectional area, cracks during the diamond penetration may cause errors in the measurements.

Table 5.4: Hardness measurements of Magnéli phases fibres reduced in various temperatures [128]

Reduction process	Hardness Mean MHV
800°C for 24h	799
900°C for 24h	890.42
1000°C for 12h	981.75
1100°C for 12h	977.2
1200°C for 6h	821.31
1300°C for 1h	976.92

Figure 5.6a presents the XRD patterns for the sintered TiO_2 fibres and the fibres carbo-thermally reduced at 800-1000°C. At these reduction temperatures mainly rutile TiO_2 is present, however a wide peak at around 24°, that is characteristic for the Magnéli phases, indicates the presence of a purely crystalline phase of Ti-sub oxides. The colour of fibres is indicative of their composition changes, since it changes from yellowish (TiO_2 fibres) to grey. The fibres reduced at 1200°C and 1300°C had a bluish/black colour that is characteristic of the Magnéli phases and the XRD patterns (*Figure 5.6b*) confirm the presence of Ti_4O_7 that is the most conductive of Magnéli phases.

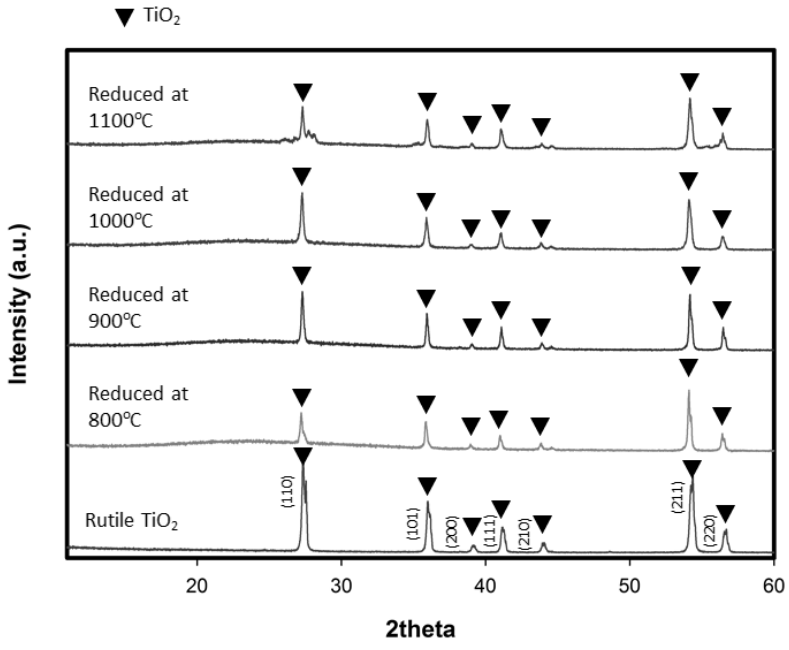

(a)

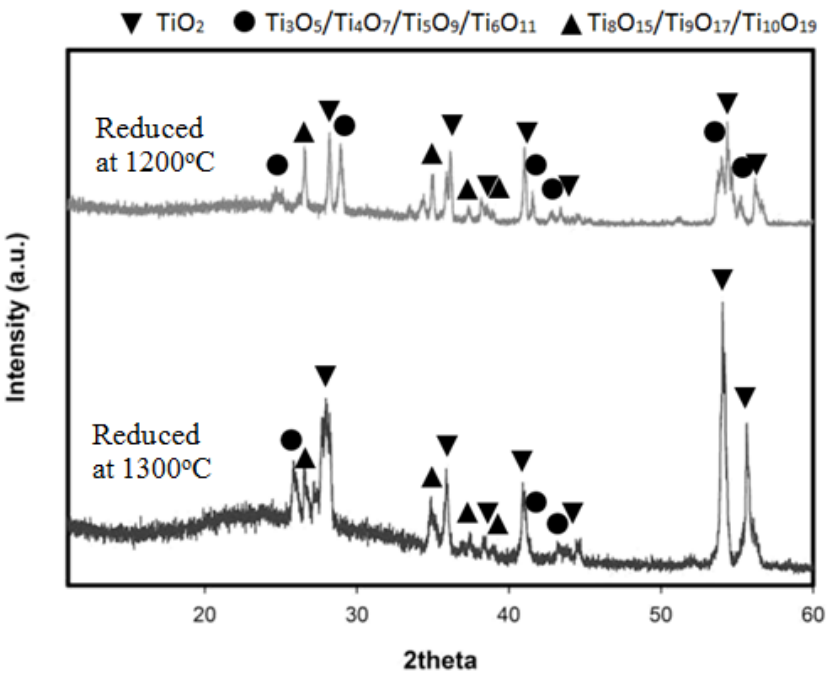

(b)

Figure 5.6: *The XRD patterns for (a) TiO_2 and fibres reduced at 800-1100°C and (b) fibres reduced at 1200°C and 1300°C*

Since the volume of the fibres is much smaller than the bulk tablets, the reduction process will be more rapid as the diffusion rate would be higher. As a result, different reduction temperatures were tested for the fibres with the additional aim to tune the electrical conductivity. Initially, it was observed that the fibres reduced at 800°C, 900°C and 1000°C did not have the characteristic black colour of the Magnéli phases, but were grey, which indicates that these fibres were reduced to a lesser extent.

In order to determine any differences in the microstructure of the Magnéli phases fibres reduced at various temperatures, SEM was used. The SEM images are shown in *Figure 5.7*.

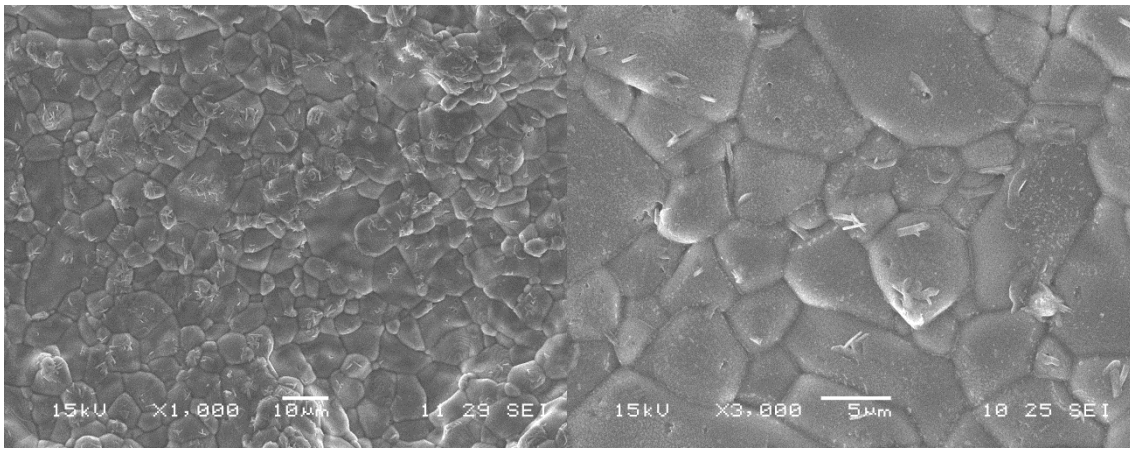

(a) Reduced at 800°C for 24h

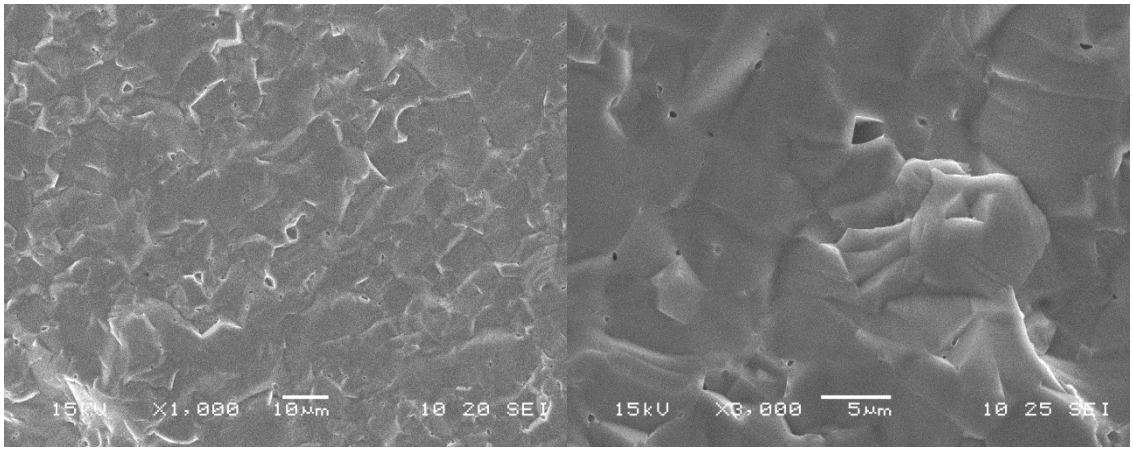

(b) Reduced at 900°C for 24h

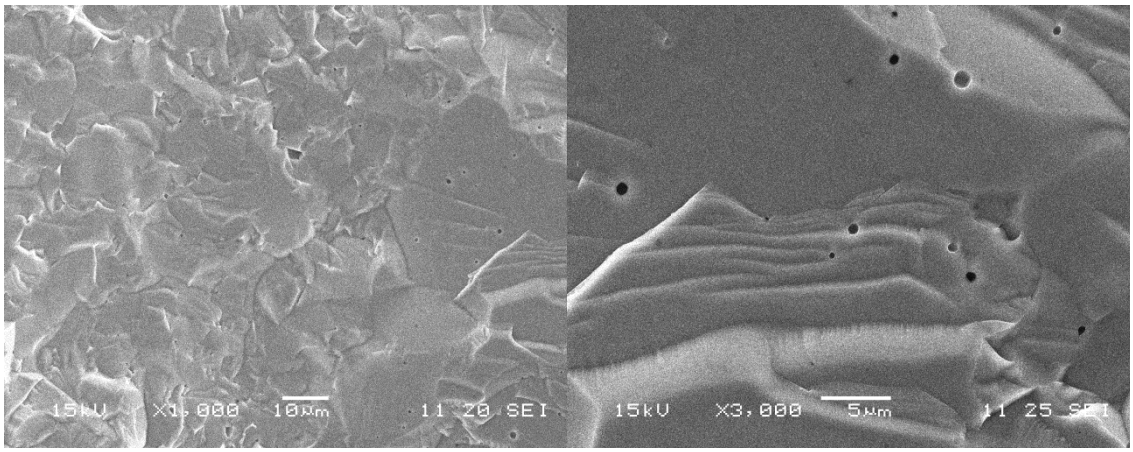

(c) Reduced at 1000°C for 12h

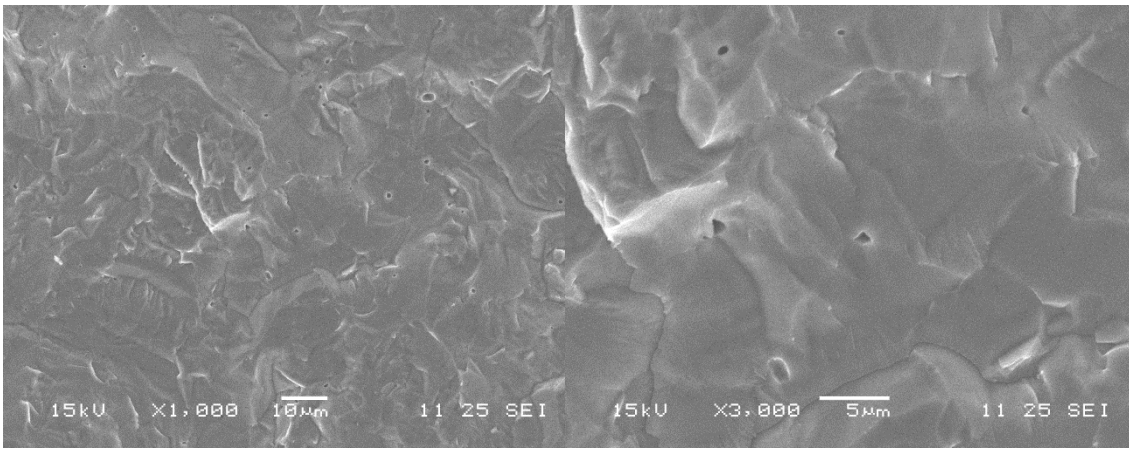

(d) Reduced at 1100°C for 12h

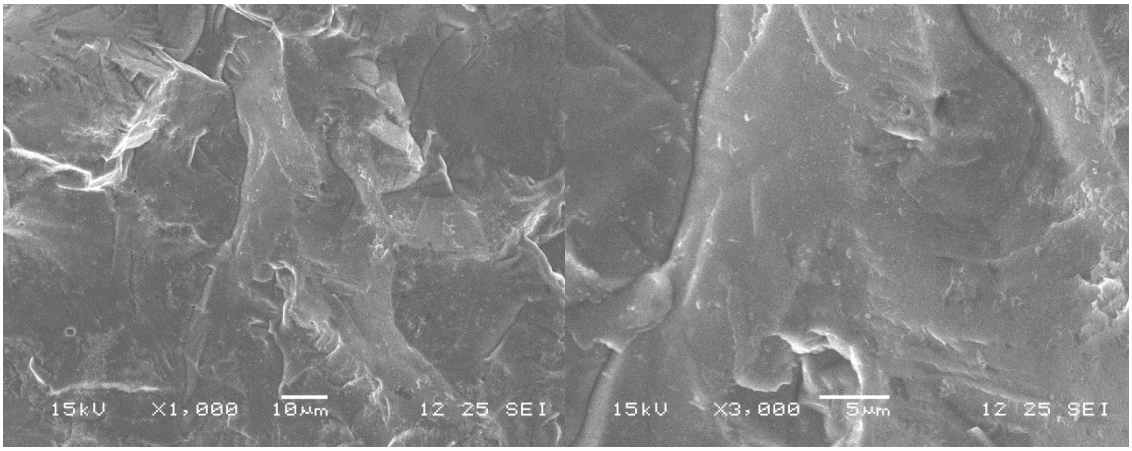

(e) Reduced at 1200°C for 6h

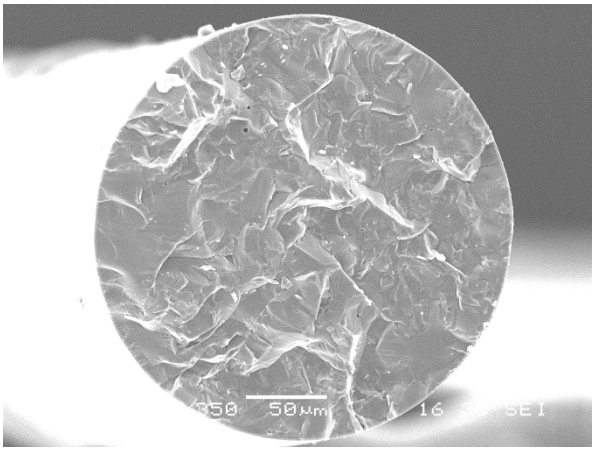

(f) Reduced at 1300°C for 1h

Figure 5.7: *SEM images of the dense fibres reduced at (a) 800, (b) 900, (c) 1000, (d) 1100, (e) 1200 and (f) 1300°C*

In summary, SEM observations indicate that the samples reduced at 800°C for 24h have two phases. The structure of the grains look more like the TiO_2 (also

see *Figure 5.5*) and on the fibre surface a second crystal phase was observed. It is possible that a temperature of 800°C is not enough to activate the diffusion process in order to reduce the TiO_2, as it is also indicated by the XRD spectra (*Figure 5.6*). In addition, there was no grain growth observed, since the grain size was relatively small at around 4 μm. For all the fibres reduced at higher temperature it was not possible to observe two phases and the structure of the grains was similar to the Magnéli phase for the bulk tablets (also see *Figure 4.10*). The fibres reduced at 900°C have a grain size in the range of 10-20 μm (*Figure 5.7*b). In the fibres reduced at 1000°C and higher a significant grain growth was observed with grain sizes from 50 to 100 μm (*Figure 5.7c-f*). Table 5.5 presents the grain size of the six fibre batches.

Table 5.5: Grain size for fibres reduced at various temperatures

Reduction process	Grain size (μm)
800°C for 24h	4
900°C for 24h	10-20
1000°C for 12h	50
1100°C for 12h	50
1200°C for 6h	70
1300°C for 1h	100

To investigate further the structure of the fibres and understand the reduction mechanism, EDX measurements were undertaken. The goal was to determine whether there was composition difference between the bulk material in the grains and the grain boundaries. *Figure 5.8* shows a representative analysis of a fibre reduced at 900°C for 24h. In *Figure 5.8* spectras 2-10 provide information for the grain boundaries and spectras 1 & 11-15 represent spots in the bulk material.

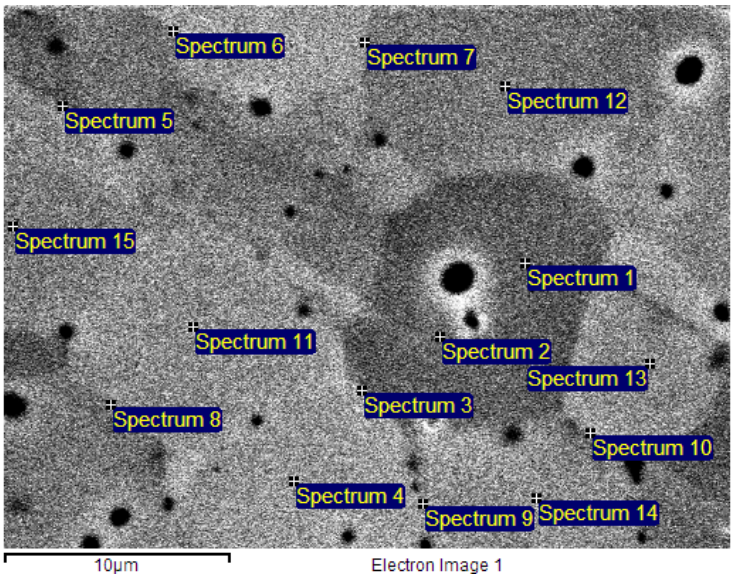

Spectrum	In stats.	O	Ti	Total
Spectrum 1	Yes	43.76	56.24	100.00
Spectrum 2	Yes	43.31	56.69	100.00
Spectrum 3	Yes	42.40	57.60	100.00
Spectrum 4	Yes	43.64	56.36	100.00
Spectrum 5	Yes	43.98	56.02	100.00
Spectrum 6	Yes	44.44	55.56	100.00
Spectrum 7	Yes	43.10	56.90	100.00
Spectrum 8	Yes	43.84	56.16	100.00
Spectrum 9	Yes	43.77	56.23	100.00
Spectrum 10	Yes	44.35	55.65	100.00
Spectrum 11	Yes	43.71	56.29	100.00
Spectrum 12	Yes	43.73	56.27	100.00
Spectrum 13	Yes	44.17	55.83	100.00
Spectrum 14	Yes	43.40	56.60	100.00
Spectrum 15	Yes	43.97	56.03	100.00
Mean		43.70	56.30	100.00
Std. deviation		0.51	0.51	
Max.		44.44	57.60	
Min.		42.40	55.56	

Figure 5.8: *EDX analysis on Magnéli phases fibre [128]*

In *Figure 5.8* and in the rest of the samples, holes and scratches are obvious on the surface. This damage is due to insufficient polishing. The EDX analysis of all the samples (reduced at various temperatures) showed no significant difference in the composition of the bulk material in the grains and in the grain boundaries.

5.3 Electrical characterisation

The various reduction profiles followed for the fibres result in fibres reduced to a different extent. The extent of reduction can also be studied through the electrical properties. Before proceeding with the Impedance Spectroscopy measurements, it is of importance to determine the electrode-wire combination that guarantees an ohmic contact. Ohmic contacts are also crucial for the final application that is based on resistance measurements. Therefore the linearity measurements were conducted on the fibres reduced at 1300°C for 1h that were used in the final application.

5.3.1 Linearity measurements

In order to ensure ohmic contacts for electrical tests Pt, Ag and Al electrodes were tested and *Figure 5.9* shows the linearity measurements. The Pt paste was fired at 600°C, the Ag paste at 610°C and the Al paste at 670°C.

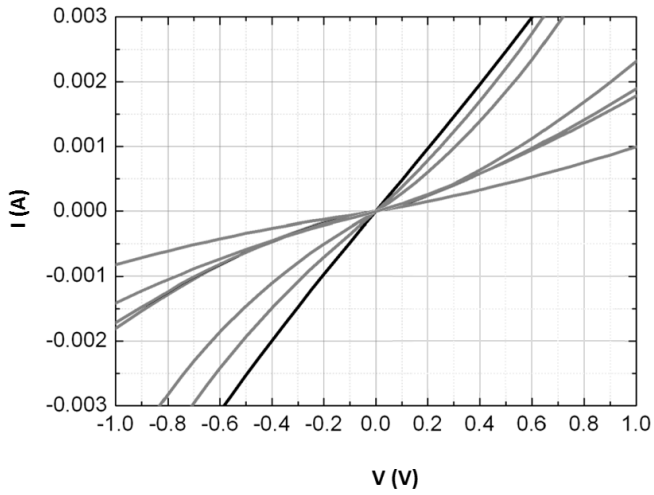

(a)

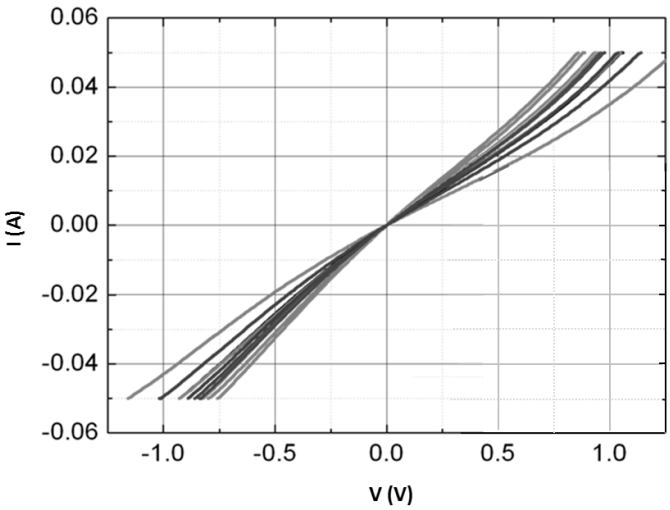

(b)

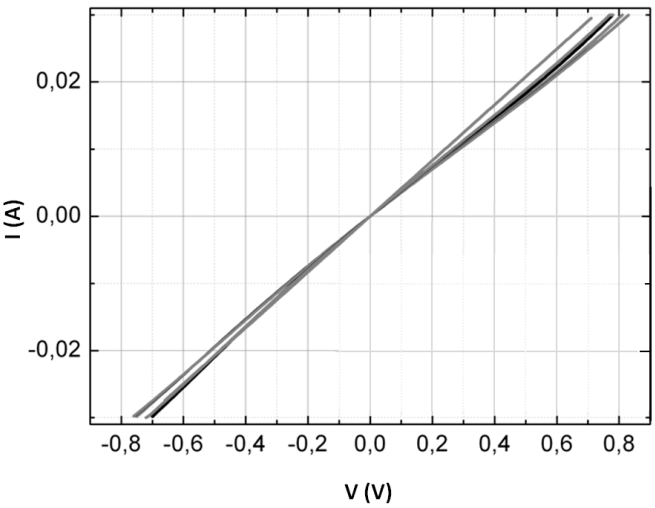

(c)

Figure 5.9: *Linearity measurements using (a) Pt, (b) Ag and (c) Al electrodes [12]*

Figure 5.9 shows that the most consistent I-V and linear (ohmic behaviour) response between fibres were achieved using Al electrodes; these were used for further characterisation. Non-ohmic behaviour was observed for Pt and Ag. Non-ohmic electrode contacts to semiconducting oxides are a well-known phenomenon where Schottky barriers develop at the metal-semiconductor interface due to mismatch in the Fermi energy levels of the sample and electrode metal [129]. Pt and Ag are common electrode materials for characterisation of low conductivity ceramic materials where non-ohmic behavior is not an issue. In the case of Magnéli phases electrode selection is important for characterization of the material.

5.3.2 Impedance Spectroscopy

The low frequency (1Hz) measurements of the conductivity are shown in *Figure 5.10* and confirm the presence of Ti-sub oxides in the fibres reduced at 800-1100^{o}C, since their conductivity is between 10^{-1}-10 S/m. The same was indicated from the XRD spectra by the presence of a wide peak at approximately 24^{o} that is characteristic of the Magnéli phases and shows the presence of a purely crystalline phase of Ti-sub oxides (*Figure 5.6*). It is also clear the samples reduced at 1200^{o}C and 1300^{o}C have metallic conductivity between 10^{3}-10^{4} S/m. In all the samples it was possible to tune the electrical conductivity in a range of five orders of magnitude (10^{-1}-10^{4}). From the low frequency measurements it was also clear that it was difficult to obtain consistent results in the samples reduced at lower temperature, probably because the diffusion process is slow and it is more difficult to obtain a homogenous degree of reduction through the fibres. On the other hand the results were very consistent for the fibres reduced at 1200^{o}C and 1300^{o}C with a deviation of ±1297 S/m and ±357 S/m respectively.

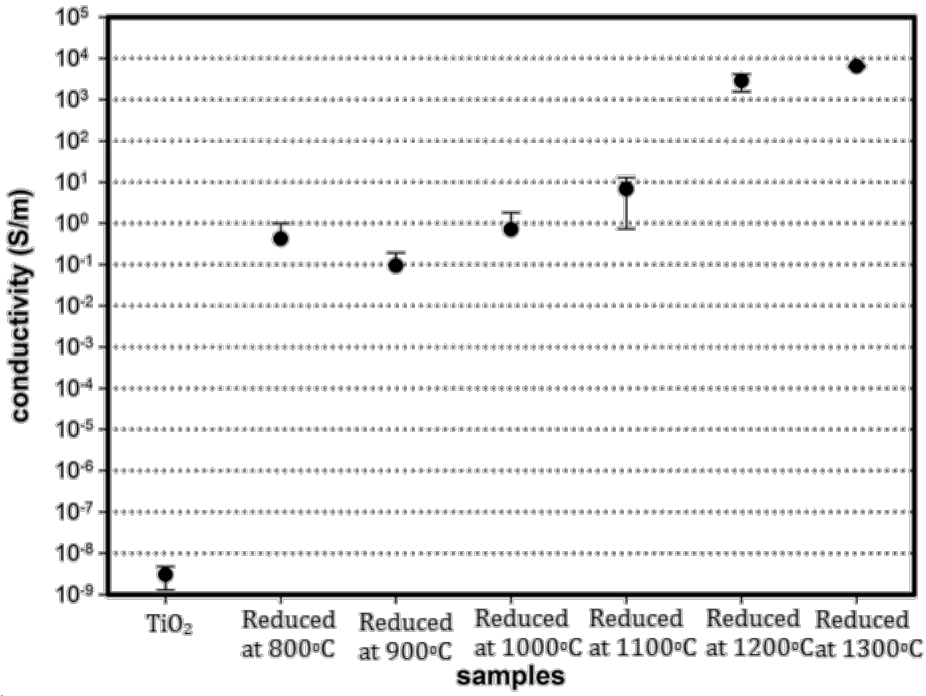

Figure 5.10: *Low frequency electrical measurements for TiO_2 fibres and fibres reduced at various temperatures*

Measurements in a wide range of frequencies (1-10^5 Hz) were also conducted for the fibres reduced at 1200°C and 1300°C and the results are shown in *Figure 5.11*. It is clear that the fibres behave as resistors, since their conductivity is frequency independent, confirming that no insulating layer of TiC has developed. On the other hand the TiO_2 fibres behave as capacitors since the conductivity is frequency dependent. The measurements were conducted scanning the frequencies up to 10^5 Hz, because at higher frequencies the inductance effect from the wires would be greater. *Figure 5.12* presents the phase shift of TiO_2 fibres and fibres reduced at 1200°C and 1300°C over the same range of frequencies, confirming that the fibres reduced at 1200°C and 1300°C respond as almost ideal resistors having a phase shift slightly above 0°, whereas TiO_2 fibres respond as almost ideal capacitors having a phase shift slightly below 90°.

Following the electrical characterisation the fibres reduced at 1300°C for 1h were chosen for use as a sensing element in the wear sensor application. These fibres had the highest conductivity and the smallest deviation in conductivity values.

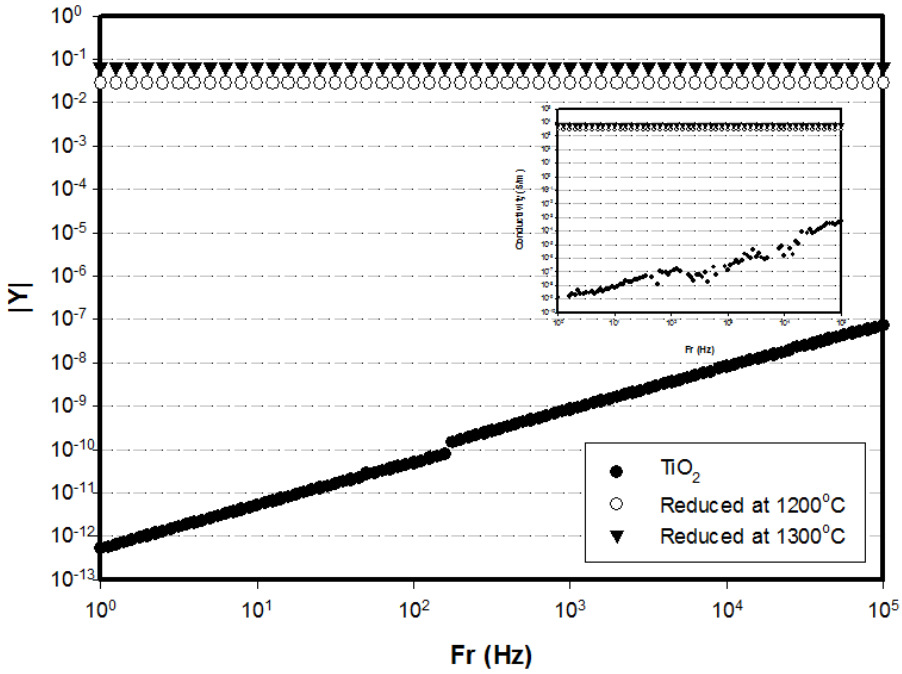

Figure 5.11: *Modulus of conductivity of TiO_2 fibres and fibres reduced at 1200°C and 1300°C over a range of frequencies. Inset shows real part of ac conductivity with frequency*

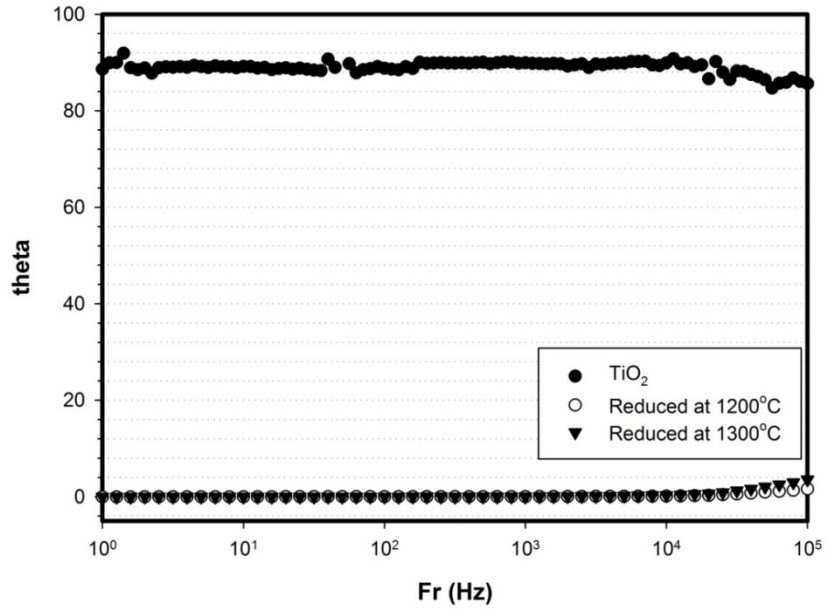

Figure 5.12: *Phase angle of TiO_2 fibres and fibres reduced at 1200°C and 1300°C over a range of frequencies.*

5.4 Thermo-gravimetric analysis

For applications that require a high temperature or oxygen rich applications, such as the wear sensor and energy storage applications, the thermal stability of the Magnéli phases is a feature that needs to be taken into consideration and analysis of the re-oxidation process of dense fibres by thermo-gravimetry (TGA) was undertaken for the fibres reduced at 1300°C that were used for the final application. The activation energy of the re-oxidation process was calculated and the analysis provided an insight on the kinetic oxidation mechanism. *Figure 5.13* shows the heating profile used to study the oxidation mechanism.

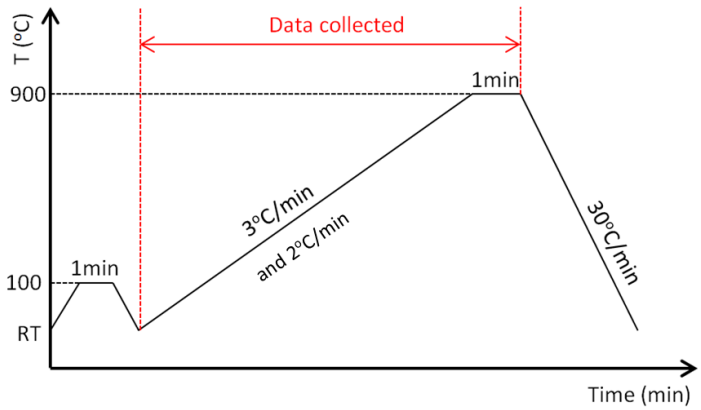

Figure 5.13: *TGA temperature profile*

After re-oxidation of the Magnéli fibres, the XRD (*Figure 5.14*) shows the presence of only rutile TiO_2. The presence of a very broad peak at approximately 25° may indicate the presence of some amorphous or purely crystalline phases of Ti-sub-oxides left in the samples.

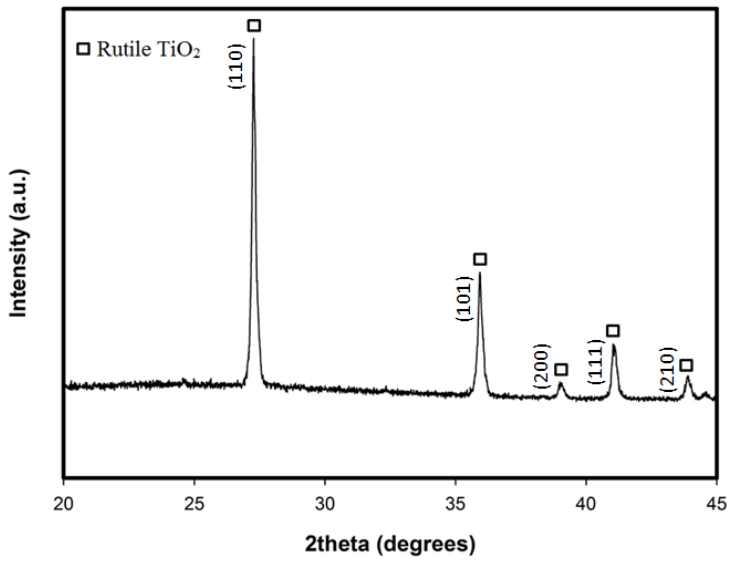

***Figure 5.14**: XRD spectrum of the re-oxidised samples*

Scanning electron microscopy images of the sintered TiO_2 fibres (*Figure 5.5a*) and the Magnéli fibres (*Figure 5.7*) indicate that both have high density with limited porosity and cracks visible. *Figure 5.15* shows a cross-section of the re-oxidized fibres, where cracks are observed along the grain boundaries (*Figure 5.15b*) and the fibres fracture more easily during handling.

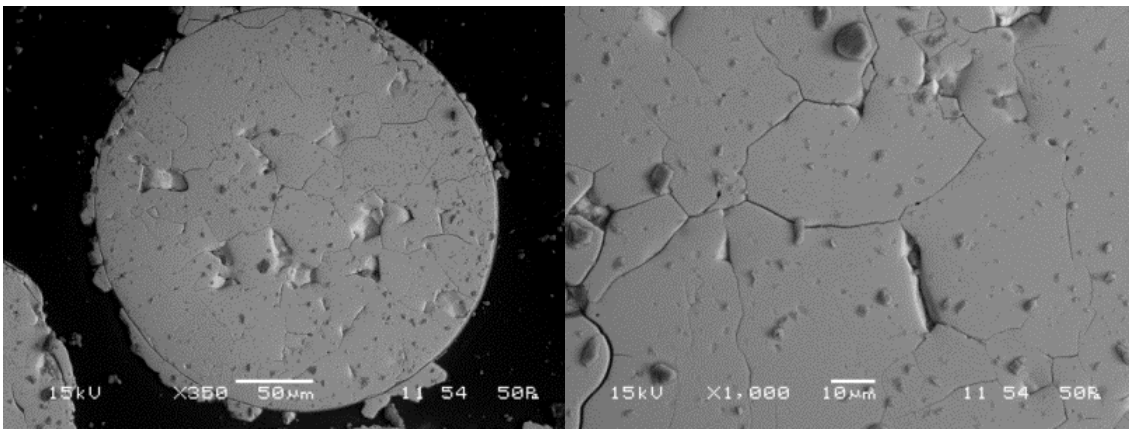

(a) *(b)*

***Figure 5.15:** SEM images of the re-oxidized fibres*

Following calibration of the data using the sample free measurement, *Figure 5.16* shows the mass change (α) as temperature increases for a heating rate of 3°C/min and 2°C/min. The mass change is defined as:

$$\mathbf{a} = \frac{\mathbf{w_0 - w}}{\mathbf{w_0 - w_f}}, \qquad \textbf{Equation 22,}$$

where w_0, w and w_f are the initial, actual and final sample mass respectively.

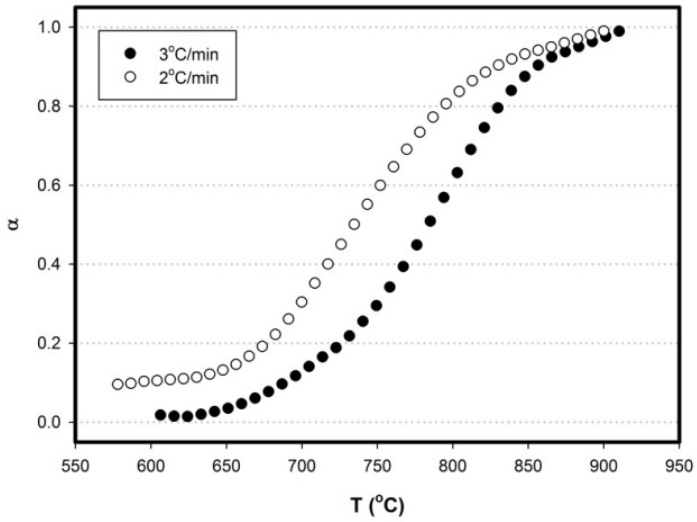

Figure 5.16: *TGA experimental curves for 3°C/min and 2°C/min heating rates*

The re-oxidation of the Magnéli fibres begins at 650°C and the temperature for α=0.5 is 734°C and 781°C for heating rates 2°C/min and 3°C/min respectively. A temperature of 650°C is above the operation temperature for the sensing and the energy storage applications, but can set the operation limit for any other applications.

In order to begin the analysis it is assumed that the reaction rate obeys the Arrhenius law:

$$\mathbf{k = Aexp}\left(-\frac{\mathbf{E_a}}{\mathbf{RT}}\right), \qquad \textbf{Equation 23}$$

where A is the pre-exponential factor, E_a is the activation energy, R is the gas constant and T the absolute temperature. The reaction rate depends on the conversion according to the general equation:

$$\frac{\mathbf{da}}{\mathbf{dt}} = \mathbf{kf(a)}, \qquad \textbf{Equation 24}$$

where f(a) is a function depending on the kinetic model. Taking into consideration eq. 24 and the heating rate ($\beta = dT/dt$), the Arrhenius equation can be written as:

$$\ln f(a) = \frac{E_a}{RT} + C, \quad C = \ln \frac{AdT}{\beta da}, \qquad \textbf{Equation 25}$$

During a solid state reaction, a layer of the product (in this case TiO_2) often initially forms and gradually covers the surface of the reactant. The diffusion of the reactant (oxygen) through the product is slower than the surface reaction and becomes the rate controlling mechanism of the overall reaction; whereas surfaces, grain boundaries and defects are favourable migration paths. In this case four functions are used for the kinetic study (Table 5.6) [130-133]. The simplest rate equation is for an infinite flat plane that does not involve a shape factor (D1). Two-dimensional diffusion (D2) assumes that the solid particles are cylindrical and diffusion occurs though a cylindrical shell. The 3-dimensional models are based on the assumption of spherical solid particles. If x is the thickness of the reaction zone, Jander (D3a) used a simplified equation to define it, where Ginstling and Brounshtein (D3b) take into consideration that the thickness of the reaction zone is increasing as the reaction continues.

Table 5.6: Diffusion kinetic models

Dimension	Kinetic model	Function *f(a)*
D1	One dimensional diffusion	$1/(2\alpha)$
D2	Two dimensional diffusion	$-\{1/\ln(1-\alpha)\}$
D3a	Three dimensional diffusion (Jander)	$\{3(1-\alpha)^{2/3}\}/\{2(1-(1-\alpha)^{1/3})\}$
D3b	Three dimensional diffusion (Ginstling-Brounshtein)	$3/\{2((1-\alpha)^{-1/3}-1)\}$

If it is assumed that C is a constant in Equation 25, since the mass increases as a linear function of time, plots of lnf(a) versus 1/T should be linear having a slope E_a/R. It is possible to obtain the value of the activation energy from a single experiment but it is necessary to assume a relevant diffusion mechanism

(kinetic model in table 5.6). In order to confirm the diffusion mechanism, the analysis was carried out using two heating rates and the iso-conversional method [134]. Equation 26 for both heating rates was used to calculate the activation energy without knowledge of the diffusion mechanism and is expressed as:

$$E_a = \frac{R}{\frac{1}{T_1}+\frac{1}{T_2}}\left(\ln\frac{\beta_2}{\beta_1} + \ln\frac{da_2}{T_2} - \ln\frac{da_1}{T_1}\right), \quad \textbf{Equation 261}$$

where β_1 and β_2 are the heating rates 3°C/min and 2°C/min respectively, α_1 and α_2 are the conversion rates for the two heating rates and T_1 and T_2 are the temperatures for the corresponding α_1 and α_2.

Figure 5.17 shows the plots using the kinetic models of *f(a)* in Table 5.6 for the two heating rates, indicating excellent linearity in both cases. The calculated activation energies (by the calculation of the slope of the graphs in *Figure 5.17*) for the diffusion kinetic models are summarised in Table 5.7.

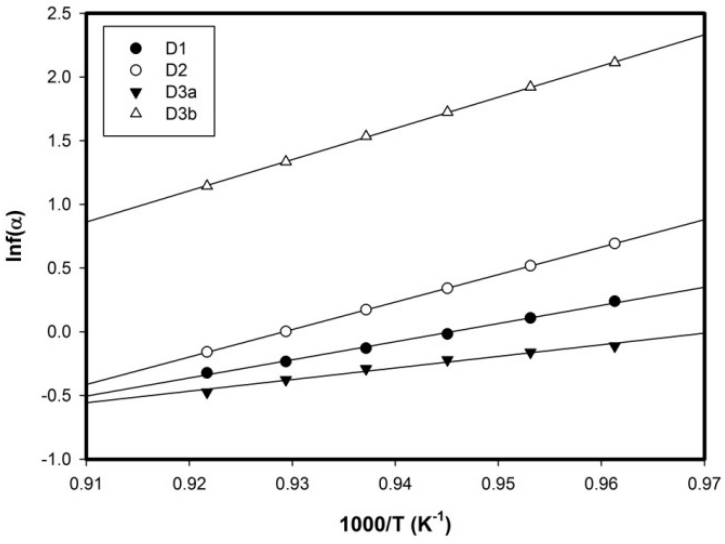

(a)

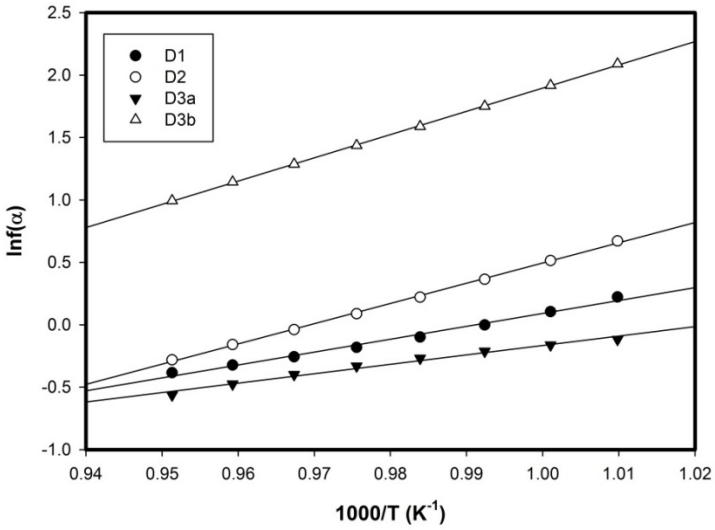

(b)

Figure 5.17: *Temperature dependence of lnf(a) for the diffusion models at (a) 3°C/min and (b) 2°C/min*

Table 5.7: Activation energy from re-oxidation data

Kinetic model	**E_a(eV) (3°C/min)**	**E_a(eV) (2°C/min)**
One dimensional diffusion – D1	1.33	0.88
Two dimensional diffusion – D2	1.85	1.39
Three dimensional diffusion (Jander) – D3a	0.78	0.64
Three dimensional diffusion (Ginstling-Brounshtein)-D3b	2.11	1.6

As described in section 3.2.1 it is possible to determine the activation energy without knowing the diffusion mechanism by using the iso-conversional method (eq. 26). The activation energy calculated using this method at $\alpha_1=\alpha_2=0.5$ is E_a= 0.71 eV. This value agrees with the value estimated using Jander's three dimensional diffusion model (D3a). Jander's model is limited by diffusion of one of the components through a layer of the product, which is sensible given that this is the case in the re-oxidation process of the Magnéli phase fibres. The reaction rate is controlled by the diffusion rate of oxygen through layers of TiO_2 initially created on the surface and around the grain boundaries. Oxygen is diffused in the bulk of the grains thought the defects (oxygen vacancies) created during reduction. Jander's model does not take into consideration that the thickness of the reaction zone is increasing as the reaction proceeds and in

some cases is more representative of the initial stages of the reaction. In the case of the re-oxidation of Magnéli phases the model may be more appropriate due to the high density of defects. The value of the activation energy is also in good agreement with the value of 0.77±0.08eV measured from conductivity data using impedance spectroscopy at temperatures from 250°C to 375°C, as seen in section 4.3.2 [124]. The conduction mechanism through oxygen vacancies is also a thermally activated process and the activation energy was calculated using the Arrhenius equation.

5.5 Discussion

The aim of the work presented in this chapter was to manufacture dense Magnéli phases fibres in order to use them in the wear sensor. The reduction process was optimized in order to achieve high conductivity and consistency between fibres. At the same time various reduction profiles were followed in order to tune the conductivity of the fibres for other potential applications that are going to be discussed in section 9.2 on future work.

To summarize the achievements of this work:

i. A variety of high conductivity titanium sub-oxides fibres, including Magnéli phases (Ti_nO_{2n-1}, $3<n<10$) were prepared.

ii. Using the manufacturing process described it was possible to produce dense (>96% of the theoretical) conductive fibres.

iii. The process is able to tune the conductivity of the reduced fibres by five orders of magnitude (10^{-1}-10^4 S/m).

iv. Magnéli phases fibres that were reduced at 1200°C and 1300°C provided the most consistent and highest electrical conductivity.

v. Ohmic contacts were achieved using Al electrodes and silver wires, that were also strong and stable that is essential fo the integration of the wear sensor.

vi. The operational limit was determined by studying the re-oxidation mechanism at high temperatures, that is 650°C, much higher than the operation temperature of the wear sensor.

The work in this chapter was published in the Journal of Materials Chemistry A (V. Adamaki, F. Clemens, P. Ragulis, S. R. Pennock, J. Taylor and C. R. Bowen, 'Manufacturing and characterisation of Magnéli phase conductive fibres', J. of Materials Chemistry A RSC, 2, 2014, 8328-8333)[124] and in Journal of Material Science (V. Adamaki, F. Clemens, J. Taylor, T. J. Mays, C. R. Bowen, 'Re-oxidation mechanism and kinetics of fine scale Ti-Magnéli phases in fibre form using thermogravimetric analysis', J. of Mat.Science, DOI 10.1007/s 10853-014-8468-9)[136].

The integration of the wear sensor that the Magnéi phases fibres (reduced at 1300^{o}C) is described in chapter 7.

Having gained experience on the Magnéli phases, a collaboration with University of Southampton started in order to test the Magnéli phases for electrodes in Redox flow batteries. To better match the requirements for this application, samples with increased surface area were manufactured. The manufacturing process of bulk samples and fibres and their characterisation is described in the following chapter.

6. Porous ceramics bulk and fibres- Development and characterisation

This chapter presents the manufacturing process of porous ceramic tablets and porous fibres in order to increase the surface area and test them for electrodes in Redox flow batteries. It also presents the physical and structural characterisation of the manufactured fibres. Preliminary tests to determine the appropriate sintering profile and to examine the electrochemical behaviour were initially made on bulk materials (tablets). As the result of the promising results obtained from the manufacturing and testing of porous bulk materials, porous fibres were produced during a three months visit to EMPA, in collaboration with Dr Frank Clemens in the High Performance Ceramics Laboratory. As described in chapter 1, the porous bulk samples and fibres were characterised in terms of electrochemical properties in collaboration with Dr Richard Wills and Ms Maria Kourasi from the University of Southampton.

6.1 Development and characterisation of porous bulk ceramics

Working with small scale fibres means high surface area and the high surface area and electrical conductivity of the Magnéli phases ceramic make it an attractive material for a battery electrode. To increase further the active area of the material for the electrode application, one approach is to produce porous materials and more specifically to concentrate porosity close to the fibre surface. As described in chapter 5 for dense fibre development, the initial tests were made on bulk tablets where attempts were made to increase the porosity by simply increasing the binder content when shaping the tablets. The increase in the porosity level with binder content was determined with density measurements and SEM images that also aided in examining the effect of the porosity in controlling the grain growth. As described in chapters 4 and 5, large grain growth was observed in the manufacturing of dense material. The porosity was also expected to influence the reduction process, therefore XRD was used to determine the phases present in the porous samples. Because of the high porosity, electrical measurements are unlikely to be accurate, therefore knowledge of the phases present is crucial in order to estimate the electrical conductivity.

6.1.1 Development of porous bulk samples

In order to achieve high surface area to meet the requirements for battery electrodes, the manufacturing process was changed to increase the porosity and limit the grain growth. The electrical conductivity should be as high as possible for such applications, so the heat treatment for sintering and carbo-thermal reduction needs to be at a maximum of 1300^{o}C to create the most conductive phase, namely Ti_4O_7 (see chapter 4).

As described in section 4.1.2, for the manufacturing of high density green tablets, 2.5wt% organic binder (polyethylene glycol-PEG 8000) was used. In order to generate porosity higher binder contents were examined; the binder is burnt out during heat treatment to leave behind residual porosity. The TiO_2 mixes were prepared with 2.5, 5, 7.5, 10, 20 and 50wt% binder to create a range of porosity levels as shown in Table 6.1.

Table 6.1: High binder concentration batches

Batch No	wt% binder
1	2.5
2	5
3	7.5
4	10
5	20
5b	20
6b	50

A titania slurry was then created with the addition of distilled water (1ml per 1g of powder) and ball milled for 24h using the apparatus. The slurry was then dried and the powder sieved through a 45µm mesh. TiO_2 tablets were formed by dry cold pressing, applying a pressure of ~250MPa (~20kN over an area of $1cm^2$).

The work presented in chapter 4 showed that using a 'two-step' heating treatment, namely sintering TiO_2 in air at 1300°C and an additional heat treatment to form Magnéli phases by carbo-thermal reduction at 1300°C, led to excessive gain growth. In order to prevent such large grain growth a 'one-step' preparation method was employed whereby both sintering and carbo-thermal reduction stages were combined into one process in a tubular furnace with carbon black powder under constant argon flow. The heating profile is an initial slow heating at 60°C/hr to 400°C and dwell for 3hr to burn out the binder, followed by heating at 120°C/hr to 1300°C and a dwell for 1hr for sintering and reduction and then cooling of 150°C/hr to room temperature (*Figure 6.1*).

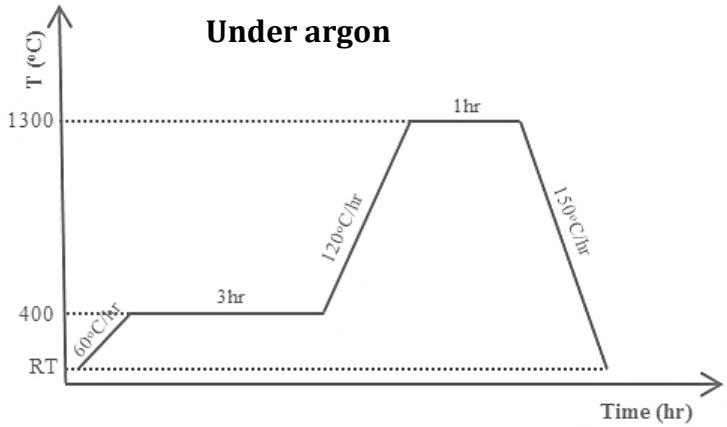

Figure 6.1: *'One-Step' process to sinter and reduce the green tablets (for batches 1-5)*

At higher binder contents (>20wt%) the heating profile was changed with a slower heating of 40°C/hr to 400°C and a dwell for 3hr, a heating at 40°C/hr to 1300°C and a dwell for 1hr and then cooling of 150°C/hr to room temperature (*Figure 6.2*); this lower heating rate enables the highly porous green body to maintain a volume similar to the initial pressed 'green' bodies.

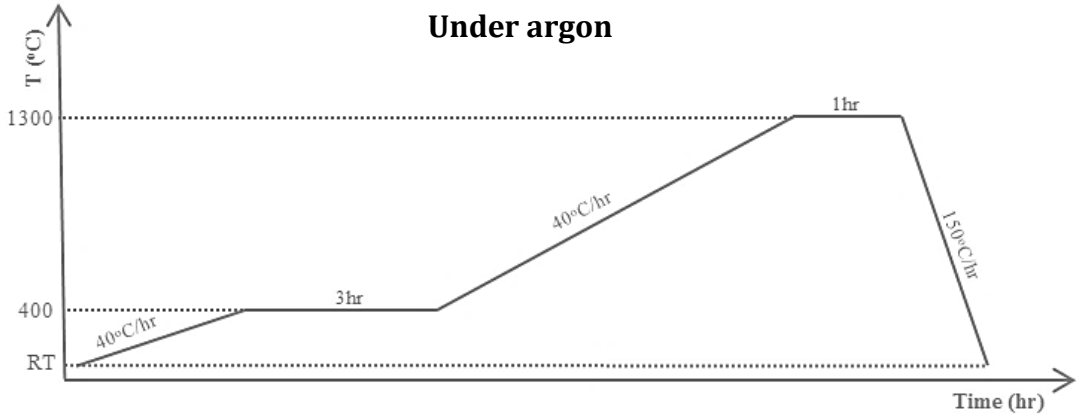

Figure 6.2: *One-Step process to sinter and reduce the green tablets (for batches 5b & 6b)*

6.1.2 Physical properties and structural characterisation of porous bulk samples

Density and the apparent porosity of the bulk sintered tablets were measured according to the BS EN623-2:1993 standard. Table 6.2 compares the density and the porosity measurements for all the batches prepared with the 1-Step preparation method with increasing content of binder. The properties of the dense tablets prepared with 2.5%wt binder and using the 2-Step preparation are also included as reference; in this case the carbo-thermal reduction takes place after initially sintering the TiO_2 in air to high density, as described in section 4.1.2.

Table 6.2: Density measurements of porous of porous bulk samples

Batches No	wt% binder	Theoretical density ($g.cm^3$)	Bulk density ($g.cm^3$)	Apparent solid porosity (%)	% Theoretical density
2-Step dense samples	2.5	4.3	4.19±0.03	0.17±0.17	97.41±0.63
1	2.5	4.3	4.00±0.02	3.02±0.34	93.07±0.58
2	5	4.3	4.01±0.03	2.87±0.44	93.31±0.64
3	7.5	4.3	3.75±0.09	5.62±2.09	87.28±2.08
4	10	4.3	3.94±0.04	1.78±0.53	91.63±0.93
5	20	4.3	3.57±3.95	2.43±1.15	89.82±1.00
5b	20	4.3	2.88±0.06	7.68±2.70	66.92±1.51
6b	50	4.3	1.45±0.03	64.92±0.69	33.87±0.77

There is an increase in porosity level with added binder that reaches a maximum of 64.92% with 50wt% binder, therefore these samples would be better suited for applications that require high surface area such as electrodes.

All the samples were also examined using the SEM JEOL6480LV and the images were analysed using the ImageJ software in order to determine accurately the porosity and the grain size. The images in *Figure 6.3* present and compare a plan view of the samples containing 2.5%wt binder prepared with the 2-Step (dense samples) and 1-Step process. Whereas the images in *Figure 6.4* show a cross-section view of the 2.5, 5, 7.5, 10, 12.5, 20 and 50%wt binder Magnéli phases tablets prepared with the 1-Step process. The effect of the binder content on the porosity of the tablets is apparent.

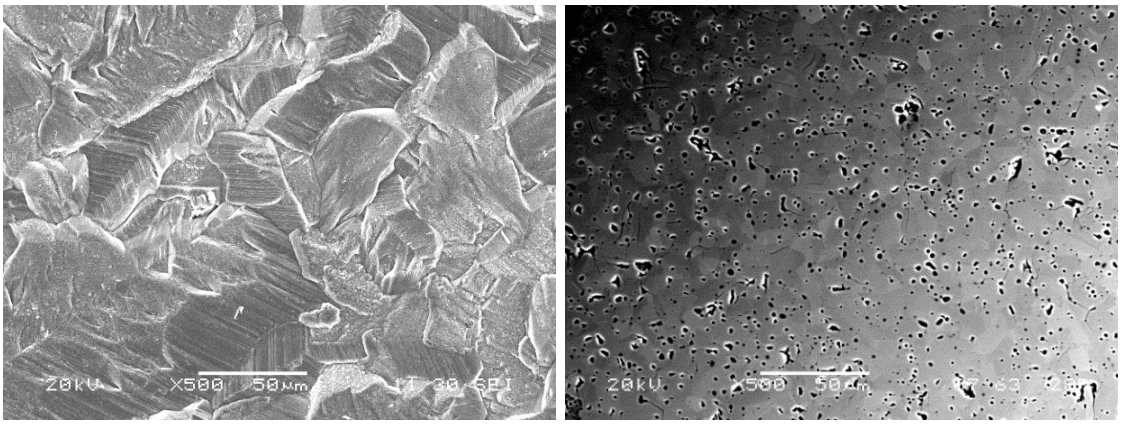

(a) *(b)*

Figure 6.3: *SEM images of Magnéli phases tablets with 2.5%wt binder prepared with(a) 2-Step and (b) 1-Step process [137].*

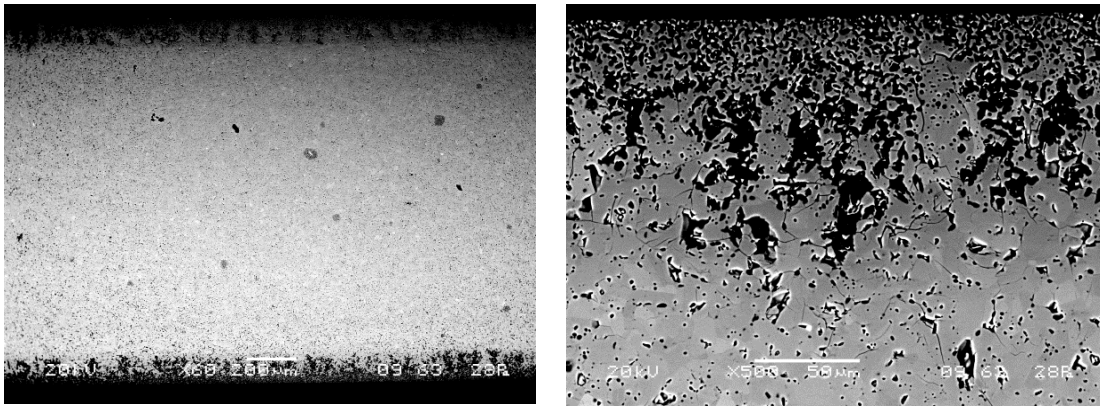

(a) *(b)*

Tablets with 2.5%wt binder – 1-Step preparation process[137]

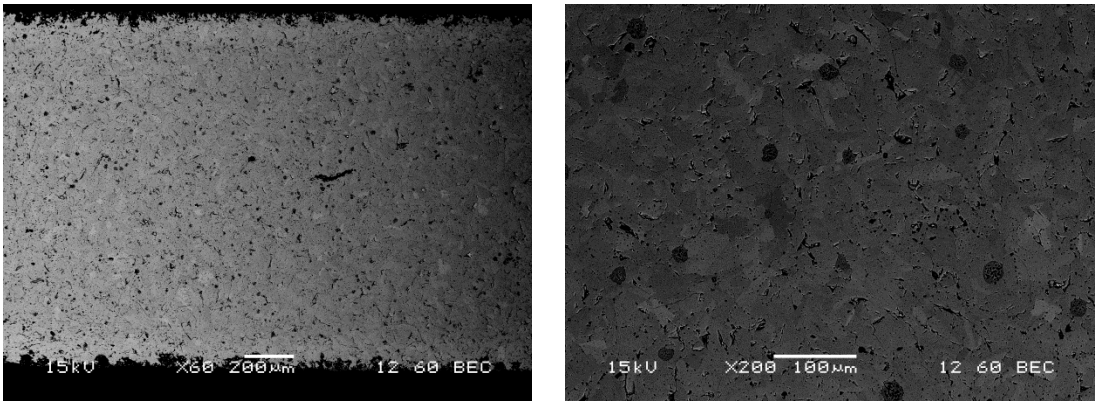

(c) *(d)*

Tablets with 5%wt binder – 1-Step preparation process[137]

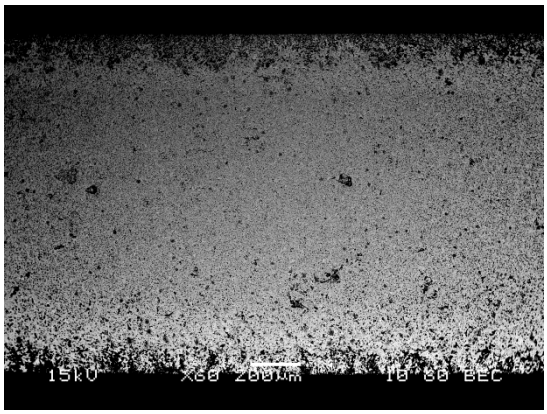

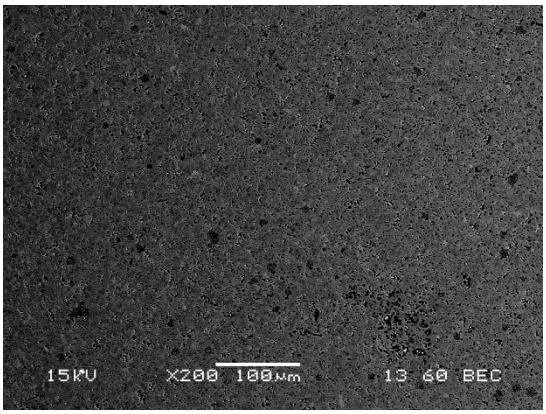

(e) *(f)*

Tablets with 7.5%wt binder – 1-Step preparation process[137]

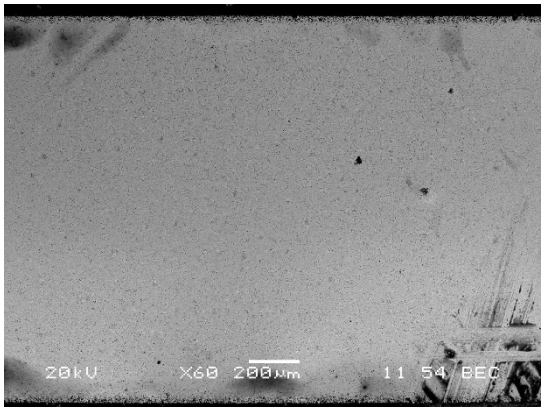

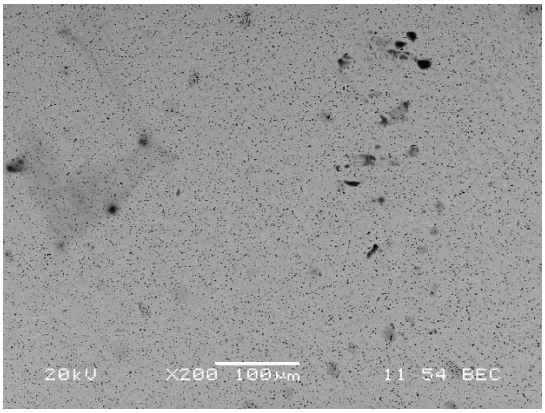

(g) *(h)*

Tablets with 10%wt binder – 1-Step preparation process

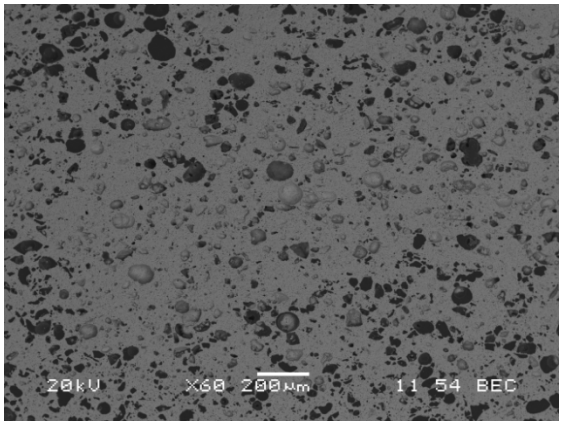

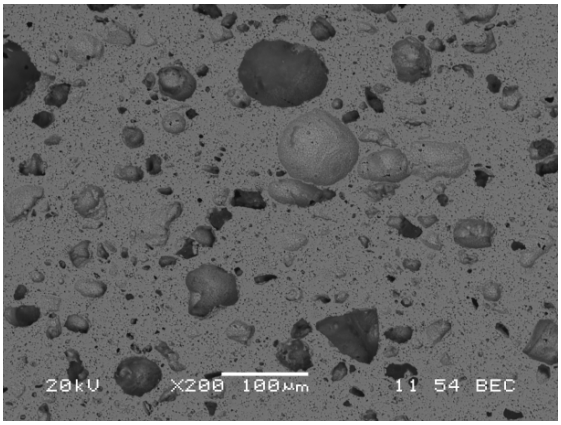

(i) *(j)*

Tablets with 20%wt binder – 1-Step preparation process with low heating rate

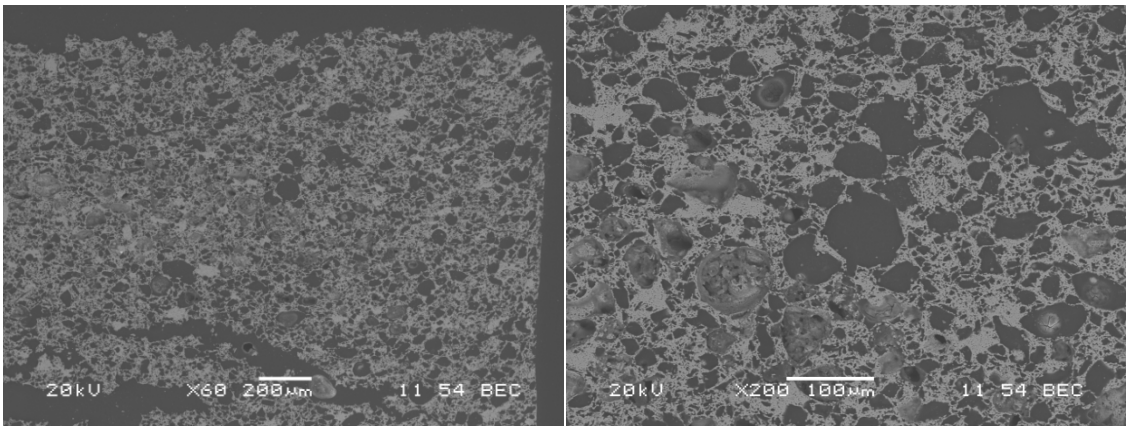

(k) *(l)*

Tablets with 20%wt binder – 1-Step preparation process with low heating rate

Figure 6.4: *SEM images of the Magnéli phases tablets prepared with 1-Step process with (a, b)2.5, (c, d) 5, (e, f) 7.5, (g, h) 10, (i, j) 20 and (k, l) 50%wt binder.*

The cross-section images show a difference in the porosity between the core and the surface of the tablets containing 2.5, 5, 7.5 and 10wt% binder. *Figure 6.5* offers higher magnification close to the surface and this difference is clearer.

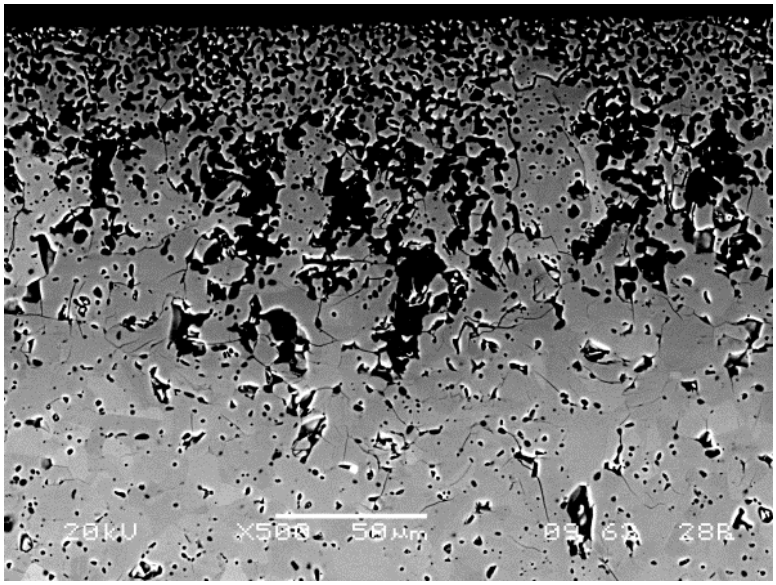

(a)

Tablet with 2.5%wt binder – 1-Step preparation process[137]

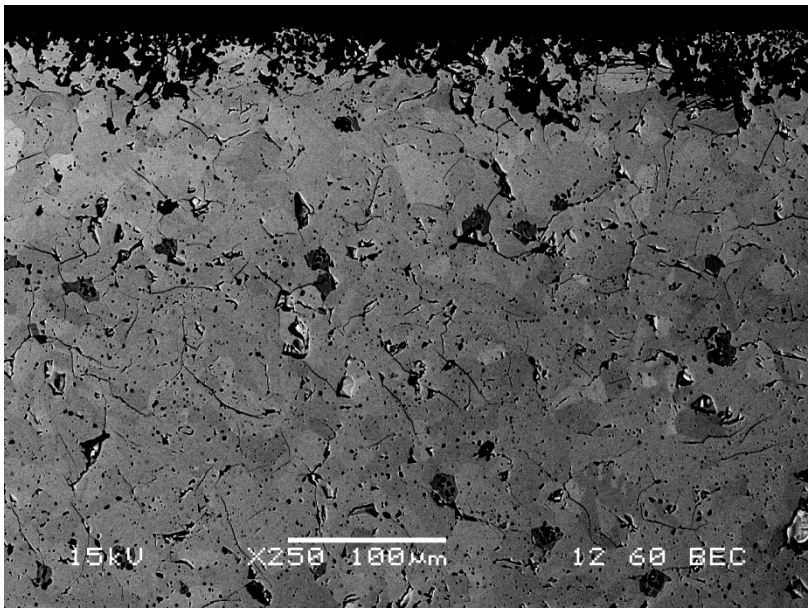

(b)

Tablet with 5%wt binder – 1-Step preparation process[137]

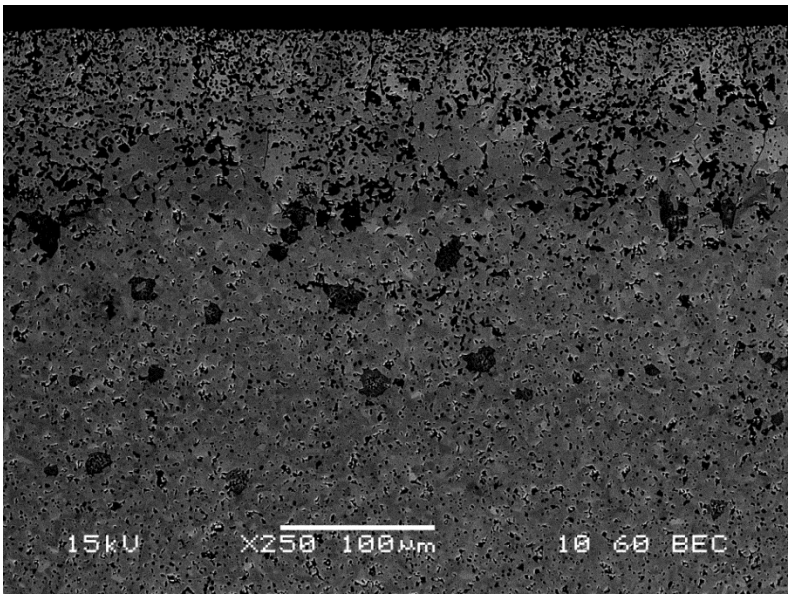

(c)

Tablets with 7.5%wt binder – 1-Step preparation process[137]

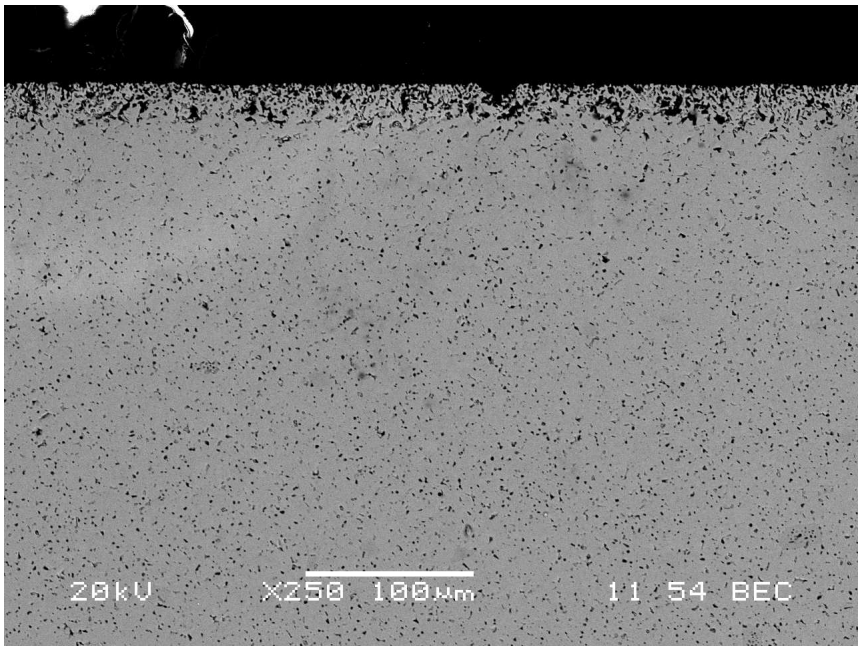

(d)

Tablets with 10%wt binder – 1-Step preparation process

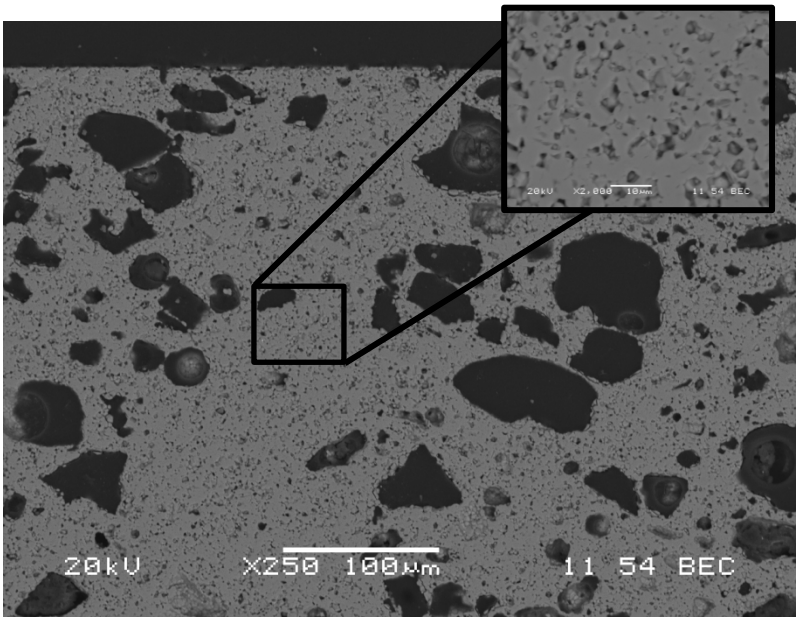

(e)

Tablets with 20%wt binder – 1-Step preparation process with low heating rate

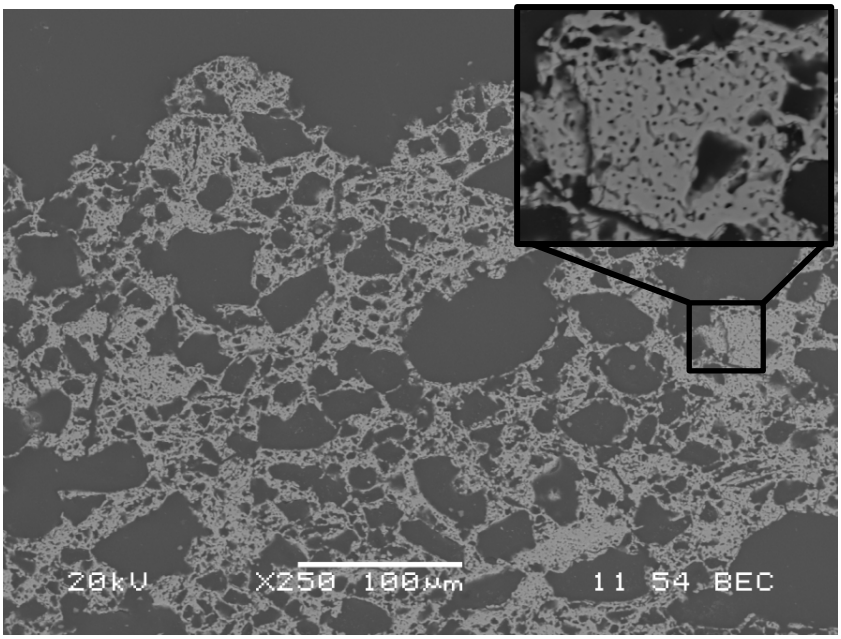

(f)

Tablets with 20%wt binder – 1-Step preparation process with low heating rate

Figure 6.5: *SEM images of the Magnéli phases tablets prepared with 1-Step process with (a)2.5, (b) 5,(c) 7.5, (d) 10 (e), (e) 20 and (f) 50%wt binder focused close to the surface.*

Table 6.3 compares the grain size, pore size and the surface area to volume ratio. These parameters were determined using the ImageJ software on SEM images. Particularly for the 20 and 50 wt% binder samples the determination of the pore size was difficult, due to larger size porous (blisters) created by gas release during de-binding [138, 139].

Table 6.3: Grain size and porosity of wt% binder tablets

Batches No	wt% binder	Grain size (µm)	Pores size (µm)	Surface area to volume ratio (μm^{-1})
2-Step dense samples	2.5	98.94±53.69	-	0.02
1	2.5	13.69±3.43	1.04±0.08	0.08
2	5	19.66±7.34	2.06±1.05	0.08
3	7.5	4.72±1.76	2.36±0.52	0.12
4	10	5.77±1.06	1.71±0.11	0.37
5b	20	3.42±0.73	-	-
6b	50	2.13±0.57	-	-

The grain size of the 2-Step dense tablets is also presented in this table as a reference. The grain size of the samples with 2.5%wt binder prepared with the 2-Step and the 1-Step preparation method are 98.94μm and 13.69μm respectively. The larger grain size is associated with the 2-step process as a result of the material being subjected to heat treatment at 1300°C twice. An additional conclusion was that as the content of binder increases the grain size decreases significantly, even though the heating treatment was the same, up to 1300°C, for all the batches. Pores in a material are essentially defects in the structure and according to the Zener pinning effect [140], if they are present in a high enough proportion, they prevent the grain growth. Furthermore, due to an increased pore density close to the surface, the surface area to volume ratio increases for the tablets containing 2.5, 5, 7.5 and 10wt% binder, which is optimal for use as electrodes. However, the tablets containing 20 and 50wt% binder, even though they have in total higher porosity, do not exhibit gradual porosity towards the surface. Further study is needed in order to understand the de-binding mechanism that causes the increased surface porosity.

Having linked the Magnéli phases to the electrical properties, using XRD, Impedance Spectroscopy and linearity measurements on the dense samples, XRD measurements were conducted to determine the phases present in the porous samples and compare them with the dense samples. *Figure 6.6* presents the XRD data of all the batches of porous samples and of the dense samples as a reference. Based on the XRD spectra, Magnéli phases are present in all the samples. A difference is that the content of TiO_2 was smaller as the samples became more porous. In addition, the presence of Ti_4O_7 (the most conductive phase) was more clear (16.8°, 20.7°, 23.5°). In porous samples electrical measurements are not representative, because of humidity trapped in the pores and because of the electrode paste diffusing through the pores in the sample during the drying and the firing stages. Finally, both the XRD and the SEM confirmed that there was not a second phase created during the heating treatment due to the burning of the binder and the carbon black powder present.

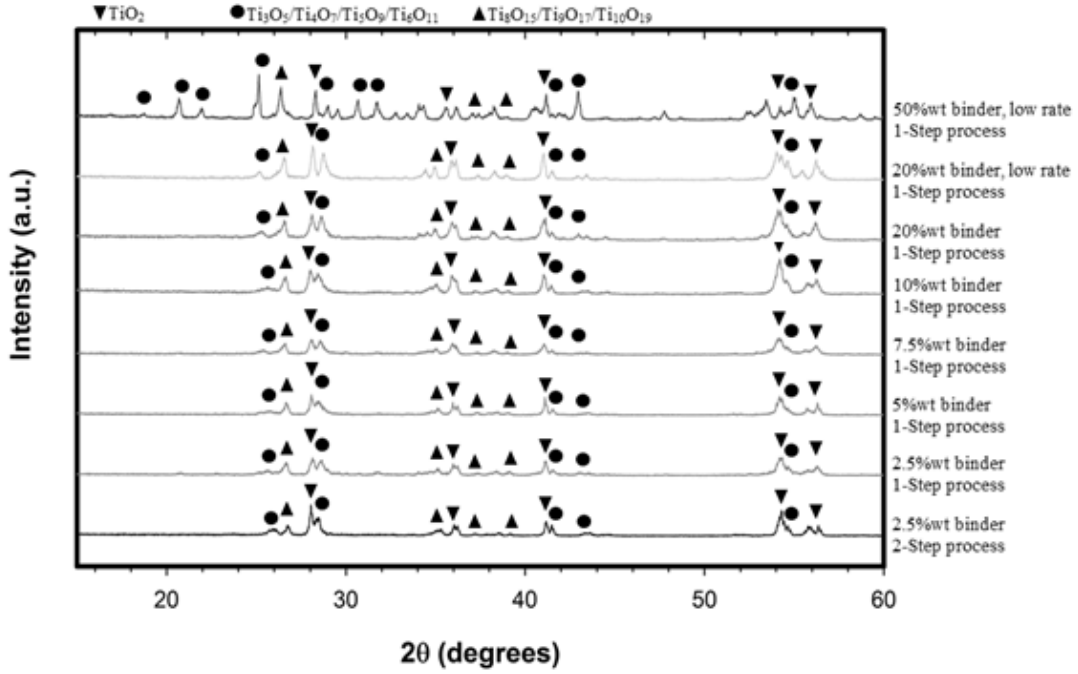

Figure 6.6: *The XRD patterns for all the batches with various percentages of binder*

6.2 Development and characterisation of porous ceramic fibres

After achieving promising results with the bulk tablets, the same approach was attempted to create porous fibres during the visit in EMPA. The increased porosity was likely to affect the reduction process, since it is a diffusion driven process, therefore further optimization of the reduction parameters was necessary. In the following two sections the development and the characterisation of fibre samples is presented.

6.2.2 Development of porous ceramic fibres

For the production of Magnéli phases porous fibres seven different feedstocks were prepared, five of them containing various percentages of a thermoplastic binder, whereas in the others one part of the binder was replaced with paraffin. The description and function of the materials used are listed in Table 6.4.

Table 6.4: Description and function of the materials used in the feedstock preparation

Material	Function	Product details
Rutile TiO_2	Primary material	PI-KEM, 99.5%, 0.3 μm particle size, UK
Low density polyethylene (LDPE)	Thermoplastic binder	Lacqtene Elf Atochem S. A., Switzerland
Stearic acid	Surfactant	Sigma-Aldrich GmbH, Switzerland
Paraffinwax	Pore formers	Bindemittel org, Switzerland

The feedstocks were prepared using a high-shear mixer (HAAKE PolyLab Mixer, Rheomix 600, Thermo Scientific, Karlsruhe, Germany). A higher and a smaller volume chamber were used, having total volumes of $70cm^3$ and $300cm^3$ respectively. The volume of the feedstocks was calculated to fill 70% of the chamber volume. To make sure the feedstocks were homogeneous, the mixing was carried out in two steps. All of the feedstock was removed from the chamber and the chamber was cleaned after the first mixing and it was fed again for the second mixing. The feedstock with the higher content of TiO_2 was prepared first in two mixing steps and then this feedstock was also used to prepare the lower TiO_2 content feedstocks with a single mixing. The feedstocks prepared are shown in Table 6.5 and they were chosen to approximately match the batches of porous bulk samples prepared with 2.5, 5, 7.5, 10, 20 and 50%wt of binder.

Table 6.5: Feedstocks compositions

Feedstocks	Description
54v% TiO_2	54v% TiO_2 + 46v% st. acid+LDPE
50v% TiO_2	50v% TiO_2 + 50v% st. acid+LDPE
45v% TiO_2	45v% TiO_2 + 55v% st. acid+LDPE
40v% TiO_2	40v% TiO_2 + 60v% st. acid+LDPE
20v% TiO_2	20v% TiO_2 + 80v% st. acid+LDPE
40v% TiO_2 (LDPE+Paraffin)	40v% TiO_2 + 60v% st. acid + (80v%LDPE+20v%Paraffin)

The first mixing of the 54v%TiO_2 feedstock occurred in the high volume chamber at 150°C with a constant roller speed of 10rpm. *Figure 6.7* shows the torque of the rollers as a function of time. After reaching a steady torque for

30min the chamber was emptied and cleaned to make sure no ceramic powder was left unmixed. The second mixing of the 54v% TiO_2, 40v%TiO_2 and 20v%TiO_2 feedstock, after adding the proper amount of LDPE, took place in the high volume chamber at 100, 90 and 50°C respectively with a steady roller speed of 10rpm. *Figure 6.8* shows all three second mixing curves.

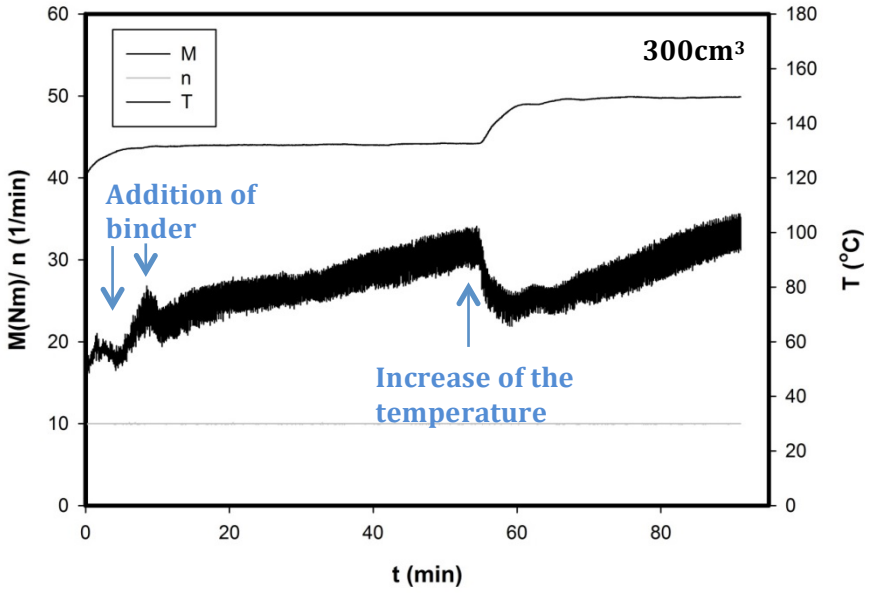

Figure 6.7: *First mixing curve of the 54v% TiO_2 that shows the torque, the temperature and the rotation speed as a function of time*

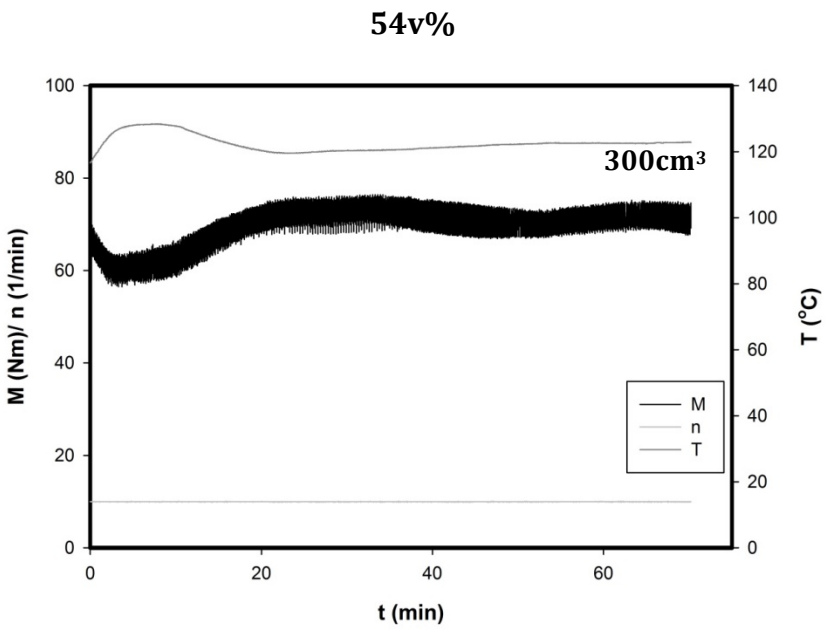

(a)

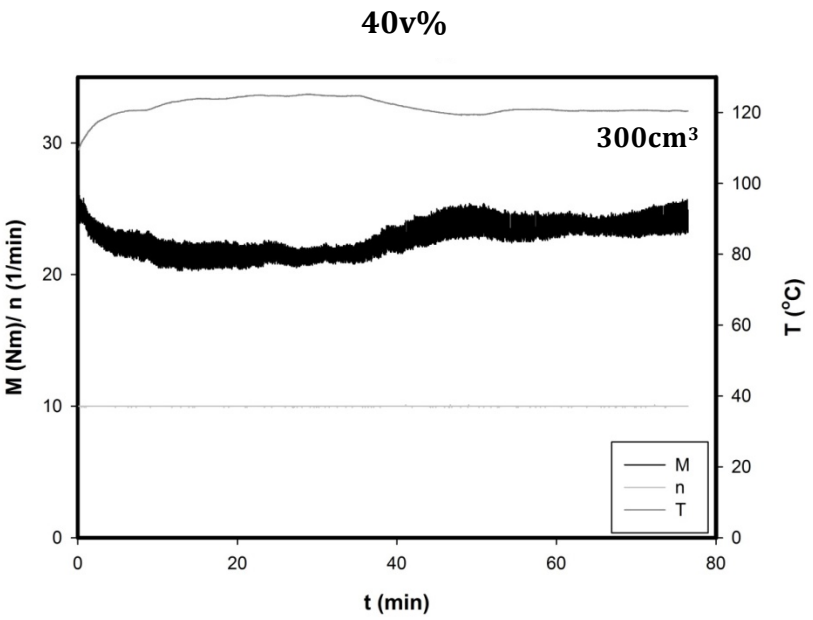

(b)

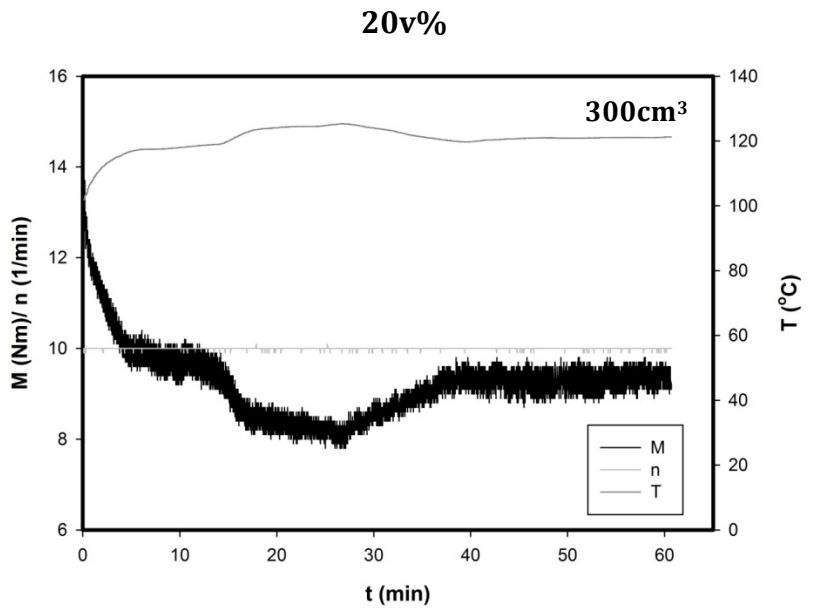

(c)

Figure 6.8: *Second mixing curves for (a) 54v%TiO_2, (b) 40v%TiO_2 and (c) 20v%TiO_2 that shows the torque, the temperature and the rotation speed as a function of time*

Following the same procedure, *Figure 6.9* shows the mixing curves for the 50v% TiO_2 and the 45v% TiO_2, although for these feedstocks the small volume chamber was used.

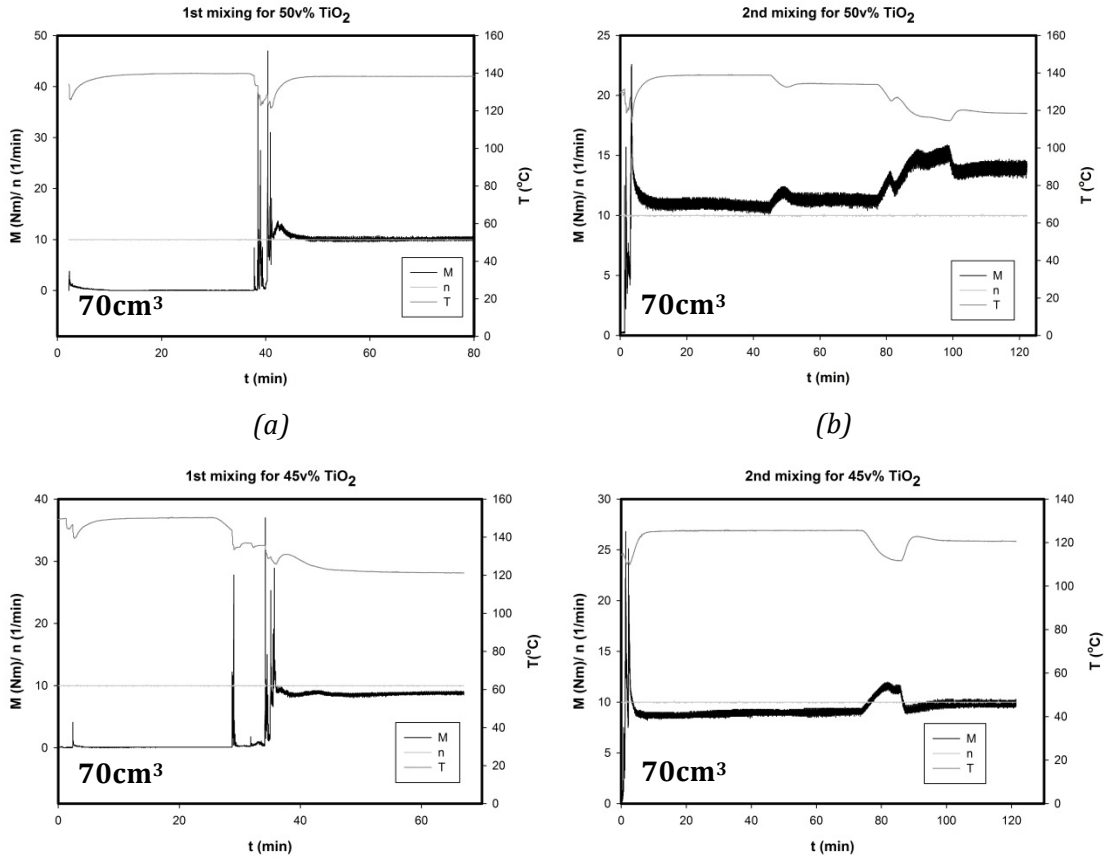

Figure 6.9: *Mixing curves for (a & b) the 50v%TiO_2 and (c & d) the 45v%TiO_2, that show the torque, the temperature and the rotation as a function of time*

In the case of the feedstock with the paraffin, the small volume chamber was used again using part of the 40v%TiO_2 feedstock. *Figure 6.10* shows the mixing curve.

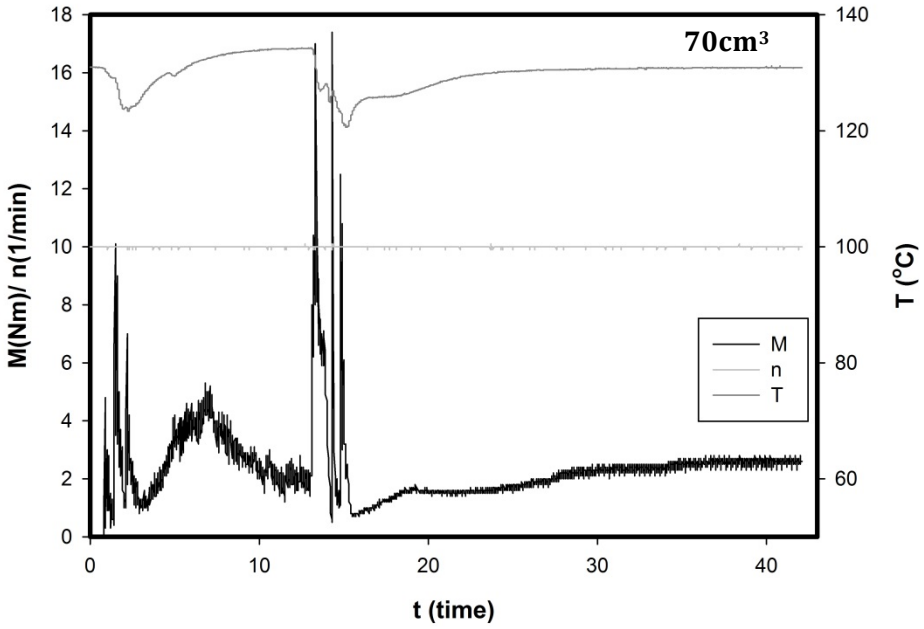

Figure 6.10: *Mixing curve for the 40v%TiO_2 (LDPE+Paraffin) that shows the torque, the temperature and the rotation speed as a function of time*

As shown in *Figure 6.8, 6.9 and 6.10* the mixing stopped after 20min of a steady torque. A steady torque ensures a homogeneously mixed feedstock. Table 6.6 summarizes the torque values for all feedstocks that is an indication of the viscosity of the feedstocks, when comparing the same volume chambers.

Table 6.6: Second mixing torque for all feedstocks

Feedstock	**Torque (Nm)**	**Volume chamber (cm^3)**
54v% TiO_2	72	300
40v% TiO_2	24	300
20v% TiO_2	9.5	300
50v% TiO_2	13.9	70
45v% TiO_2	9.9	70
40v% TiO_2 (LDPE+Paraffin)	2.5	70

The fibres were extruded using a capillary rheometer (RH7-2, Malvern) with a die of Ø 500µm. The parameters that influence the extrusion are the shear rate and the temperature of the barrel. In the case of an extrusion temperature that is too low the feedstock is not homogeneously melted and the flow is not

continuous, the result can be seen in *Figure 6.11a*. In the case of an extrusion temperature that is too high the feedstock is attached on the walls of the barrel causing a non-continuous movement of the piston and the result is inhomogeneous diameter of the fibres, as shown in *Figure 6.11b*.

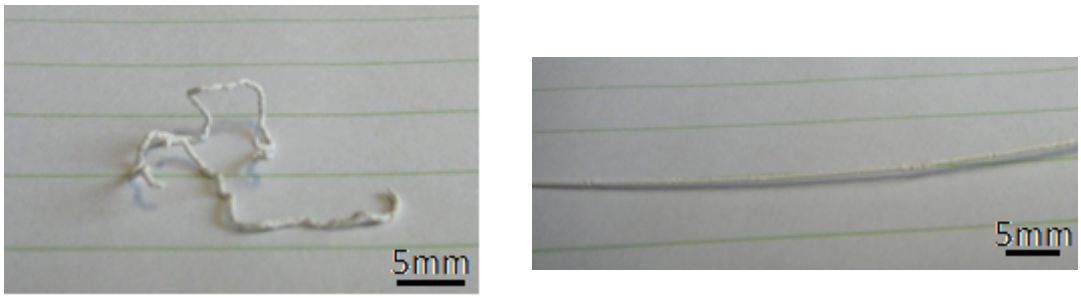

(a) *(b)*

Figure 6.11: *Unsuccessful extrusion in the case of (a) too low a temperature and (b)too high a temperature*

Table 6.7 summarizes the optimal extrusion parameters in order to have a constant flow of fibres having a uniform diameter.

Tabl 6.7: Extrusion parameters for all feedstocks

Feedstocks	**Shear rate (l/s)**	**Temperature (°C)**
54v% TiO_2	1434	140
50v% TiO_2	1434	130
45v% TiO_2	1434	120
40v% TiO_2	1434	98
20v% TiO_2	294	102
40v% TiO_2 (LDPE+Paraffin)	294	100

Taking into consideration the de-binding and reduction profile that achieved the best results on the tablets in terms of deformation and porosity, the same profile was also followed for the fibres. To ensure that the thermoplastic binder does not react with the carbon black powder during reduction, the de-binding phase was undertaken in a chamber furnace following the de-binding profile in *Figure 6.12a*. The carbo-thermal reduction took place in a tubular furnace in the

presence of carbon black powder under constant Argon flow following the profile in *Figure 6.12b*.

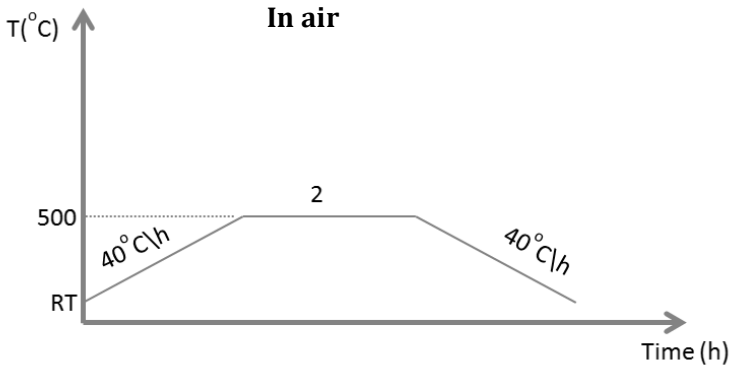

(a)

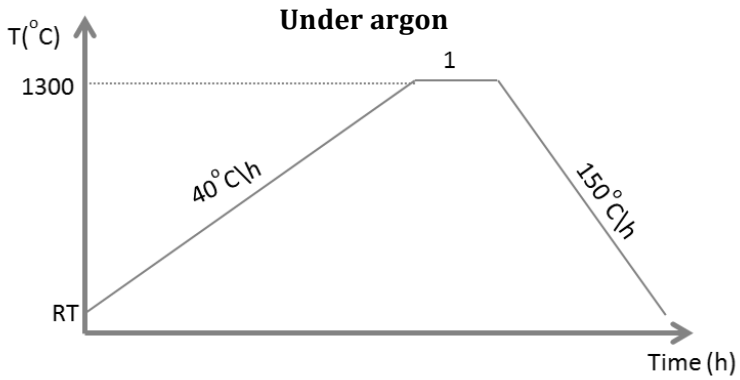

(b)

Figure 6.12: *(a) De-binding profile and (b) reduction profile*

6.2.2 Physical properties and structural characterisation of porous ceramic fibres

Initially, in order to ensure that the feedstocks were homogeneous and their density was the same as calculated from the quantities of the material used, it was measured using a helium pycnometer (AccuPyc II, micromeritics). *Figure 6.13* summarizes the densities of all feedstocks and shows that the densities measured with the helium pycnometer match the calculations.

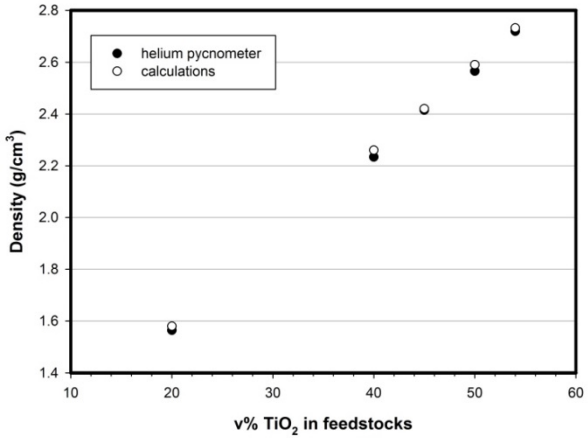

Figre 6.13: *Density calculations and measurements using a helium pycnometer for all feedstocks*

In feedstocks with increased content of binder the die swell effect is expected to be greater. The die swell effect is related to the relaxation of the binder and it is expressed by the ratio of the die diameter and the diameter of the extruded fibres [141]. Table 6.8 shows the green fibres diameter and presents the die swell effects, confirming that as the percentage of binder increased the die swell effect was greater.

Table 6.8: Green fibres diameter and die swell effect

Feedstocks	Green fibre Ø (µm)	Die swell (%)
54v% TiO_2	520	4
50v% TiO_2	530	6
45v% TiO_2	560	12
40v% TiO_2	570	14
20v% TiO_2	620	24
40v% TiO_2 (LDPE+Paraffin)	500	0

The small scale of the fibres would result in inaccurate density measurements with the helium pycnometer, therefore SEM images aided in the evaluation of the density and porosity of the fibres, as well as the effect of the various percentages of binder and the pore formers on the grain size, porosity and shrinkage of the fibres after the de-binding and the reduction.

Initially, the feedstocks prepared were the 54v%, 40v% and 20v% TiO_2. After de-binding the 20v% TiO_2 fibres did not retain their shape, so it was not possible to continue with their preparation. *Figure 6.14* shows SEM images after de-binding for the 54v% and 40v% TiO_2 fibres (see de-binding profile in *Figure 6.12a*). The 54v% TiO_2 fibres maintained their circular cross-section having a diameter of 490μm (5.7% shrinkage) and the binder burned out uniformly (*Figure 6.14a*). On the other hand the 40v% TiO_2 fibres did not maintain their circular cross-section, since the burning out of the binder created a central hole resulting in an oval cross-section (*Figure 6.14c,d*). However, they maintained their strength and it was possible to handle them, therefore the fibres were subjected to the reduction process.

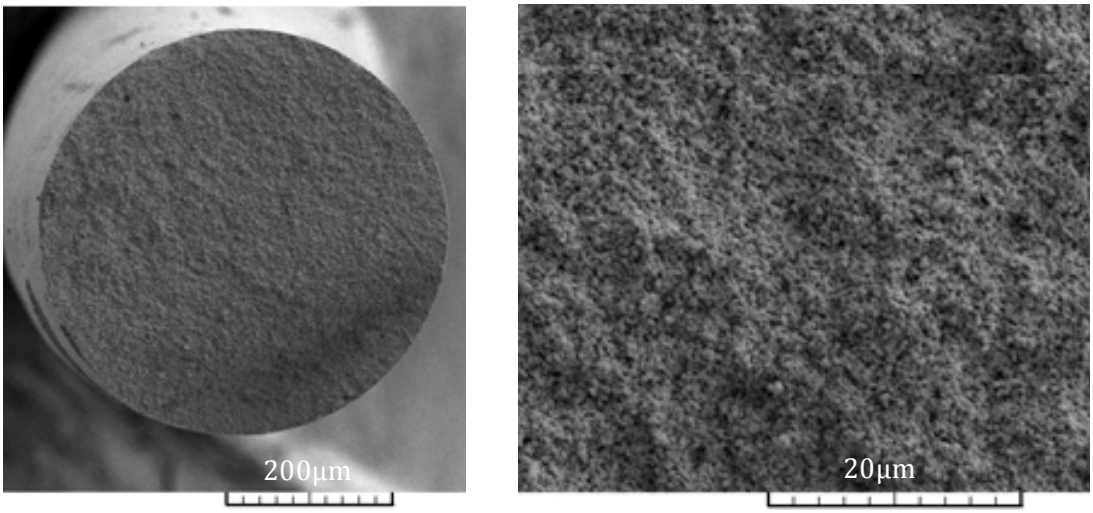

(a) *(b)*

54v% TiO_2 fibres, green after reduction

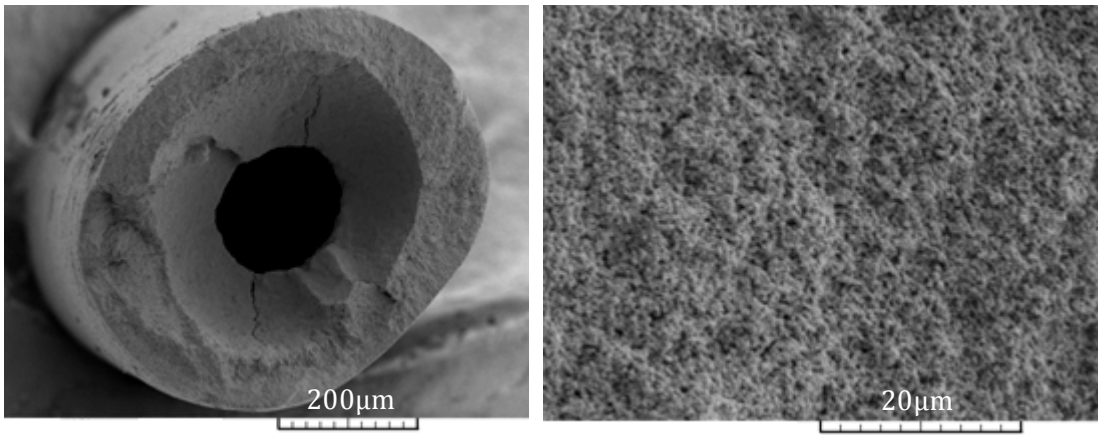

(c) *(d)*

40v% TiO_2 fibres, green after reduction

Figure 6.14: *SEM images after de-binding for the (a, b) 54v% and (c, d)40v% TiO_2 fibres*

Figure 6.15 shows the 54v% TiO_2 fibres after reduction. Their cross-section was circular and their diameter was 410µm (a further 16.3% shrinkage). There was a difference in the grain size and the porosity between the core and the surface. The porosity increased close to the surface as was also seen in the bulk tablets (*Figure 6.3*).

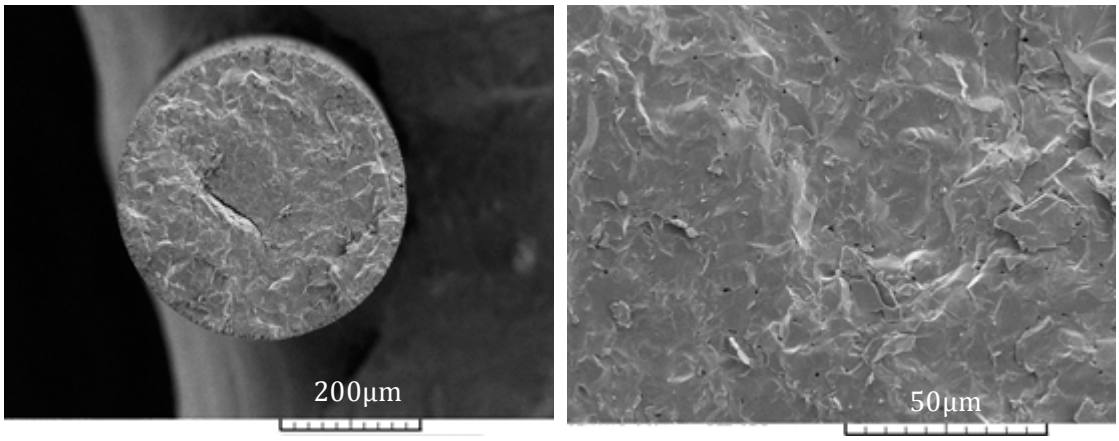

(a) *(b)*

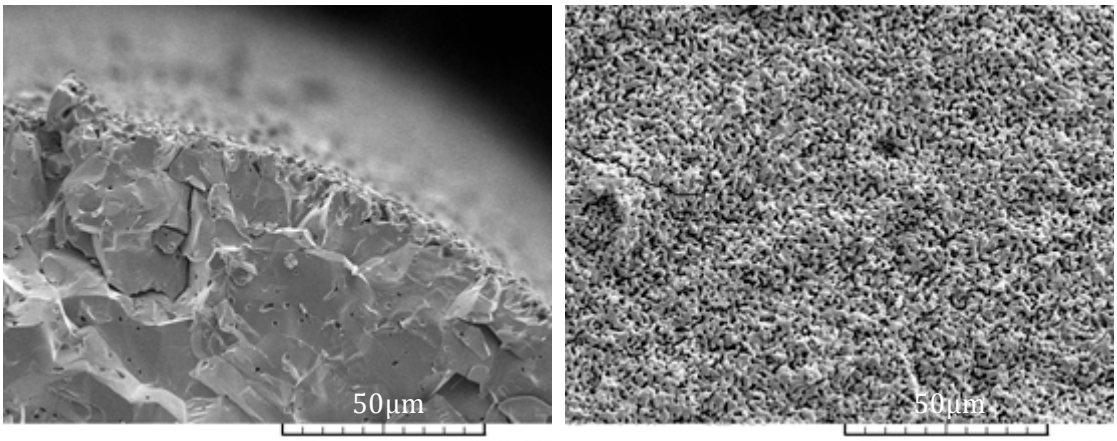

(c) *(d)*

Figure 6.15: *(a, b, c, d) SEM images of the 54v% TiO_2 fibres after reduction*

The 54v% TiO_2 feedstock was also used for the manufacturing of dense fibres following a 2-Step preparation method as described in section 5.1. *Figure 6.16* shows the effect of the 1 and 2-Step preparation on the grain size and the porosity. The combined de-binding and reducing process has an effect on surface porosity, similar to the effect in the tables. Moreover, the fibres exhibit a gradual grain size from the core to the surface and the same will be observed for the fibres with increased content of binder. The determination of the grain size due to this variability cannot be achieved with accuracy, however Table 6.9 offers an estimate of the grain size for the 54v% TiO_2 fibres prepared with the two different methods. As with the tablets the lack of a second heating treatment has a significant effect on the grain size that is 7.5-16.69µm and 100µm for the fibres prepared with a 1-Step and 2-Step preparation respectively.

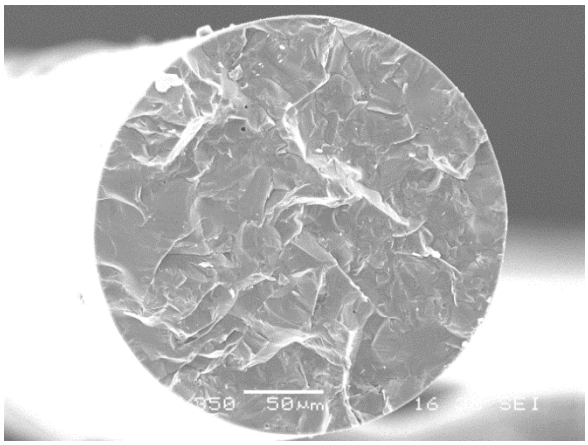

(a)

Magnéli phases fibres prepared with 2-Step preparation

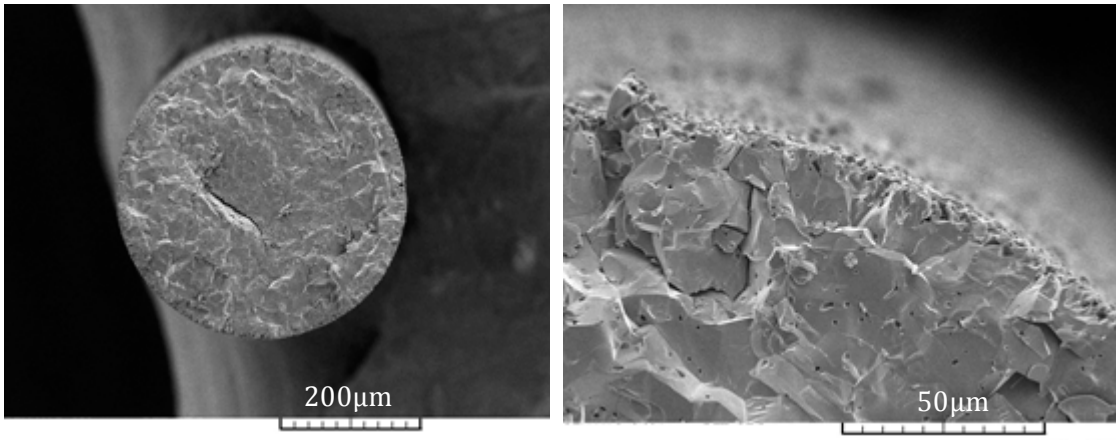

(b) *(c)*

Magnéli phases fibres prepared with 1-Step preparation

Figure 6.16: *SEM images of the Magnéli phases fibres prepared with the 54v% TiO_2 feedstock with the (a) 1-Step preparation and (b, c) with the 2-Step preparation method*

Table 6.9: Grain size for the Magnéli phases fibres prepared with the 54v% TiO_2 feedstock with the 1-Step and 2-Step preparation method

Magnéli phases using 54v% TiO_2 feedstock	**Core grain size (µm)**	**Surface grain size (µm)**
2-Step preparation	100	100
1-Step preparation	7.5	16.69

The Magnéli phases fibres made using the 40v% TiO_2 feedstock due to the non-uniform burn out of the binder during de-binding were more like hollow fibres,

since the inner hole was better shaped after the reduction as shown in *Figure 6.17*.

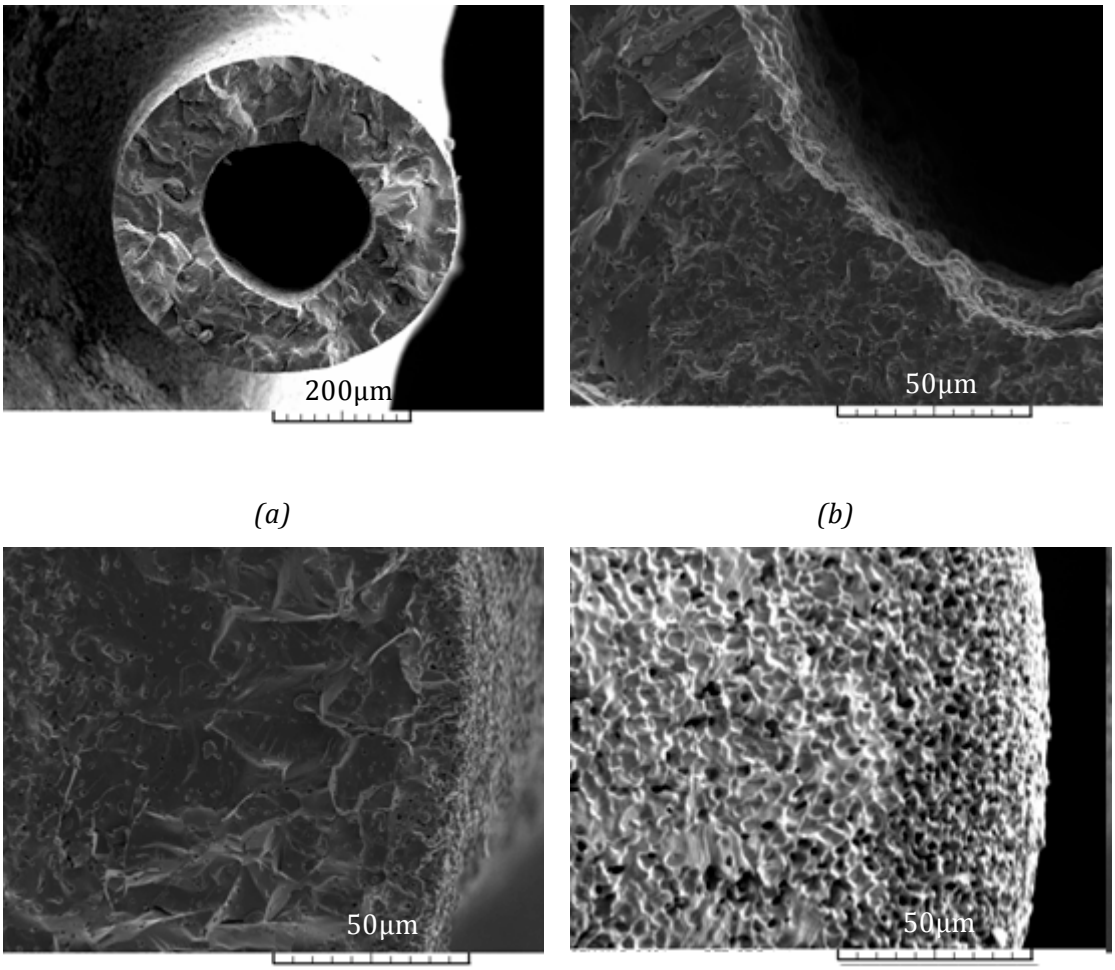

Fiure 6.17: *(a, b, c, d) SEM images of the Magnéli phases fibres prepared with the 40v% TiO_2 feedstock*

It was also observed that the grain size was larger in the core and smaller in the surface (core grain size: ~2.71µm, surface grain size: ~14.57µm) and the porosity was again higher closer the surface (see *Figure 6.17d*).

In an effort to achieve the lowest percentage of the binder in the feedstock that offers a uniform de-binding. The 50v% and 45v% TiO_2 feedstocks were prepared and SEM images were taken after de-binding (*Figure 6.18*) and reduction (*Figure 6.19*).

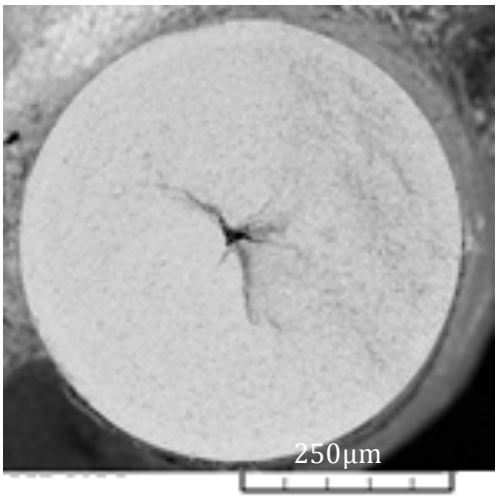

(a)

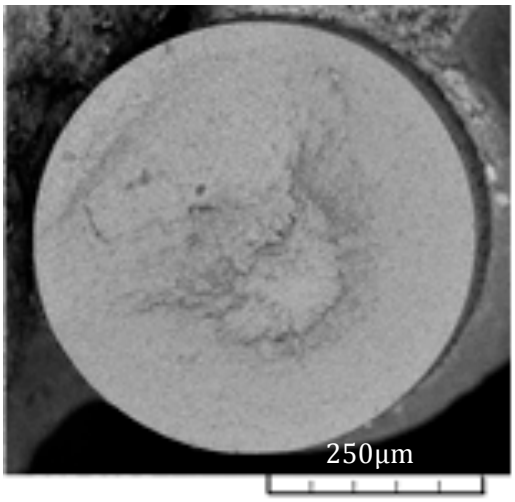

(b)

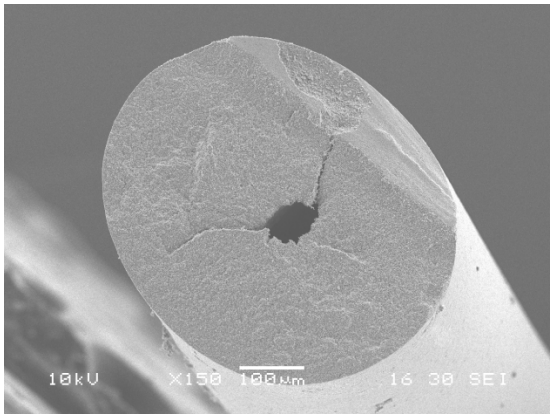

(c)

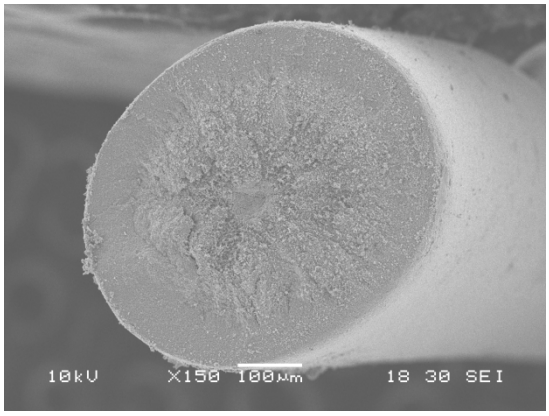

(d)

Figure 6.18: *SEM images of the (a, b) 50v% and (c, d) 45v% TiO_2 fibres after de-binding*

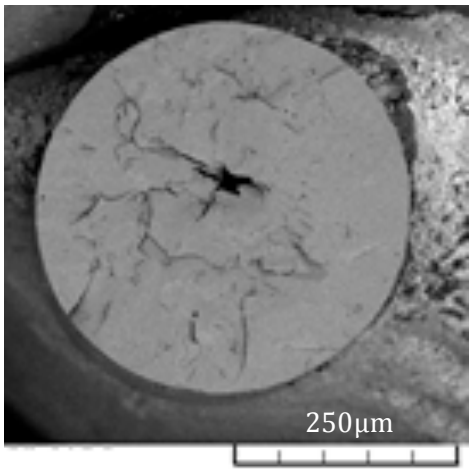

(a)

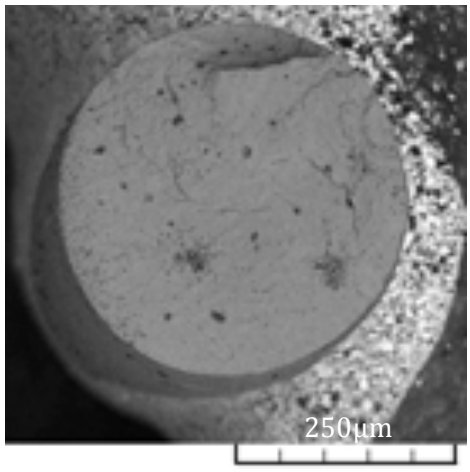

(b)

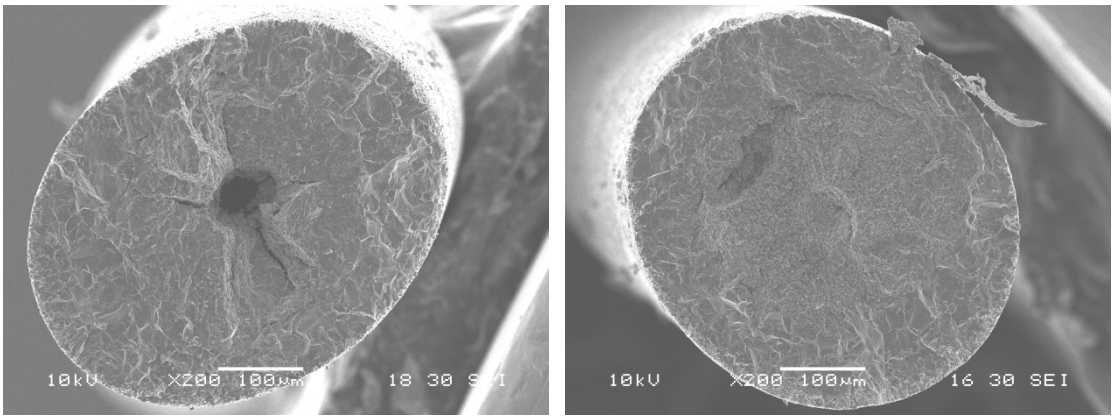

(c) *(d)*

Figure 6.19: *SEM images of the Magnéli phases fibres prepared with (a, b) the 50v% and (c, d) the 45v% TiO_2 feedstocks*

Based on the SEM images after de-binding and after the reduction step the outcome was not consistent. The binder was not burning out homogeneously and so it was not possible to produce uniform fibres and ensure consistent mechanical properties.

Finally, in order to avoid the non-uniform burning out of the binder, a new feedstock was prepared in which part of the binder was replaced with paraffin as described in section 6.1.2. The paraffin provides further stiffness to the green bodies, so that it was easier to handle, maintain their shape and prevent the formation of hollow fibres [142]. The green fibres after de-binding were put on a TiO_2 powder bed at 150°C over night to diffuse the paraffin out of the fibres. The 40v% TiO_2 was chosen to check the performance of the paraffin in the feedstock. *Figure 6.20* shows the SEM images of the 40v% TiO_2 (LDPE+Paraffin) after de-binding and after reduction, whereas *Figure 6.21* compares the fibres using the 40v% TiO_2 feedstock with and without paraffin.

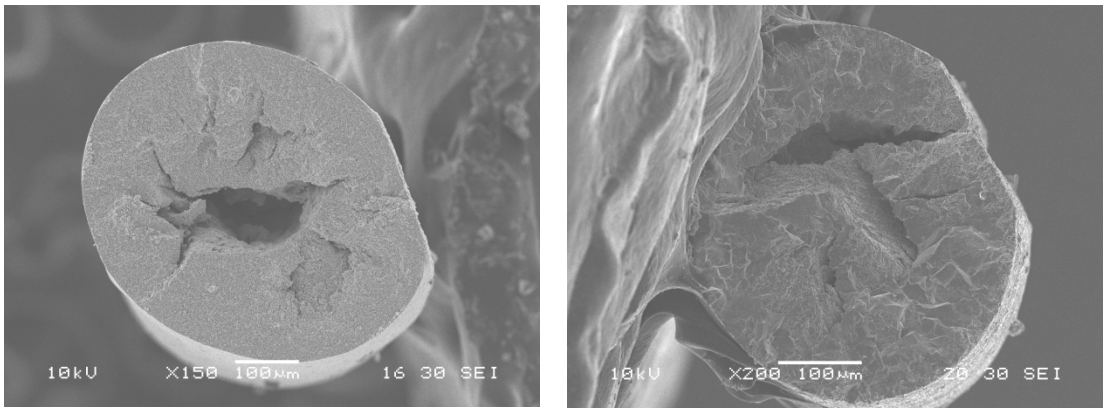

(a) *(b)*

Figure 6.20: *SEM images of the 40v% TiO_2 (LDPE+Paraffin) fibres (a) after de-binding and (b) after reduction*

After de-binding

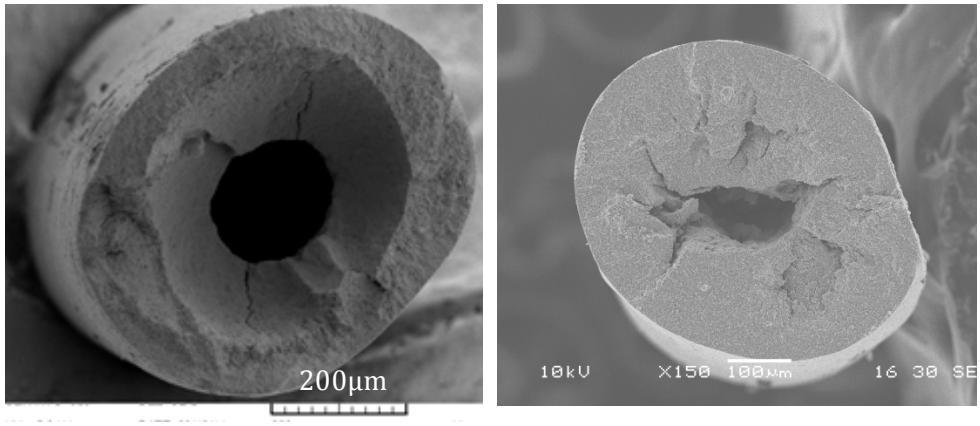

(a) *(b)*

After reduction

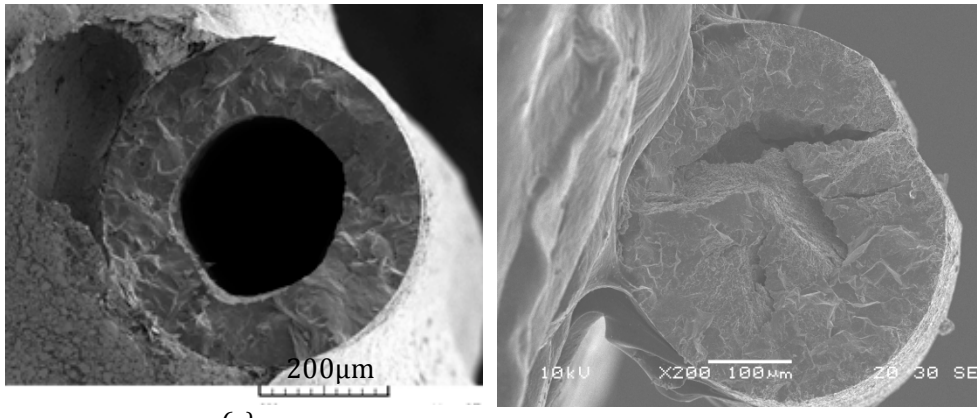

(c) *(d)*

Figure 6.21: *SEM images of 40v% TiO_2 fibres (a, c) without paraffin and (b, d) with paraffin, after de-binding and after reduction*

The paraffin did not improve the properties of the fibres. The burn-out of the binder occurred slightly more homogeneously, however the shape was not

maintained. Further work to optimise the extrusion parameters and preparation of new feedstocks will be discussed in section 9.2 as future work.

6.3 Discussion

The aim of the work presented in the current chapter was the manufacturing of bulk samples and fibres with increased porosity. The initial work focused on manufacturing bulk tablets with an increased percentage of binder, rather than the 2.5wt% that was used for the dense tablets (section 4.1.2). In order to control grain growth and avoid densification of the samples a different heating treatment was followed that included de-binding and reduction at 1300^{o}C in a tubular furnace under constant Argon flow in the presence of carbon black powder; this avoided the use of an additional high temperature heat treatment. Samples were prepared following this 1-Step reduction process containing 2.5, 5, 7.5, 10, 20 and 50wt% of binder. The samples with a binder percentage up to 10wt% exhibited an increased porosity close to the surface, whereas the core is denser. At the same time the grain size was smaller close to the surface due to porosity preventing the grain growth. In total the porosity reached a maximum of 65% for the samples containing 50wt% of binder.

Following the same method, fibres with an increased percentage of binder were manufactured (46, 50, 55, 60, 80v% binder). The binder used for the extrusion of fibres is a thermoplastic and by increasing its percentage in the feedstocks instead of increasing the porosity the result was hollow fibres. However using the same feedstock as for the dense fibres (54v% TiO_2) and following a 1-step reduction method the same effect of increased surface porosity was observed as in the tablets. Differences in the core and surface grain size were also observed (an increase of 122% close to the surface). Further work to achieve higher porosity will take place using pore formers in the feedstock, such as carbon. Additional work to understand the binder burning-out mechanism will also take place using thermo gravimetric analysis.

The cyclic voltammetry on these samples will be presented in chapter 8. The results will be analysed in detail, both for fibres and tablets with a relatively dense core and a highly porous surface. Such a structure is of interest for

electrode applications since the increased surface area will provide more active area to react with the electrolyte, whereas the more dense core will guarantee a good contact with the electrode/wire.

The achievements of the work presented in this chapter can be summarised in the following points:

i. Preparation of bulk tablets with a maximum porosity of ~65% was achieved by using a combined de-binding and reduction process.
ii. Bulk tablets were manufactured having a dense core and increased surface porosity.
iii. Following the same 1-step process fibres with a dense core and increased surface porosity were manufactured.

7. Wear sensor – Integration

Following the manufacturing of dense Magnéli phases materials that meet the requirements (conductivity, hardness, thermal expansion coefficient) for the active material in the wear sensor application and having achieved a strong and ohmic fibre-wire contact, the next step was the integration of the material in a device for the final application. For the successful integration of the sensor it was essential to choose the appropriate soldering glass to guarantee good insulation of the conductive fibre from the steel and good soldering of the fibres in the grooves (see schematic of sensor in *Figure 2.5*). During the testing of the prototypes sensors noise problems and problems with the wire termination had to be solved. The optimized sensor was tested in a grinding machine and the results are presented in section 7.2. The sensors were also placed in a steel mould used in the injection moulding machinery, however the wear rate was slow, so it was not possible to acquire these results within the timescale of the project. Discussion of the results and improvements on the sensor are presented in section 7.3.

7.1 Integration

The working principle of the wear sensor is described in section 2.1.1, where *Figure 2.5* presented the side view of the sensor.

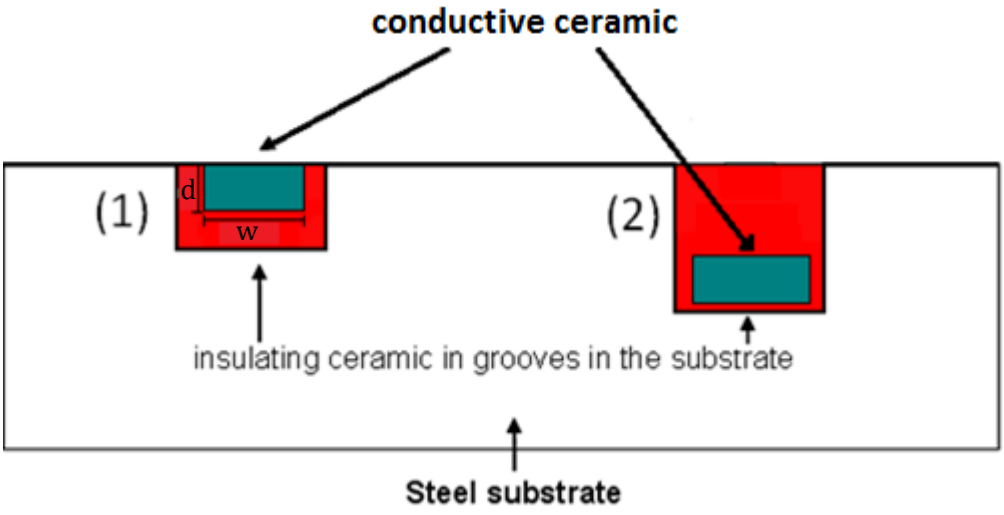

Figure 2.5: *Side view of the sensor showing the placement of the insulating (red) and conducting ceramic (green) in the grooves: (1) sensor element (2) reference element*

Regarding the insulating layer and the ceramic deposition techniques into the grooves of steel, sol-gel processing of ceramics, thermal spray and the use of vitreous enamel have been tested as part of the initial work for the MesMesh project. The University of Bath prepared a series of titanium dioxide (TiO_2) and aluminium oxide (Al_2O_3) gels from low-cost inorganic chemical precursors. The idea was to inject the gel into the grooves in the steel and heat the samples in a furnace at a specific temperature (600°C) to promote the formation and the densification of the ceramic from the gel. It was found that sol-gel presents some processing issues. Although the ceramic particles tend to aggregate, suggesting that sintering and densification can be achieved at a relatively low temperature of 600°C (compared to other techniques used to sinter ceramics, > 1000°C), there was little bonding at the steel-ceramic interface. Shrinkage of the gel during the heat treatment also prevented the channel in the steel from being properly filled. For thermal spray deposition, the precursors (feedstock: solid powder or solution) are vaporised either electrically (plasma) or chemically (combustion) to form a coating on a substrate (steel). The advantage is that the

steel can be kept at room temperature so that oxidation was limited, however the coating will be deposited over the entire steel substrate (unless a mask is used) and will have to be polished off from unwanted areas (outside the channels). Again due to the complexity of the processing, this was not considered suitable.

An alternative approach investigated as part of the PhD involved the use of vitreous (Porcelain) enamel, either as powder or a suspension that was introduced into the channel. Enamel is a glassy material and, depending on its chemical composition, melts at a temperature in the range of 300-800^{o}C. In this case it is possible to use the melting of the glass rather than sintering to fill the grooved steel with an electrical insulator. Melting of the enamel allows the material to flow and fill the channel (see *Figure 2.5* for the red insulating material). Initial results on the use of enamel were encouraging. An enamel based suspension (P4302.015, Kingfisher Blue Onglaze, PotteryCraft) was deposited on a channel (2x2mm) on mild steel substrates and fired at 750-780^{o}C. In addition, a ceramic fibre had been successfully embedded in the enamel in the groove. The cross section image of the steel-enamel-fibre system obtained from Scanning Electron Microscopy (SEM), *Figure 7.1a*, confirmed the enamel coating had bonded well to the steel but lacked homogeneity. This issue can be solved by optimising the firing conditions of the enamel and refining its composition. Error! Reference source not found.*b* shows a SEM high magnification view of the interface steel-enamel, where the bonding between the vitreous matrix and the steel can be better observed. This system (enamel-ceramic fibre) has the potential to fulfil the requirements of the MesMesh project and has the advantage of allowing processing of the ceramic (composite) separately from the glassy component used as filler and insulator.

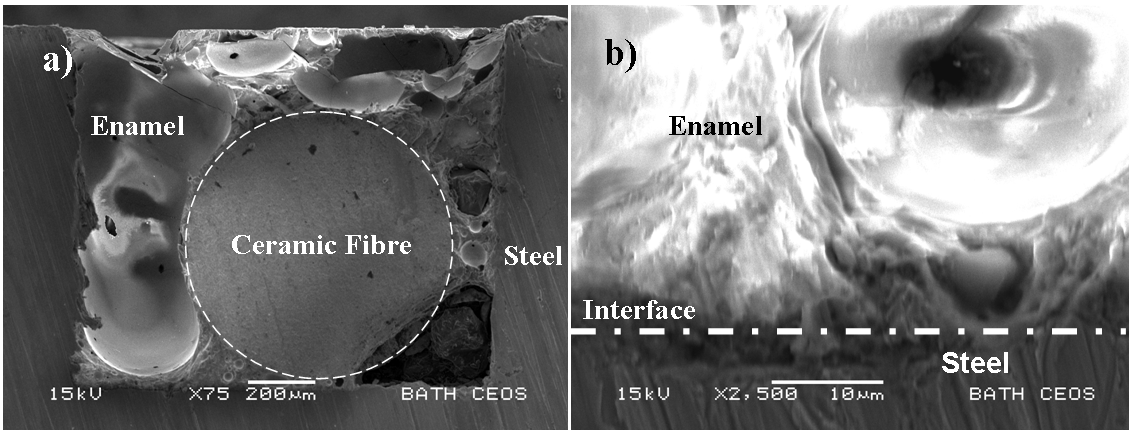

Figure 7.1: *SEM image of the steel-enamel-ceramic fibre system (a) and high magnification SEM image (b) showing the interface between the vitreous enamel and the steel [12]*

The goal of the glassy material used - enamel in the initial tests - is to insulate the ceramic efficiently and bond the ceramic and the steel so they behave in a similar way during operation of the mould without delaminating or cracking. In addition the glassy material needs to be a low melting point glass (up to 550°C), so that the steel does not get oxidised during firing, but has an operating temperature higher than 250°C, a typical operating temperature for injection moulding. Enamel did not meet the requirements therefore a low melting point lead free solder glass based on Bi_2O_3 was chosen. Glasses based on heavy metal oxides such as Bi_2O_3 have wide applications in the field of glass ceramics, layers for optical and electronic devices, thermal and mechanical sensors, reflecting windows, etc [143]. Bismuth oxide cannot be considered as network former due to the small field strength of the Bi^{3+} ion. However in combination with B_2O_3 glass formation is possible in a large compositional range, since B_2O_3 is one of the most common glass formers and with an increase in the concentration of Bi_2O_3, the glass transition temperature (T_g) decreases [143].

The glass that was selected is the SCHOTT low melting lead free solder glass [144], which has the chemical composition and physical properties shown in Table 7.1.

Table 7.1: Chemical composition and physical properties of the SCHOTT solder glass

Chemical composition (wt%)		Physical properties	
Bi_2O_3	>50	**Thermal expansion coefficient**	$10.11x10^{-6}\ K^{-1}$
ZnO	10-50	**Transformation temperature**	365°C
SiO_2	1-10	**Density**	$7.13\ g.cm^{-3}$
B_2O_3	1-10		
Al_2C_3	0.1-1		

Solder glasses, such as the one selected in this work, are used to join glass to other glasses, ceramics or metals without thermally damaging the materials. As with all seals involving glass, adapting the thermal expansions of the components to be joined with solder glass is a necessary prerequisite to achieve stable, tight joints. The coefficient of thermal expansion of the solder glasses should be smaller than the expansion coefficients of the sealing partners by around $0.5\text{-}1.0x10^{-6}K^{-1}$ [145]. The firing conditions for the solder glass are shown in *Figure 7.2*.

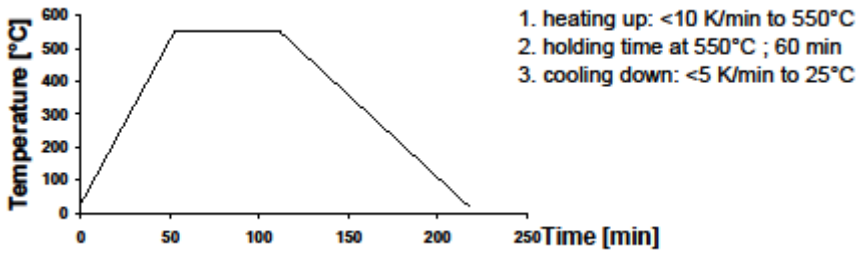

Figure 7.2: *Firing condition of the SCHOTT low melting solder glass [145]*

Initial trials were conducted using steel samples with machined grooves of 2 mm and Magnéli phases bars of 1.5x1 mm, that were cut from the bulk (tablets) samples (*Figure 7.3*).

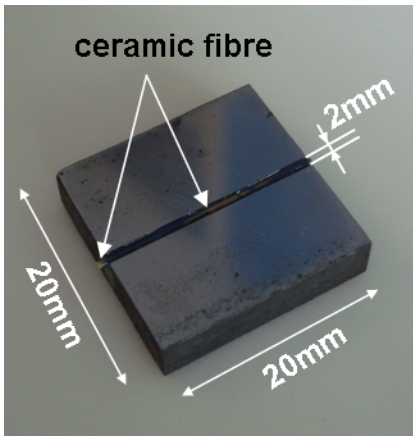

Figure 7.3: *Grooved steel samples used for initial testing to place ceramic fibres into the grooves using a glass*

In order to test the durability of the ceramic/glass/steel system, a grinding test was performed removing approximately 100µm from the surface. *Figure 7.4* shows optical microscope images of the samples after grinding. The images show that the glass joint remains tight and the ceramic is fully covered. Some micro-cracks that are visible on the ceramic surface are probably due to internal stress generated during the reduction process.

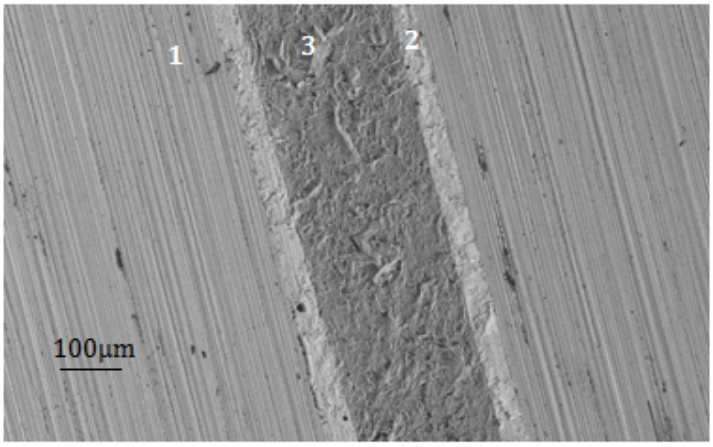

(a)

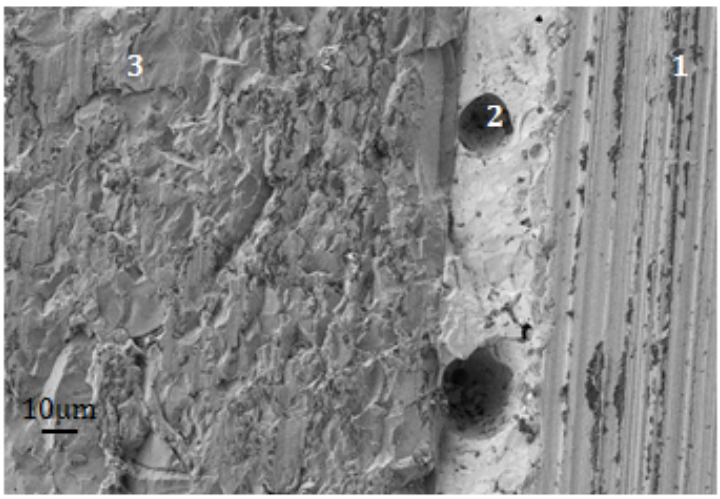

(b)

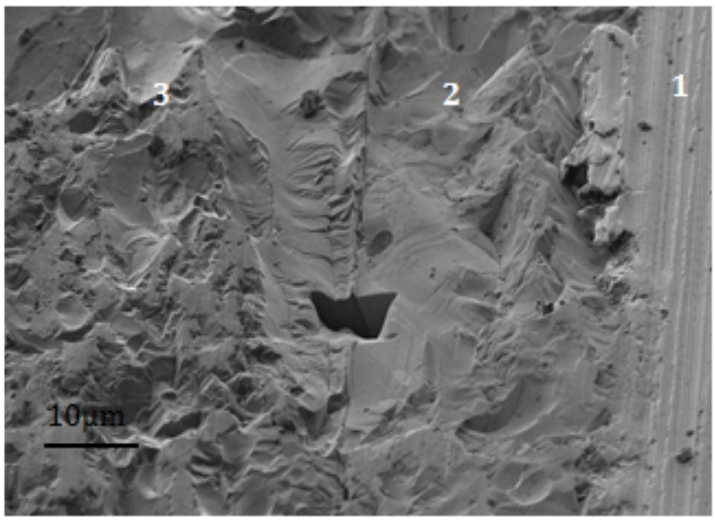

(c)

1: steel, 2: SCHOTT glass, 3: Magnéli phases fibres

Figure 7.4: *Images of the embedded ceramic in the grooves after the grinding test [146]*

The design of the complete sensor with electrical contacts was circular and holes were drilled for the wires to pass through. Various sizes were tested before downsizing to the final sensor dimensions. The first step of the sensor assembly is to achieve a good bond between the silver wires and the fibres to measure resistance (*Figure 7.5a*). The second step is to fill the holes and the grooves with the glass (*Figure 7.5b*) and the final step is to place the fibres and wires through the holes and into the grooves (*Figure 7.5c*).

(a) *(b)* *(c)*

Figure 7.5: *Assembly steps*

After the firing step, the sensors were tested and some of them appeared to be short - circuited and the signal was not very stable. This indicates that the wires were not properly insulated in the holes and at some point the touch they steel as shown in *Figure 7.6a*. To avoid this result, alumina tubes were placed in the holes and then the same procedure was followed (*Figure 7.6b* and *Figure 7.7*).

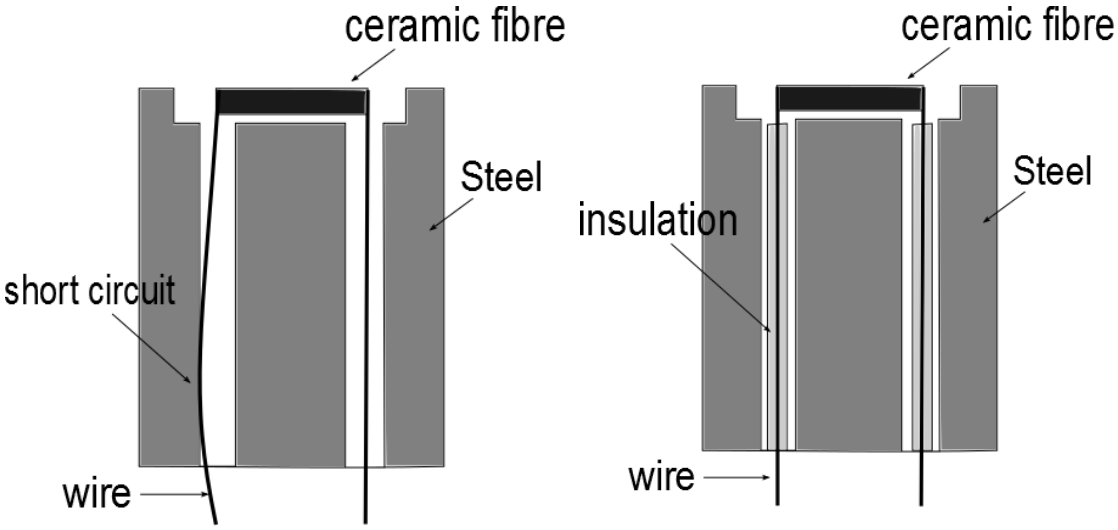

(a) *(b)*

Figure 7.6: *Schematic design of short circuit in the prototype sensors*

Figure 7.7: *Prototype sensors using alumina tubes*

The final design of the sensor is shown in *Figure 7.8*.

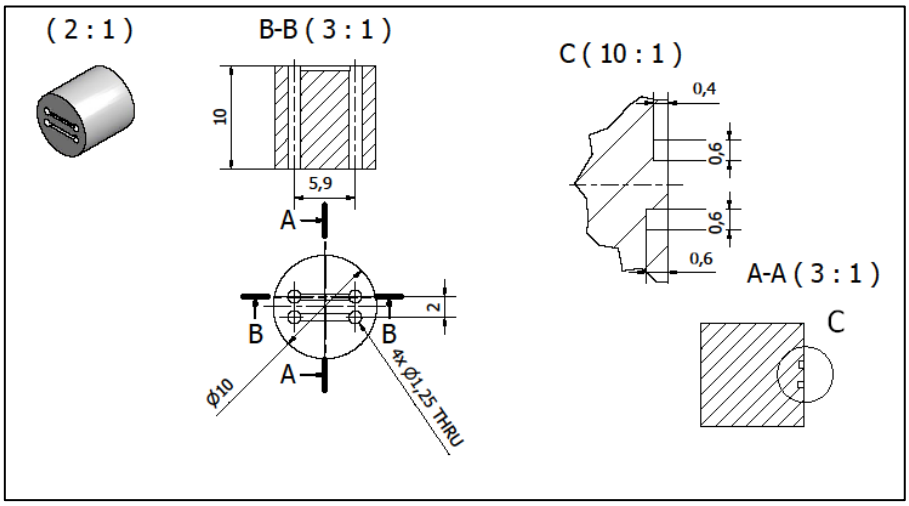

Figure 7.8: *Test sensor 8 from Müggler (project partner)[12]*

7.2 Test results

The prototype sensors were then tested by Pera Innovation Ltd, the project partner responsible for manufacturing the electronic hardware and coding the microcontroller for the MesMesh system. Pera extended the wires of the prototype sensors (*Figure 7.9*) and manufactured a tool to hold the samples (*Figure 7.10*).

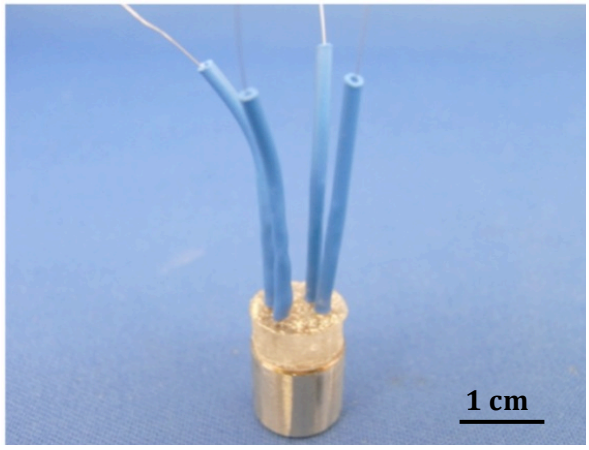

Figure 7.9: *Prototype sensor with extended wires [146]*

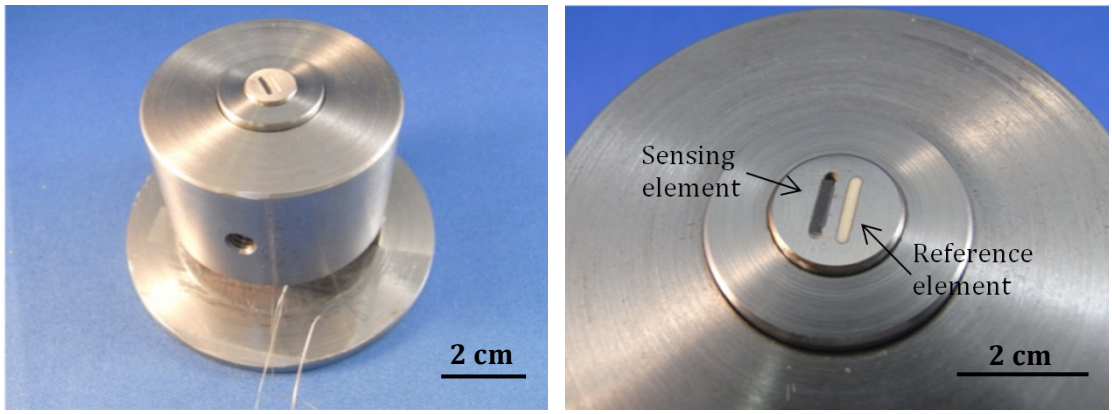

Figure 7.10: *Prototype sensor placed into holder ready for the grinding test [146]*

Using a grinder, 10 μm were removed at a time and the resistance was measured using the LCR and the MesMesh system. *Figure 7.11* shows the results of the grinding test [12]. As indicated from the graph the noise is quite significant, so no reliable conclusions can be drawn. However, there is an upward trend of the resistance as expected as the sensors wear down and its resistance increases due to a decrease in the cross-sectional area. At 150 μm there is a sharp peak and then the signal is lost, which either due to a crack in the ceramic or some damage to the wire-ceramic bond. In order to evaluate the results better, *Figure 7.12* presents the theoretical response of the sensor. This is based on the dimensions of the fibres and the measured resistivity.

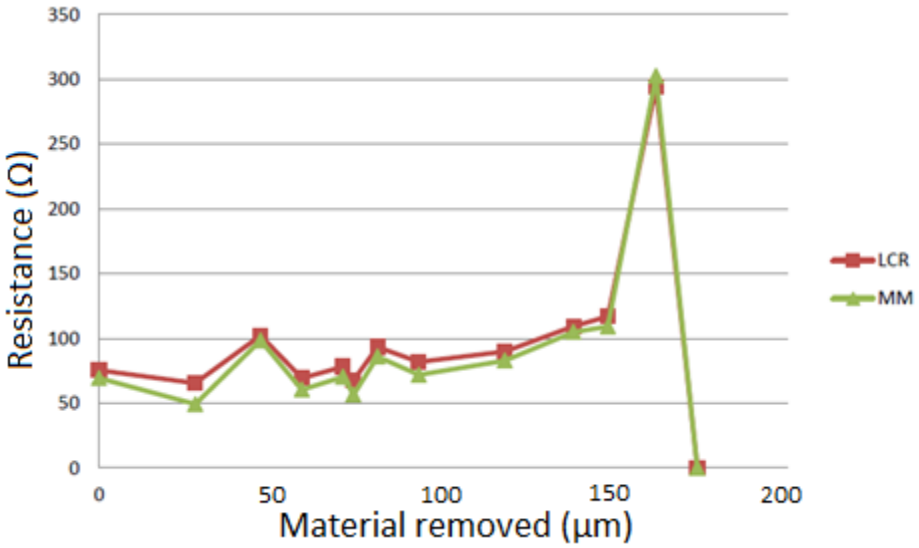

Figure 7.11: *Results of the grinding test of a prototype sensor [146]*

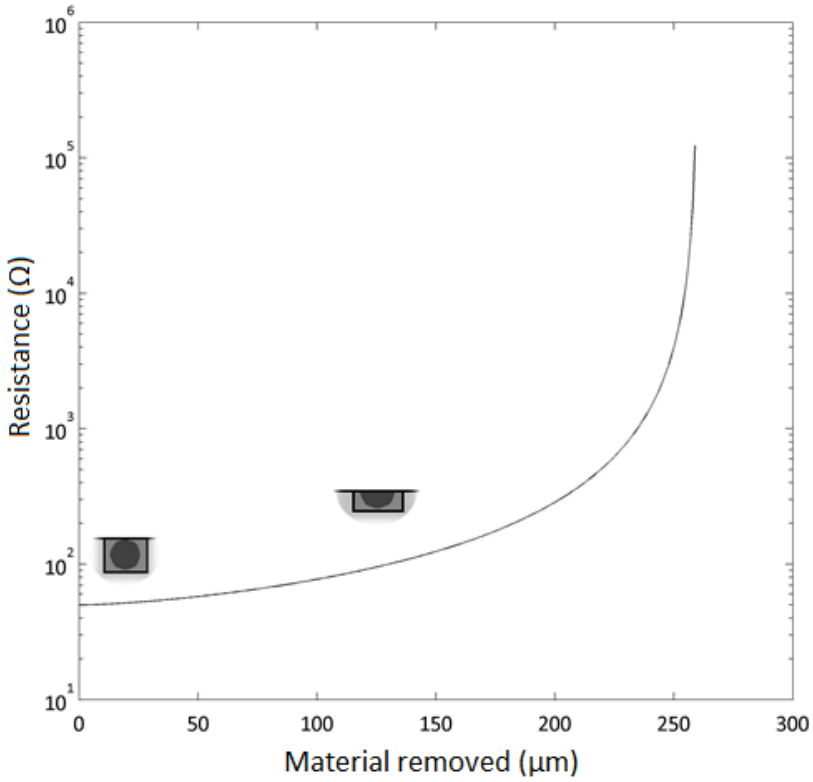

Figure 7.12: *Theoretical response of the sensor (circular cross section of the fibre) up to 260µm of material removed in a logarithmic scale*

To optimize further the integration step and reduce noise from the results (*Figure 7.11*), it was necessary to cover the top part of the holes, since debris

during the grinding test was falling in the holes and touching the wires causing noise to the measurements (*Figure 7.13*).

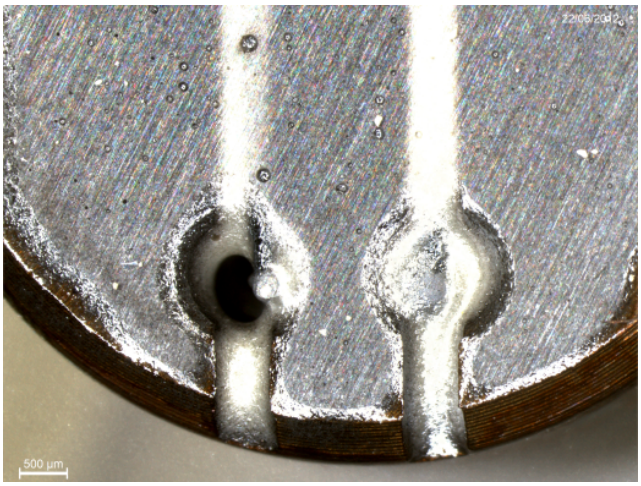

Figure 7.13: *Exposed fibre and wire on the sensor surface*

In order to achieve this, a high temperature two-part resin was used, that offered additional protection to the surface of the sensor. *Figure 7.14* shows the flat fully covered surfaces of three of the sensors tested by Pera Innovations.

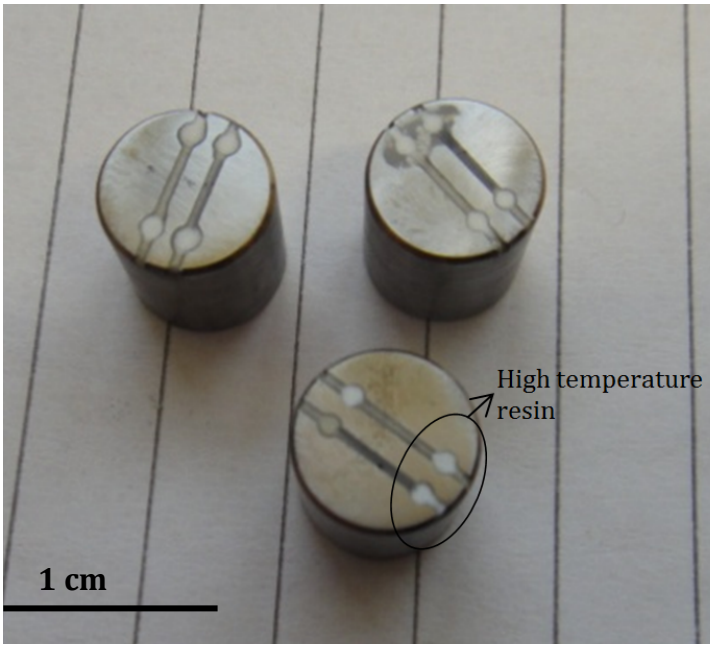

Figure 7.14: *Sensors after using a high temperature resin to cover the exposed fibres and wires on the surface*

Additionally, in order to optimize the termination of the wires to ensure stable measurements a combination of plastic rings, resin and metal tubes and copper wires were also used as shown in *Figure 7.15.*

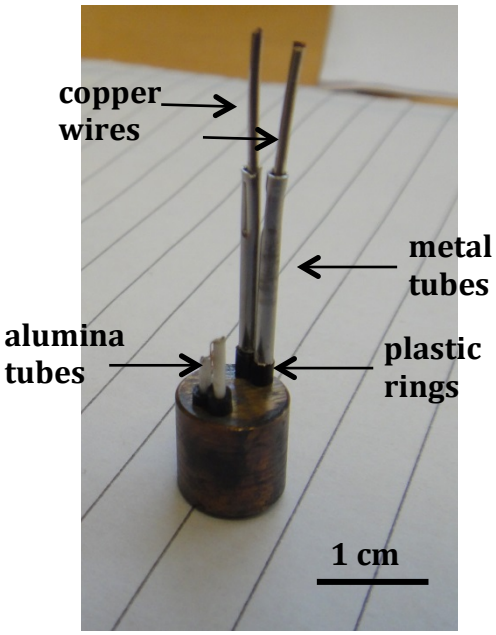

Figure 7.15: *Extension and termination of the wires in University of Bath*

The grinding test results are presented in *Figure 7.16*. The noise has been reduced considerably, however after having removed half of the fibre (130μm) the signal is lost presumably due to loss of the wire-fibre electrical contact. *Figure 7.17* compares these results with the theoretical response.

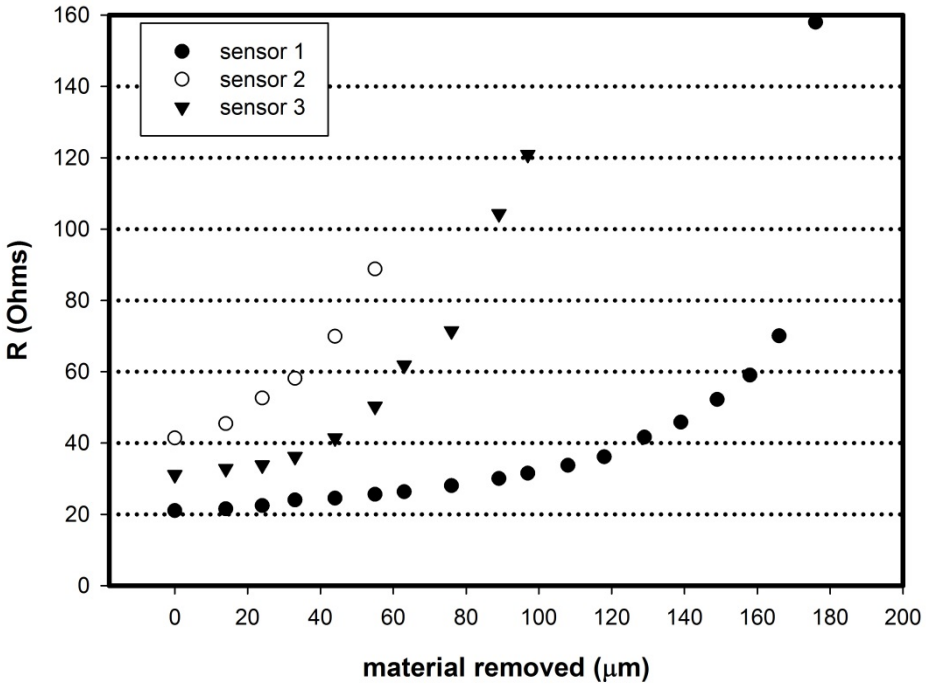

Figure 7.16: *Grinding test results for three (3) prototype sensors*

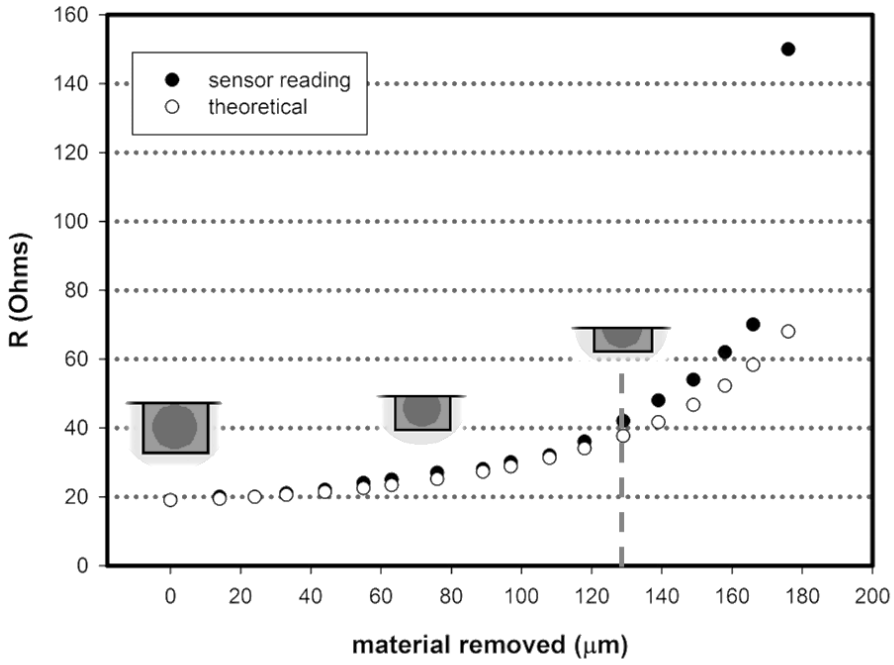

Figure 7.17: *Comparing results of a sensor with theoretical response*

The sensor follows the theoretical response until 130μm have been removed from the surface which is the half of the fibres. After that degree of removal the

readings from the sensor are approximately 5% higher than the model reading and after 170µm are removed the sensor fails. This is likely to be due to the fact that the wire-fibre bonds are destroyed. As shown in *Figure 3.23* (section 3.2.2) the wire is attached on the sides of fibre, but the exact point of contact is not possible to control. In order to improve this parameter, that causes the failure of the sensor at 130µm, University of Vilnius (MesMesh project partner) has conducted work on the fibres and were able to micromachine wells using femtosecond laser pulses in order to provide support points for the wire soldering [147]. *Figure 7.18* shows the micromachined fibres. Since the Magnéli phases fibres may reoxidize at high temperature, the structure of the fibres may change around the well in case of too high pulse power and repetition rate as shown in *Figure 7.19*.

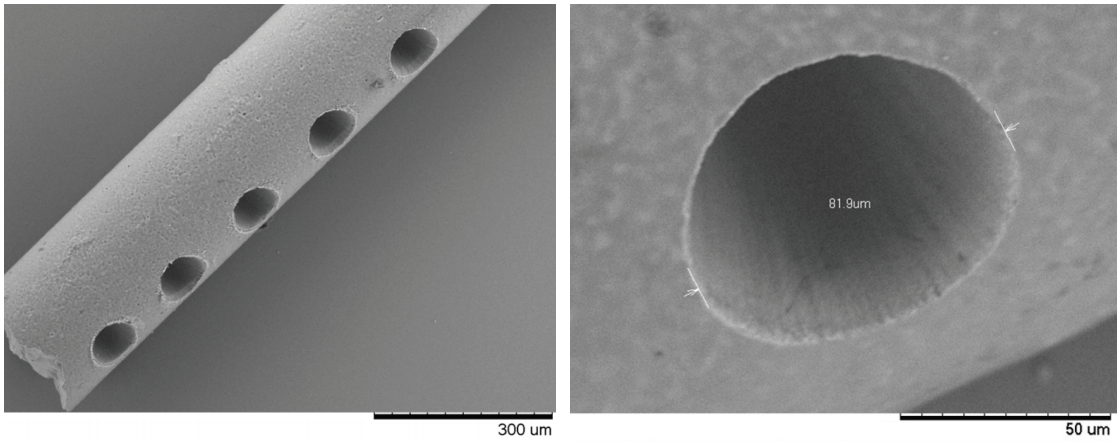

Figure 7.18: *Microwells machined in ceramic fibres, with 160 µm of depth [147]*

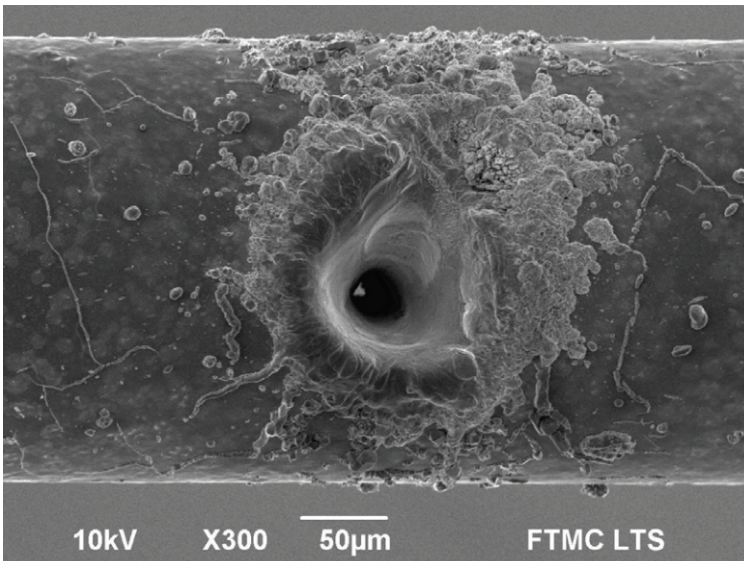

Figure 7.19: *Re-oxidized fibre after micromachine using too high pulse power and repetition rate [147]*

The sensor was also placed in the mould in Balpol (MesMesh project partner) and used in actual operation conditions in the injection machinery for a short time without any faults. However, in this short operation time it was not possible to extract results. *Figure 7.20* shows a sensor in a nail mould as it was tested and the initial reading of resistance.

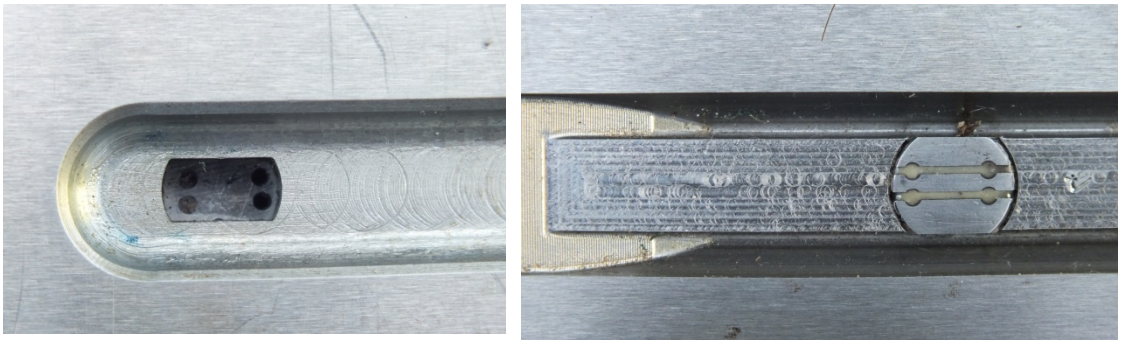

(a) (b)

(c) (d)

Figure 7.20: *(a) Nail mould with machined place for the sensor, (b) sensor in the nail mould as it was placed in the injection machinery, (c) wire exits and (d) the sensor interface with initial reading [148]*

7.3 Discussion

The aim of this chapter was to present the work for the final stages of the MesMesh EU Project. This work focused on integrating the Magnéli phases fibres into the final application and solving additional problems in order to achieve good results while testing the sensors.

In summary from the integration work, it can be concluded that:

i. A low melting temperature solder glass was successfully chosen to insulate the fibres in the grooves and offer a strong soldering during grinding tests and operation of the sensor in the mould. The solder glass chosen was a lead free glass based on Bi_2O_3.

ii. Noise problems due to uncovered parts of the wires were solved using a two part high temperature resin that did not offer any additional mechanical support.

iii. The termination of the wires was optimized and the extensions were strong enough to be used in the injection machinery.

iv. Promising results were acquired through grinding tests, a process more aggressive that the mechanical pressure during operation, that were in good agreement with the model prediction.

The most significant problem with the integration stage was to achieve strong and repeatable fibre-wire bonds. This can be solved by using femtosecond laser

pulses to micromachine wells on the fibres that can be used as contact points for the wire soldering. This work was presented in the final report of the MesMesh EU project and the report was accepted and the project was considered successful in producing a sensor that can measure wear continuously in real time.

8. Redox batteries

Following the manufacturing of tablets and fibres with increased surface area, cyclic measurements were conducted at the University of Southampton by PhD student Maria Kourasi to examine their performance as electrodes for Redox Flow Batteries. The set up and the results are presented in the current chapter, together with expected future work. The work presented is on the dense fibres and the tablets with increased porosity.

8.1 Electrode preparation

Due to the fragility of the porous fibres manufactured in section 5.1, it was necessary to turn them into robust Magnéli microelectrodes. The electrical contact on the dense Magnéli fibres was made by using Al paste and Ag wire, following the procedure that has been described in section 5.3. After making the electrical contact, the fibre was adjusted in a plastic micropipette, where subsequently Epoxy (RS Quick Set Epoxy Adhesive) was added to insulate and stabilise the fibre. After the Epoxy had dried and the microelectrode was solid, the tip of the pipette was polished in order to reveal the fibre and to create a uniform planar electrode (*Figure 8.1*).

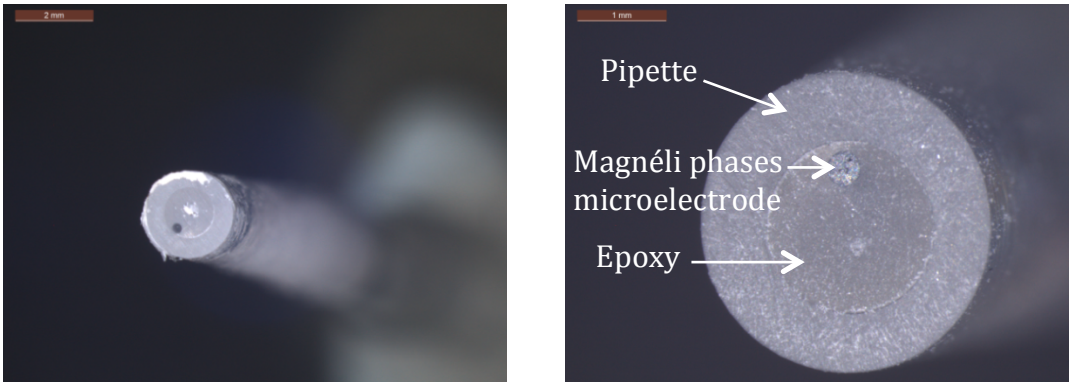

(a) *(b)*

Figure 8.1: *The microelectrodes with the dense Magnéli fibres by using an optical microscope*

The Magnéli phases tablets with increased porosity were also tested. As described in section 6.1.1 the porosity of the Magnéli tablets was controlled by increasing the organic binder during their manufacturing process. In order to characterize the tablets they had to be converted into planar electrodes. Firstly, an electrical contact was made on the tablet, by using Ag paint and Cu wire, instead of Al paste and Ag wire that have been used for the fibres. The Al paste requires a firing temperature of 710^{o}C, so it is likely that the paste would diffuse through the pores of the tablets and cause a short circuit. Since the electrical contact was made on one surface of the tablet, the other surface of the tablet was placed in contact with the electrolyte. Hence, the tablet had to be insulated by surrounding it by a material that would isolate both the remaining part of the

tablet and the electrical contact. This was achieved by inserting the Magnéli tablet into a plastic tube with similar diameter size that would let only one surface be in contact with the electrolyte (*Figure 8.2*).

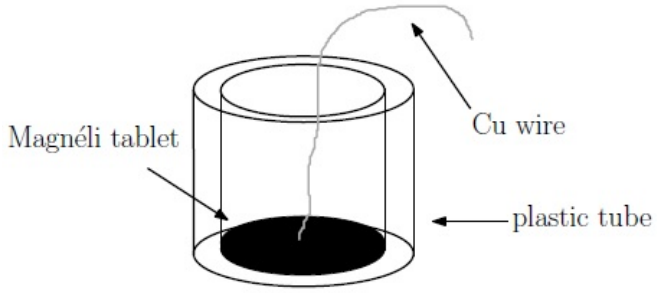

***Figure 8.2**: The design of the microelectrodes with the Magnéli tablets [106]*

8.2 Results

For the first measurement, dense fibres were used as microelectrodes in a 0.1 KNO_3 electrolyte with 5.0 mM $K_3Fe(CN)_6$ as a redox agent. In this case the dense Magnéli microelectrode was tested as a receiver of that redox activity in comparison with a glassy carbon electrode. *Figure 8.3* presents the results that confirm that Magnéli phases can detect the redox activity giving peaks with lower current density compared with the glassy carbon electrode. The voltage window of the redox peaks is wider for the Magnéli microelectrode due to the lower conductivity compared to glassy carbon (10^3 S/m [149], compared to 10^{-2} S/m for the Magnéli phases tablets).

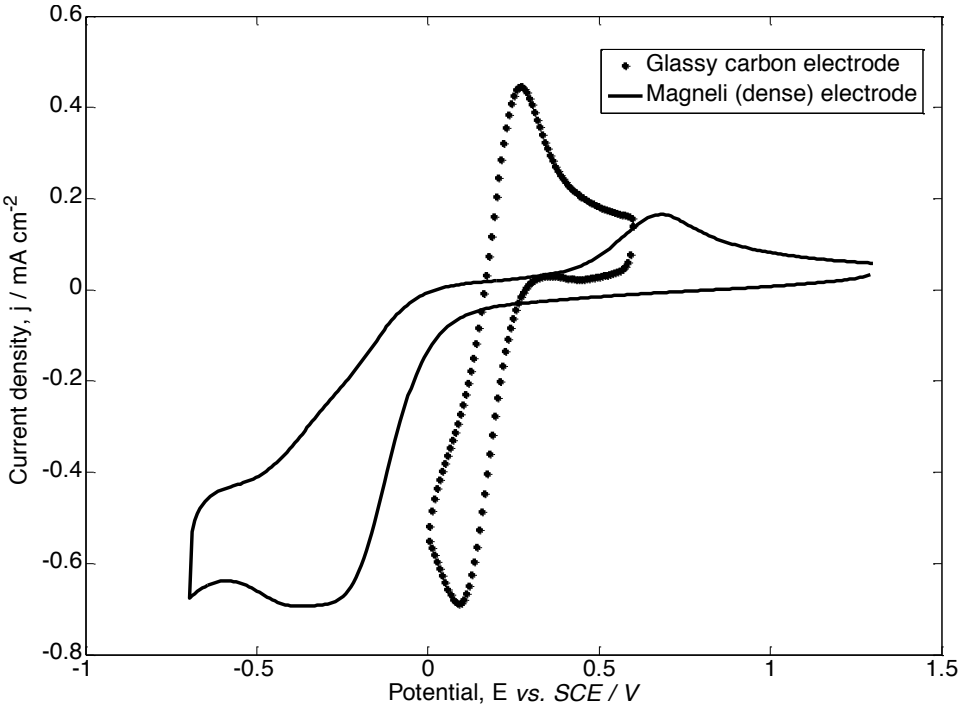

Figure 8.3: *Cyclic voltammogram of a glassy carbon electrode (-) and Magnéli microelectrode (.) with a dense fibre in 5.0 mM $K_3Fe(CN)_6$ in 0.1 KNO_3. The scan rate of the voltammograms was 50 mV sec^{-1} and the temperature was 293K [106]*

Figure 8.4 compares the data of the porous Magnéli phases tablets. The most porous tablet (50%wt binder and 65%porosity) has the highest current intensity redox peaks, however it also exhibits higher capacitance. The increased porosity may prevent a good bond of the sample with the electrode used to solder the wire. Both can be the reasons for the increased capacitance.

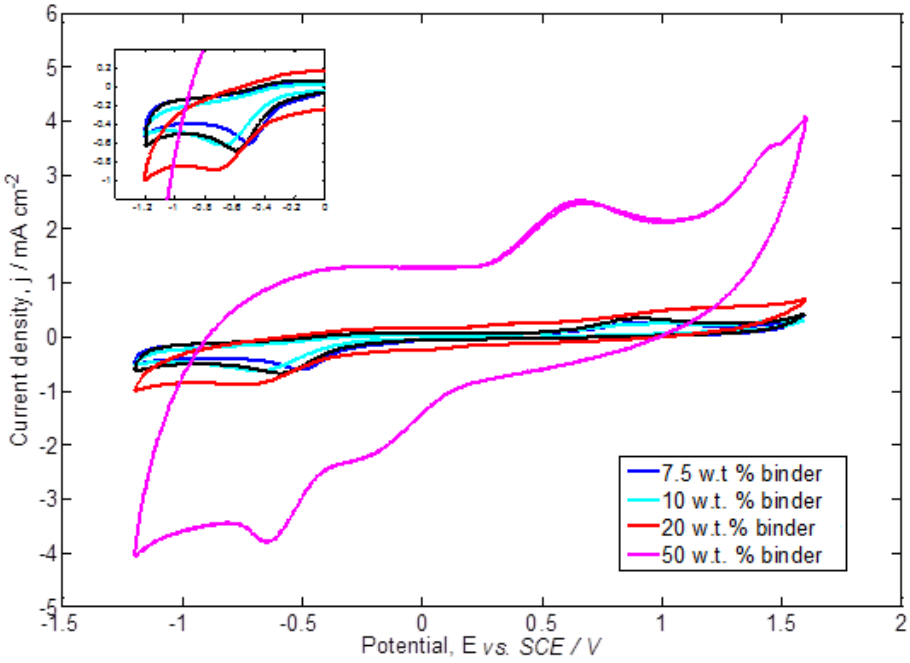

Figure 8.4: *Cyclic voltammograms of various electrodes with Magnéli phases tablets with different binder loading 5.0 mM $K_3Fe(CN)_6$ in 0.1 KNO_3. The scan rate of the voltammograms was 50 mV sec^{-1} and the temperature was 293K [106]*

The next group of experiments involve the testing of the increased porosity fibres that were manufactured as described in section 6.1.2. The fibres using the 54v% TiO_2 feedstock have a high density core and increased surface area. The dense core could offer high carrier mobility and good sample-electrode bond.

8.4 Discussion

The work presented in this chapter is the initial work on Magnéli phases electrodes using cyclic voltammetry. The results look promising since redox activity can be detected using Magnéli phases electrodes. Although the 65% porosity (using 50wt% binder) tablets have maximum active area they also exhibit higher capacitance that is likely to be the result of a poor electrode/wire-sample contact because of the rough surface.

9. General discussion and future work

This final chapter of the thesis summarizes the results presented in the previous chapters and discusses the key findings of the work. Following the discussion, ideas and plans for extending this work are discussed. Initial results of this additional work that is already in progress are also presented. In the final section the reader can also find a list of conferences at which I had the opportunity to disseminate my work, journal publications that present the current work, including a patent and publications on additional work that I was involved. During my studies I also had the opportunity to visit and work in three Institutes that are included in the final section.

9.1 General discussion

The main achievements and novelties of this work are:

i. Managing to manufacture fine scale dense Magnéli phases fibres with constant conductivity that can be tuned within a range of five orders of magnitude.
ii. Studying the electrical properties of Magnéli phases fibres.
iii. Studying the re-oxidation mechanism of Magnéli phases.
iv. Being able to use these ceramic fibres in wear sensor, achieving ohmic contacts, integrating the sensor and showing promising results using the sensor.
v. Developing methods of producing porous Magnéli phases materials, including high surface porosity materials.

One of the main aspects of the research was the initial materials selection and matching the main requirements for the wear sensor that were the hardness and the thermal expansion coefficient. Further wear measurements were undertaken to make sure the wear rate of the Magnéli phases matches that of steel. Tuning the conductivity of the Magnéli phases by optimising the manufacturing process was a main part of the research, as well as understanding the electrical properties by using Impedance Spectroscopy. Having reproducible dense Magnéli phases fibres with constant conductivity, it was very important to study the thermal stability, since reoxidation of the Magnéli phases is the main disadvantage. The study of the reoxidation mechanism has set an operation limit of 650^{o}C and has proven the stability of the fibres at the operation temperature of the sensor.

Regarding the integration of the sensor a key element in achieving measurements without noise was insulating the fibres and the wires using a solder glass and alumina tubes respectively.

Another main aspect of this research was the collaboration with EMPA Institute and University of Southampton. During a work visit to EMPA Institute fibres with increased surface area were manufactured and at the University of Southampton the samples were tested as electrodes with promising results.

The following section discusses future work that can be done to optimise the existing applications and future work on manufacturing and tuning the properties to match additional possible applications.

9.2 Future work

Having achieved the main objectives of this work, there are still aspects that need optimising. Regarding the wear sensor, having produced prototype sensors that gave accurate measurements, optimising the integration process is necessary in order to achieve reproducibility of the final application. The key aspect of the integration is achieving a strong and stable wire-fibre bond. The future work can focus on using the wells on the fibres – manufactured with a femtosecond laser in University of Vilnius [147] – as contact points for the wire bonding.

Regarding the increased surface porosity fibres, further work is needed to understand the burning out of the thermoplastic binder that results in acquiring hollow fibres and the role of the paraffin. This work is going to take place as part of the collaboration with EMPA Institute using thermogravimentric analysis to study the decomposition of the thermoplastic binder.

Taking the work on Ti-suboxides further, work on another application has started. TiO_2 is of interest for the photovoltaic conversion of light to electricity and the photocatalytic conversion of light to chemical fuels [150-156]. One of the factors that limit the utility of TiO_2 for these applications is the wide band gap. By altering the manufacturing methods used to obtain Magnéli phases (Ti_nO_{2n-1}) it was possible to introduce Ti^{3+} and Ti^{4+} defects in the structure that resulted in increasing the photocatalytic activity. Bulk dense TiO_2 samples were prepared as described in section 4.1.2. The tablets were then reduced at various temperatures in order to introduce the oxygen vacancies, but not change the lattice and produce the Magnéli phases. Therefore the reduction temperatures used were lower than 1300^{o}C. Using Impedance Spectroscopy, the effect of the various contents of defects on the electrical response will be studied. The photocatalytic activity will then be tested under UV light.

Additionally, focusing again on testing the photocatalytic activity tungsten doped TiO_2 was synthesised during my visit in AMPRI and MANIT, India. In these samples the properties of anatase TiO_2 are altered by introducing tungsten in the lattice in various concentrations. The tungsten doped TiO_2 was synthesised using emulsion and the precursors. Further work will take place to relate the structure to the photocatalytic activity of the W-TiO_2.

9.3 Dissemination

The publications that arise from this PhD are:

1. D. Regonini, V. Adamaki, C. R. Bowen, S. R. Pennock, J. Taylor, A. C. E. Dent, 'AC electrical properties of TiO_2 and Magnéli phases, TinO2n-1', Solid State Ionics, 229, 2012, 38-44.
2. V. Adamaki, F. Clemens, P. Ragulis, S. R. Pennock, J. Taylor and C. R. Bowen, 'Manufacturing and characterisation of Magnéli phase conductive fibres', J. of Materials Chemistry A RSC, 2, 2014, 8328-8333.
3. C. R. Bowen, V. Adamaki, T. Thomas, 'Manufacture of porous electrically conductive ceramics', paper accepted for presentation and publication in the proceedings of Mining, Materials and Metallurgical Engineering International Conference, Prague, 11-12 August 2014.
4. V. Adamaki, F. Clemens, J. Taylor, T. J. Mays, C. R. Bowen, 'Re-oxidation mechanism and kinetics of fine scale Ti-Magnéli phases in fibre form using thermogravimetric analysis', Journal of Materials Science, 49, 2014, 7597-7603.

Copies of the publications are available in Appendix 1.

As part of the EU MesMesh project a patent was issued including the findings of this work:

i. Sensor system for monitoring wear, EP 2637014 A1, 2013

Additionally, this work was presented in the following conferences and workshops:

1. Electroceramics XIII, 24th-27th of June 2012, University of Twente. Enschende, Netherlands. Poster presentation with title 'Development

and electrical characterisation of conductive Ti - Magneli phases for sensing applications'.

2. Defects in Semiconductors, Gordons Research Conferences, 12th-17th of August 2012, University of New England, ME, USA. Poster presentation with title 'Electrical characterisation of conductive Ti - Magneli phases'.
3. FEMS EUROMAT 2013, 8th-13th of September 2013, Seville, Spain. Oral presentation with title 'Manufacture and characterisation of Magnéli phases conductive ceramic fibres for sensing application'.
4. International workshop on Green Buildings and Sustainable Technologies, 7th of December, IIT Delhi, New Delhi, India. Oral presentation with title 'Manufacture and characterisation of Magnéli phases conductive ceramic fibres'.

During my PhD I had the opportunity to visit and work in various Institutes in Lithuania, India and Switzerland:

1. 5th-9th of March 2012 working in the 'Centre for Physical Sciences and Technology' with Dr Zilvinas Kancleris in Vilnius, Lithuania. My work there involved linearity tests in dense Magnéli phases fibres.
2. 2nd-6th of December 2013 working in 'Advance Materials and Process research Institute' (AMPRI) and in 'Manulana Azad National Institute of Technology' (MANIT) with Dr. Rajnish Kurchania in Bhopal, India.
3. 3rd of February to 25th of April 2014 working in EMPA Materials Science and Technology Research Institute of the ETH Domain with Dr. Frank Clemens in Zurich, Switzerland.

Work on the Magnéli phases dense fibres was also published by University of Vilnius, MesMesh EU Project partner, and it includes femto-second laser micromashining in order to create contact points for the wires bonding [147]. Finally, having gained experience on Impedance Spectroscopy though my PhD, I also took part in work published in Pure and Applied Chemistry and presented at the 9th International Symposium on Novel Materials and their Synthesis (NMS-IX) and the 23rd International Symposium on Fine Chemistry and Functional Polymers (FCFP-XXIII) in Shanghai, 17-22 October 2013, with title

‘Manufacture and characterisation of conductor-insulator composites based on carbon nanotubes and thermally reduced grapheme oxide’ [157].

References

1. Seventh framework programme theme, *The development project for a cheap, innovative yltra thin conductive ceramic mesh to monitor stress and wear on a steel surface*. 2009.
2. Cohen, E.A., *Embedded wear sensor*. 2000, The USA as represented by the secretary of Navy US, patent no 6,080,982.
3. Takeshi, S. and I. Yoshiyuki, *Wear sensor*. 1989, Mitsubishi Cable Industries, Ltd: US, patent no 4,884,434.
4. Purvis, H.A. and R.F. Strickers, *Wear sensor system*. 1987: US, patent no 4,655,077
5. Bödecker, A., et al., *Manufacturing of a wear detecting sensor made of 17-4PH steel using standard wafer processing technology.* Sensors and Actuators A: Physical, 2011. 171(1): p. 34-37.
6. Lüthje, H., et al., *Thin film sensor for wear detection of cutting tools.* Sensors and Actuators A: Physical, 2004. 116(1): p. 133-136.
7. Yaxley, S.J. and J.A.G. Knight, *The development and integration of novel sacrificial wear sensors into the quarrying industry.* Sensors and Actuators A: Physical, 1999. 75(1): p. 24-34.
8. Ruff, A.W. and K.G. Kreider, *Deposited thin-film wear sensors: materials and design.* Wear, 1997. 203–204(0): p. 187-195.
9. Baldwin, D.G. and A.E.S. White, *Resistive wear sensors*. 1987, Morganite Electrical Carbon Limited: US.
10. Vasilow, T.R., et al., *Resistive ceramic bushings for brake lining wear sensor*. 1986, General Motors Corporation: United States.
11. Fritsch, H., et al., *A low-frequency micromechanical resonant vibration sensor for wear monitoring.* Sensors and Actuators A: Physical, 1997. 62(1–3): p. 616-620.
12. MesMesh consortium, *Technical progress report 24M*. 2012: Copenhagen.
13. ExxonMobil, *The outlook for Energy: A view to 2040*. 2013.
14. Ardizzon, G., G. Cavazzini, and G. Pavesi, *A new generation of small hydro and pumped-hydro power plants: Advances and future challenges.* Renewable and Sustainable Energy Reviews, 2014. 31(0): p. 746-761.
15. Yang, Z., et al., *Thermodynamic analysis of a hybrid thermal-compressed air energy storage system for the integration of wind power.* Applied Thermal Engineering, 2014. 66(1–2): p. 519-527.
16. Sebastián, R. and R. Peña Alzola, *Flywheel energy storage systems: Review and simulation for an isolated wind power system.* Renewable and Sustainable Energy Reviews, 2012. 16(9): p. 6803-6813.
17. energystorage.org (2014).
18. International panel for the RCUK review of energy 2010, *Progressing UK Energy Research for a Coherent Structure with Impact*. 2010.
19. Koohi-Kamali, S., et al., *Emergence of energy storage technologies as the solution for reliable operation of smart power systems: A review.* Renewable and Sustainable Energy Reviews, 2013. 25(0): p. 135-165.

20. Alotto, P., et al., *Redox flow batteries for the storage of renewable energy: A review.* Renewable and Sustainable Energy Reviews, 2014. 29(0): p. 325-335.
21. newenergyandfuel.com (2014).
22. Kim, K.T., et al., *Hardness and wear resistance of carbon nanotube reinforced Cu matrix nanocomposites.* Materials Science and Engineering: A, 2007. 449–451(0): p. 46-50.
23. Barick, P., et al., *Load-dependent indentation behavior of β-SiAlON and α-silicon carbide.* Journal of Advanced Ceramics, 2013. 2(2): p. 185-192.
24. Regonini, D., et al., *Ceramics for wear sensors- electrical and thermal properties*. 2011, University of Bath: Bath.
25. Nowotny, V.H., *Strukturchemie einiger Verbindungen der Übergangsmetalle mit den elementen C, Si, Ge, Sn.* Progress in Solid State Chemistry, 1971. 5: p. 27-70
26. Barsoum, M.W., *The $M_{N+1}AX_N$ phases: A new class of solids; Thermodynamically stable nanolaminates.* Progress in Solid State Chemistry 2000. 28: p. 201-281.
27. Barsoum, M.W., *The $M_{(n+1)}AX_{(n)}$ Phases and their Properties.* Vol. 2. 2010: Wiley-VCH Verlang.
28. Eklund, P., et al., *The $M_{(n+1)}AX_{(n)}$ phases: Materials science and thin-film processing.* Thin Solid Films, 2010. 518: p. 1851-1878.
29. Barsoum, M.W., et al., *Thermal and electrical properties of Nb_2AlC, (Ti, Nb)$_2AlC$ and Ti_2AlC.* Metallurgical and Materials Transactions A, 2002. 33(9): p. 2775-2779.
30. Barsoum, M.W. and M. Radovic, *Mechanical Properties of the MAX Phases*, in *Encyclopedia of Materials: Science and Technology (Second Edition)*, K.H.J.B. Editors-in-Chief: , et al., Editors. 2004, Elsevier: Oxford. p. 1-16.
31. Telle, R., et al., *Boride-based nano-laminates with MAX-phase-like behaviour.* Journal of Solid State Chemistry, 2006. 179(9): p. 2850-2857.
32. Wang, X.H. and Y.C. Zhou, *Layered Machinable and Electrically Conductive Ti_2AlC and Ti_3AlC_2 Ceramics: a Review.* Journal of Materials Science & Technology, 2010. 26(5): p. 385-416.
33. Barsoum, M.W., et al., *Processing and characterization of Ti_2AlC, Ti_2AlN, and $Ti_2AlC_{0.5}N_{0.5}$.* Metallurgical and Materials Transactions A, 2000. 31(7): p. 1857-1865.
34. Wang, P., et al., *Synthesis of Ti_2AlC by hot pressing and its mechanical and electrical properties.* Transactions of Nonferrous Metals Society of China, 2007. 17(5): p. 1001-1004.
35. Barsoum, M.W., *Physical Properties of the MAX Phases*, in *Encyclopedia of Materials: Science and Technology (Second Edition)*, K.H.J.B. Editors-in-Chief: , et al., Editors. 2006, Elsevier: Oxford. p. 1-11.
36. Bak, T., et al., *Photocatalytic water disinfection on oxide semiconductors: Part 1 – basic concepts of TiO2 photocatalysis.* Advances in Applied Ceramics, 2012. 111: p. 4-15.
37. Walsh, F.C. and R.G.A. Wills, *The continuing development of Magnéli phase titanium sub-oxides and Ebonex® electrodes.* Electrochimica Acta, 2010. 55: p. 6342–6351.

38. Carter, P. and A. Simpson, *A method of producing substoichiometric oxides of titanium by reduction with hydrogen*. 2009, Google Patents.
39. Regonini, D., et al., *Impedance spectroscopy analysis of Ti_nO_{2n-1} Magnéli phases.* Materials Letters, 2011. 65(23–24): p. 3590-3592.
40. Andersson, S. and A. Magneli, *Diskrete titanoxydphasen im Zusammensetzungsbereich $TiO_{1.75}$-$TiO_{1.90}$.* Naturwissenschaften, 1956. 43: p. 495-496.
41. Seebauer, E.G. and M.C. Kratzer, *Charged point defects in semiconductors.* Materials Science and Engineering: R: Reports, 2006. 55(3–6): p. 57-149.
42. Harada, S., K. Tanaka, and H. Inui, *Thermoelectric properties and crystallographic shear structures in titanium oxides of the Magneli phases.* Journal of Applied Physics, 2010. 108(8): p. 0837031-1-6.
43. Liborio, L. and N. Harrison, *Thermodynamics of oxygen defective Magnéli phases in rutile: A first-principles study.* Physical Review B, 2008. 77(10): p. 104104-1-1-10.
44. Le Page, Y. and P. Strobel, *Structural Chemistry of Magnéli Phases Ti_nO_{2n-1} (4≤n≤9) I. Cell and Structure Comparisons*. J. of Solid State Chemistry, 1982 (43) 314-319
45. Lakkis, S., at al., *Metal-insulator transitions in Ti_4O_7 single crystals: Crystal characterization, specific heat and electron paramagnetic resonance.* Physical review B, 1976 (14) 1429-1440
46. Bartholomew, R. F. and D. R. Frankl, *Electrical properties of some titanium oxides.* Physical review, 1969 (187) 828-833
47. Harada, S., et al., *Thermoelectric properties and crystallographic shear structures in titanium oxides of the Magnéli phases.* J. of Applied Physics, 2010 (108) 083703
48. Hirasawa, M., et al., *Synthesis of size-selected TiO_x nanoparticles.* Applied Surface Science, 2002 (197-198) 661-665
49. Le Page, Y. and M Marezio, *Structural Chemistry of Magnéli Phases Ti_nO_{2n-1} (4≤n≤9) IV. Superstructure in Ti_4O_7 at 140K.* J. of Solid State Chemistry, 1984 (53) 13-21
50. Le Page, Y. and P. Strobel, *Structural Chemistry of Magnéli Phases Ti_nO_{2n-1} (4≤n≤9) III. Valence Ordering of Titanium in Ti_6O_{11} at 130K.* J. of Solid State Chemistry , 1983 (47) 6-15
51. Le Page, Y. and P. Strobel, *Structural Chemistry of Magnéli Phases Ti_nO_{2n-1} (4≤n≤9) II. Refinements and Structural Discussion,* J. of Solid State Chemistry, 1982 (44) 273-281
52. Anderson, J. S. and R. J. D. Tilley, *Crystallographic Shear in Oxygen-Deficient Rutile: An Electron Microscope Study*, 1970 (2) 472-482
53. Kim, K. H., at al., *Electrical conductivity of 'Hydrogen-reduced' titanium dioxide (rutile)*. J. Phys. Chem. Solids, 1984 (45) 1265-1269
54. Marucco, J.-F., at al., *Thermogravimetric and electrical study of non-stoichiometric titanium dioxide TiO_{2-x} between 800 and 1100°C*. J. Phys. Chem. Solids, 1981 (42) 363-267
55. Smith, J.R., et al., *Reviews in applied electrochemistry. Number 50 - Electrodes based on Magneli phase titanium oxides: the properties and applications of Ebonex (R) materials.* Journal of Applied Electrochemistry, 1998. 28(10): p. 1021-1033.

56. Hayfield, P.C.S., ed. *Development of a New Material - Monolithic Ti_4O_7 Ebonex Ceramic*. 2002, Royal Society of Chemistry, Thomas Graham House: Cambridge.
57. Ohkoshi, S.-i., et al., *Synthesis of a metal oxide with a room-temperature photoreversible phase transition.* Nat Chem, 2010. 2(7): p. 539-545.
58. Bartholomew, R.F. and D.R. Frankl, *Electrical Properties of Some Titanium Oxides.* Physical Review, 1969. 187(3): p. 828-833.
59. Inglis, A.D., et al., *Electrical Conductance of Crystalline Ti_nO_{2n-1} for N = 4-9.* Journal of Physics C-Solid State Physics, 1983. 16(2): p. 317-333.
60. Le Page, Y. and P. Strobel, *Structural chemistry of magnéli phases Ti_nO_{2n-1} ($4 \le n \le 9$). I. Cell and structure comparisons.* Journal of Solid State Chemistry, 1982. 43(3): p. 314-319.
61. Le Page, Y. and P. Strobel, *Structural chemistry of the Magnéli phases Ti_nO_{2n-1}, $4 \le n \le 9$: II. Refinements and structural discussion.* Journal of Solid State Chemistry, 1982. 44(2): p. 273-281.
62. Idlis, B.G. and Y.V. Kopaev, *On the theory of phase transitions in vanadium oxides V_nO_{2n-1} (magneli phases).* Solid State Communications, 1983. 45(3): p. 301-304.
63. Tang, C., et al., *Synthesis and characterization of Magneli phases: Reduction of TiO_2 in a decomposed NH3 atmosphere.* Materials Letters, 2012. 79(0): p. 42-44.
64. Kitada, A., et al., *Selective Preparation of Macroporous Monoliths of Conductive Titanium Oxides Ti_nO_{2n-1} ($n = 2, 3, 4, 6$).* Journal of the American Chemical Society, 2012. 134(26): p. 10894-10898.
65. Woo, Y., et al., *Formation of TiC particle during carbothermal reduction of TiO_2,* Journal of the European Ceramic Society, 2007. 27(2–3): p. 719-722.
66. Sen, W., et al., *Preparation of TiC powders by carbothermal reduction method in vacuum.* Transactions of Nonferrous Metals Society of China, 2011. 21(1): p. 185-190.
67. Myung, S.-T., et al., *Black anatase titania enabling ultra high cycling rates for rechargeable lithium batteries.* Energy & Environmental Science, 2013. 6(9): p. 2609-2614.
68. Li, X., et al., *Magneli phase Ti_4O_7 electrode for oxygen reduction reaction and its implication for zinc-air rechargeable batteries.* Electrochimica Acta, 2010. 55(20): p. 5891-5898.
69. Leung, P., et al., *Progress in redox flow batteries, remaining challenges and their applications in energy storage.* RSC Advances, 2012. 2(27): p. 10125-10156.
70. Chakrabarti, M.H., et al., *Application of carbon materials in redox flow batteries.* Journal of Power Sources, 2014. 253(0): p. 150-166.
71. Charlier, J.-C., X. Blase, and S. Roche, *Electronic and transport properties of nanotubes.* Reviews of Modern Physics, 2007. 79(2): p. 677-732.
72. Weber, A., et al., *Redox flow batteries: a review.* Journal of Applied Electrochemistry, 2011. 41(10): p. 1137-1164.
73. Rouquerol, J., et al., *Recommendations for the characterization of porous solids (Technical Report)* in *Pure and Applied Chemistry*. 1994. p. 1739.

74. Tu, R., et al., *Preparation of Magnéli phases of $Ti_{27}O_{52}$ and Ti_6O_{11} films by laser chemical vapor deposition.* Thin Solid Films, 2010. 518(23): p. 6927-6932.
75. Ioroi, T., et al., *Platinum–titanium alloy catalysts on a Magnéli-phase titanium oxide support for improved durability in Polymer Electrolyte Fuel Cells.* Journal of Power Sources, 2013. 223(0): p. 183-189.
76. Gardon, M., et al., *Improved, high conductivity titanium sub-oxide coated electrodes obtained by Atmospheric Plasma Spray.* Journal of Power Sources, 2013. 238(0): p. 430-434.
77. Lačnjevac, U.Č., et al., *Kinetics of the hydrogen evolution reaction on Ni-(Ebonex-supported Ru) composite coatings in alkaline solution.* International Journal of Hydrogen Energy, 2013. 38(25): p. 10178-10190.
78. Al-Jewaree H. A, M. and W. Chandler H, *Air entrapment : a source of laminations during pressing.* British ceramic. Transactions and Journal, 1990. 89(6): p. 207-210.
79. Rahaman, M.N., ed. *Ceramic Processing*. 2007, Taylor & Francis: Boca Raton.
80. Rice, R.W., *Ceramic Fabrication Technology*. 2002: Taylor&Francis Inc.
81. www.lentonfurnaces.com (2014)
82. *Extrusion in Ceramics*. Engineering Materials and Processes, ed. F. Handle. 2007.
83. www.adhesivestoolkit.com (2013).
84. Michen, M., *Co-extrusion of piezoelectric ceramic fibres*, in *KIT*. 2010: Switzerland.
85. BSI, *Advanced technical ceramics — Monolithic ceramics — General and textural properties* in *Part 2: Determination of density and porosity*. 1993, BSI 10-1999.
86. H., K.E.Y., *Air and Helium Pycnometer*. 1969: United States, patent no 3585861.
87. Netzsch, *DIL 402C*, in *handbook*.
88. Lynch, P., *MAX phase ceramics for wear sensors*, in *Mech. Eng.* 2011, University of Bath: Bath.
89. ASTM, *Standard method for wear testing with Pin-on-disk apparatus*. 2010.
90. BSI, *Advanced technical ceramics - Methods of test for ceramic coatings*. 2010.
91. Lynch, P., *MAX Phase Ceramics for Wear Sensors*. 2011, University of Bath: Bath.
92. www.setaram.com (2014).
93. Bowen, C.R. and D.P. Almond, *Modelling the 'universal' dielectric response in heterogeneous materials using microstructural electrical networks.* Materials Science and Technology, 2006. 22(6): p. 719-724.
94. Hwang, J.H., et al., *Experimental limitations in impedance spectroscopy:: Part IV. Electrode contact effects.* Solid State Ionics, 1997. 98(1–2): p. 93-104.
95. Macdonald, J.R., *Impedance Spectroscopy.* Annals of Biomedical Engineering, 1992. 20: p. 289-305,.

96. Barsoukov, E. and J.R. Macdonald, eds. *Impedance Spectroscopy Theory, Experiment, and Applications*. second ed. 2005, John Wiley & Sons, Inc.: Hoboken, New Jersey.
97. Jonscher, A.K., *The 'universal' dielectric response.* Nature, 1977. 267(5613): p. 673-679.
98. Nielsen, J. and T. Jacobsen, *Current distribution effects in AC impedance spectroscopy of electroceramic point contact and thin film model electrodes.* Electrochimica Acta, 2010. 55(21): p. 6248-6254.
99. Liu, B.S., et al., *Formation and performance of ohmic contact electrodes on $BaTiO_3$-based thermistors by localized electroless Cu-plating.* Thin Solid Films, 2010. 519(1): p. 373-377.
100. Bandyopadhyay, S., et al., *Leakage-current characteristics of vanadium- and scandium-doped barium strontium titanate ceramics over a wide range of DC electric fields.* Acta Materialia, 2009. 57(17): p. 4935-4947.
101. Bueno, P.R., et al., *SnO_2, ZnO and related polycrystalline compound semiconductors: An overview and review on the voltage-dependent resistance (non-ohmic) feature.* Journal of the European Ceramic Society, 2008. 28(3): p. 505-529.
102. Lavrov, R.Y., et al., *Comparative characteristics of silver and copper electrodes on ZnO varistor ceramics.* Journal of the European Ceramic Society, 2004. 24(9): p. 2591-2595.
103. Zhang, D., et al., *Influences of the electroless nickel electrode on the electrical characteristics of $BaTiO_3$-based PTCR ceramics.* Journal of the European Ceramic Society, 2001. 21(8): p. 1101-1105.
104. Zhou, X., et al., *Metal-semiconductor ohmic contact of SnO_2-based ceramic gas sensors.* Sensors and Actuators B: Chemical, 1997. 41(1–3): p. 163-167.
105. Sinclair, D.C., *Characterization of electro-materials using ac Impedance Spectroscopy.* Ceramics y Vidrio, 1994. 34(2): p. 55-65.
106. Kourasi, M., *research collaboration*. 2014: Univeristy of Southampton.
107. Kanthal, *Maxthal 211*, http://kanthal.com/en/products/furnace-products-and-heating-systems/refractory-material/maxthal-211/, Editor (2012).
108. C. Anirudh, A.V.V.K., V. N. Kempaiah, *Max Phase Materials- Review of an exciting class of ternary carbides and nitrides.* International Journal of Emerging Technology and Advanced Engineering, 2014. 4: p. 626-630.
109. Hashimoto, S., et al., *Pressureless sintering and mechanical properties of titanium aluminum carbide.* Materials Letters, 2008. 62: p. 1480–1483.
110. S.R. Sangawar, J.P.A., D.B. Sarwade, *A comprehensive study on some binders for piezo-electric ceramics.* Indian Journal of Engineering & Materials Sciences, 2001. 8: p. 26-35.
111. Bradley, F.N., *The Relation of Ceramics Processing to Materials Properties for Electronic Application.* IEEE Transaction on Parts, Hybrids & Packaging, 1972. PHP-8, No 4: p. 17-23.
112. Kalita, S.J., S. Qiu, and S. Verma, *A quantitative study of the calcination and sintering of nanocrystalline titanium dioxide and its flexural strength properties.* Materials Chemistry and Physics, 2008. 109(2–3): p. 392-398.

113. Zhou, A., *2 - Methods of MAX-phase synthesis and densification – II*, in *Advances in Science and Technology of Mn+1axn Phases*, I.M. Low, Editor. 2012, Woodhead Publishing. p. 21-46.
114. Song, G.M., *11 - Self-healing of MAX phase ceramics for high temperature applications: evidence from Ti_3AlC_2*, in *Advances in Science and Technology of $M_{n+1}AX_n$ Phases*, I.M. Low, Editor. 2012, Woodhead Publishing. p. 271-288.
115. Schoeck, G., *The Activation Energy of Dislocation Movement.* Physica Status Solidi (b), 1965. 8(2): p. 499-507.
116. Callister, W.D., *Fundamentals of Materials Science and Engineering*, ed. n. ed. Wiley & Sons.
117. Bowen, C.R., et al., *Modelling Power Law Dependencies of Frequency Dependent AC Conductivity and Permittivity of Conductor-Relaxor Composites.* Ferroelectrics, 2008. 370(1): p. 166-175.
118. http://accuratus.com/alumox.html (2014).
119. Regonini, D., et al., *Impedance spectroscopy analysis of Ti_nO_{2n-1} Magnéli phases.* Materials Letters, 2011. 65(23-24): p. 3590-3592.
120. Jonscher, A.K., *Universal Dielectric Response.* Nature, 1977. 267(5613): p. 673-679.
121. Almond, D.P. and C.R. Bowen, *Anomalous power law dispersions in ac conductivity and permittivity shown to be characteristics of microstructural electrical networks.* Physical Review Letters, 2004. 92(15): p. 157601-1-4.
122. Walsh, F.C. and R.G.A. Wills, *The continuing development of Magneli phase titanium sub-oxides and Ebonex (R) electrodes.* Electrochimica Acta, 2010. 55(22): p. 6342-6351.
123. Hayfield, P.C., *Development of a New Material - Monolithic Ti_4O_7 Ebonex Ceramic*. 2002, Cambridge: Royal Society of Chemistry.
124. Regonini, D., et al., *AC electrical properties of TiO_2 and Magnéli phases, Ti_nO_{2n-1}.* Solid State Ionics, 2012. 229(0): p. 38-44.
125. Tiefenbach, A. and B. Hoffmann, *Influence of a crack on the electrical impedance of polycrystalline ceramics.* Journal of the European Ceramic Society, 2000. 20(12): p. 2079-2094.
126. Cutler, I.B., et al., *Sintering of Alumina at Temperatures of 1400°C. and Below.* Journal of the American Ceramic Society, 1957. 40(4): p. 134-139.
127. J. Heiber, F.C., T. Graule, D. Hulsenberg, *Thermoplastic extrusion to highly-loaded thin green fibres containing $Pb(Zr,Ti)O_3$.* Advanced Engineering Materials 2005. 7: p. 404-408.
128. Assiamah, J.N., *Manufacture and characterisation of titanium base conductive fibres in connection with textile applications*, in *Fakultat fur Maschinenwessen*. 2012, Institute fur Textitechnik der RWTH Aschen.
129. Ferrarelli, M.C., et al., *Comment on the origin(s) of the giant permittivity effect in $CaCu_3Ti_4O_{12}$ single crystals and ceramics.* Journal of Materials Chemistry, 2009. 19(33): p. 5916-5919.
130. Słoczyński, J., *Kinetics and mechanism of reduction and reoxidation of the alkali metal promoted vanadia-titania catalysts.* Applied Catalysis A: General, 1996. 146(2): p. 401-423.

131. Prudenziati, M., et al., *Reduction process of RuO_2 powders and kinetics of their re-oxidation.* Materials Science and Engineering: B, 2003. 98(2): p. 167-176.
132. Ginstling, A.M. and B.I. Brounshteim, J. Appl. Chem. USSR, 1950. 23: p. 1327.
133. Jander, W., Z. , *Reaction in the solid state at high temperatures*, Anorg. Chem., 1927. 1: p. 163.
134. Vyazovkin, S. and C.A. Wight, *KINETICS IN SOLIDS.* Annual Review of Physical Chemistry, 1997. 48(1): p. 125-149.
135. Adamaki, V., et al., *Manufacturing and characterization of Magneli phase conductive fibres.* Journal of Materials Chemistry A, 2014. 2(22): p. 8328-8333.
136. Adamaki, V., et al., *Re-oxidation mechanism and kinetics of fine scale Ti-Magnéli phases in fibre form using thermo-gravimetric analysis.* Journal of Materials Science, 2014: p. 1-7.
137. Smith, G., *Manufacturing and Characterisation of Ti Sub-oxides*, in *Department of Mechanical Engineering*. 2013, University of Bath.
138. Sharmin, K. and I. Schoegl, *Optimization of binder removal for ceramic microfabrication via polymer co-extrusion.* Ceramics International, 2014. 40(3): p. 3939-3946.
139. Knapp, A.M. and J.W. Halloran, *Binder Removal from Ceramic-Filled Thermoplastic Blends.* Journal of the American Ceramic Society, 2006. 89(9): p. 2776-2781.
140. Humphreys, F.J. and M.G. Ardakani, *Grain boundary migration and Zener pinning in particle-containing copper crystals.* Acta Materialia, 1996. 44(7): p. 2717-2727.
141. Liang, J.Z., *Effects of extrusion conditions on die-swell behavior of polypropylene/diatomite composite melts.* Polymer Testing, 2008. 27(8): p. 936-940.
142. Chalasani, D. and R. E. Johnson, Method for rapid stiffening of extrudates, 1999, US, patent no 5966582
143. Saritha, D., et al., *Effect of Bi2O3 on physical, optical and structural studies of $ZnO–Bi_2O_3–B_2O_3$ glasses.* Journal of Non-Crystalline Solids, 2008. 354(52-54): p. 5573-5579.
144. SCHOTT, *SCHOTT Technical Glass*, SCHOTT, Editor. 2007: Mainz.
145. SCHOTT, *Low-melting Lead-free Solder Glass*, SCHOTT, Editor. 2011: Landshut.
146. MesMesh consortium, *Technical progress report 36M*. 2012.
147. D. PAIPULAS, et al., *Femtosecond Micromachining of Ceramic Fibers for Electric Contact Soldering* JLMN-Journal of Laser Micro/Nanoengineering, 2013. 8(3): p. 304-308.
148. MesMesh consortium, *Final Technical Report.* 2013.
149. Baker, D.F. and R.H. Bragg, *The electrical conductivity and Hall effect of glassy carbon.* Journal of Non-Crystalline Solids, 1983. 58(1): p. 57-69.
150. Daviðsdóttir, S., et al., *Investigation of photocatalytic activity of titanium dioxide deposited on metallic substrates by DC magnetron sputtering.* Surface and Coatings Technology, 2013. 216(0): p. 35-45.

151. Ismail, A.A. and D.W. Bahnemann, *Photochemical splitting of water for hydrogen production by photocatalysis: A review.* Solar Energy Materials and Solar Cells, 2014. 128(0): p. 85-101.
152. Lan, Y., Y. Lu, and Z. Ren, *Mini review on photocatalysis of titanium dioxide nanoparticles and their solar applications.* Nano Energy, 2013. 2(5): p. 1031-1045.
153. Bell, S., G. Will, and J. Bell, *Light intensity effects on photocatalytic water splitting with a titania catalyst.* International Journal of Hydrogen Energy, 2013. 38(17): p. 6938-6947.
154. Chen, X., *Titanium Dioxide Nanomaterials and Their Energy Applications.* Chinese Journal of Catalysis, 2009. 30(8): p. 839-851.
155. Fa, J., et al., *Titanium dioxide-reduced graphene oxide thin film for photoelectrochemical water splitting.* Ceramics International, 2014. 40(9, Part B): p. 15159-15165.
156. Chen, J. and C.-S. Poon, *Photocatalytic activity of titanium dioxide modified concrete materials – Influence of utilizing recycled glass cullets as aggregates.* Journal of Environmental Management, 2009. 90(11): p. 3436-3442.
157. Bowen Chris, R., S. Buschhorn, and V. Adamaki, *Manufacture and characterization of conductor-insulator composites based on carbon nanotubes and thermally reduced graphene oxide*, in *Pure and Applied Chemistry*. 2014. p. 765.